Dual Sensing of Cells Attachment and Spreading using Fluorescence Microscopy and Electrochemical Impedance Spectroscopy

By

Maryam Parviz

A thesis submitted in fulfilment of the requirements for the degree of

Doctor of Philosophy

The University of New South Wales, Australia

School of Chemistry, Faculty of Science and
Australian Centre for NanoMedicine

August 2016

PLEASE TYPE

THE UNIVERSITY OF NEW SOUTH WALES
Thesis/Dissertation Sheet

Surname or Family name: Parviz

First name: Maryam

Other name/s:

Abbreviation for degree as given in the University calendar: PhD

School: Chemistry

Faculty: Faculty of Science

Title: Dual Sensing of Cells Attachment and Spreading using Fluorescence Microscopy and Electrochemical Impedance Spectroscopy

Abstract:

The task of understanding the mechanisms behind these cellular actions is crucial in the way of answering cell biology enquiries and designing new therapies. The cellular responses in the presence of adhesive and soluble cues occur regularly at multiple part of the cell and vary in time duration and the place. Therefore, monitoring several aspects of cellular responses is not possible to recapitulate using a single cell-based technique. In this regard, optical microscopy and impedance spectroscopy on cell chips with molecularly engineered surfaces were coupled, simultaneously. This required the presence of adhesive cues in a controllable manner on an inert background on the surfaces.

Considering the advantages of gold surface for electrochemical measurements, gold electrodes were modified with zwitterionic antifouling coatings that limited nonspecific proteins adsorption and have low-impedance. However, challenges with gold for optical microscopy of cells were the quenching of the fluorescence by the metal and its lack of transparency. Therefore a change was made to using a transparent electrode material and a better-defined surface chemistry system.

A well-controlled chemistry was achieved on interdigitated indium-tin oxide (ITO) surfaces by forming defined density of RGD molecules using a multi-steps strategy. The coupling of Phase contrast/fluorescence microscopy and impedance spectroscopy was used to investigate whether the presence of adhesive ligands affect the cellular adhesion to the surfaces and the cell responses to chemical cues. G-protein coupled cell receptors (GPCR) were used as the pathway influenced by, a model soluble cue, histamine on interdigitated ITO surfaces with various RGD spacing. The alteration of impedance readout resulted from the changes in cell shape and adhesion to the substratum. Whereas, the fluorescence microscopy was used to track intracellular Ca^{2+} signalling. As a case study, the developed technique was used to screen the effect of potential anti-fibrotic compounds. Results illustrated that the cells on the surfaces with average RGD spacing of 31 nm displayed a stronger adhesion to the surface and a faster histamine-induced release of Ca^{2+} and change in cell adhesion than cells on the other examined surfaces with less or more adhesive ligand spacing.

FOR OFFICE USE ONLY

Date of completion of requirements for Award:

ORIGINALITY STATEMENT

‘I hereby declare that this submission is my own work and to the best of my knowledge it contains no materials previously published or written by another person, or substantial proportions of material which have been accepted for the award of any other degree or diploma at UNSW or any other educational institution, except where due acknowledgement is made in the thesis. Any contribution made to the research by others, with whom I have worked at UNSW or elsewhere, is explicitly acknowledged in the thesis. I also declare that the intellectual content of this thesis is the product of my own work, except to the extent that assistance from others in the project's design and conception or in style, presentation, and linguistic expression is acknowledged.’

Signed

Date 31/08/2016

COPYRIGHT STATEMENT

AUTHENTICITY STATEMENT

'I certify that the Library deposit digital copy is a direct equivalent of the final officially approved version of my thesis. No emendation of content has occurred and if there are any minor variations in formatting, they are the result of the conversion to digital format.'

Signed …

Date 31/08/2016

LIST OF PUBLICATIONS

Journal articles:

M. Parviz, N. Darwish, M.T. Alam, S.G. Parker, S. Ciampi, J.J. Gooding, Investigation of the Antifouling Properties of PhenylPhosphorylcholine-based Modified Gold Surfaces, Electroanalysis 26 1471-1480 (2014).

M. Chockalingam, A. Magenau, SG. Parker, **M**. **Parviz,** SR Vivekchand, K. Gaus, JJ Gooding, "Biointerfaces on Indium-Tin Oxide Prepared from Organophosphonic acid Self-Assembled Monolayers", Langmuir, 2014, 30(28), 8509-8515.

M. Parviz, K. Gaus, J. J. Gooding, Simultaneous Impedance Spectroscopy and Live Cell Fluorescence Microscopy for the Real-Time Monitoring of How Mammalian Cells Respond to Soluble and Adhesive Cues, submitted, Angewandte Chemie, Aug 2016.

M. Parviz, K. Gaus, J. J. Gooding, Monitoring the Kinetics of Cell Adhesion to Engineered Indium Tin Oxide Surfaces Presenting Different RGD Densities, submitted, ChemElectroChem, Aug 2016.

M. Parviz, P. Toshniwal, H. M. Viola, L. C Hool, P. M. W. Fear, Fiona M. Wood, K. S. Iyer and J. J. Gooding. Real-time Screening of Potential Antifibrotic Compounds on Live Cells Using a Bioelectrochemical Assay, submitted, Aug 2016.

ACKNOWLEDGMENTS

This Ph.D. was an incredible adventure full of joy for me, even though it was not always fun. I was lucky to have great people around me. Due to multidisciplinary nature of this work I have worked and learned a lot from many great people, whom without them this journey was impossible. I sincerely thank all of those who helped me through this.

In the first place, I would like to give my largest thanks to my supervisor, Scientia Prof J. Justin Gooding for his unwavering trust and support. He is not only a distinguished scientist but a great mentor that always give me truly guiding suggestions on scientific matters and on believing in myself, and the work that I am doing. I am grateful for having him as my supervisor and learning from him. I also would like to express my gratitude to Scientia Prof Katharina Gaus for her continuous supports and great scientific guides. I appreciate having the chance of working under her guidance and learning from her about cell biology and microscopy techniques.

I wish to extend my appreciation to Prof. K Swaminathan Iyer for proving the opportunity of visiting and working in his great group at University of Western Australia (UWA). His scientific advice, continuous support, and encouragement during my visit are highly appreciated. I express my wholehearted appreciation to Prof. Fiona Wood and Assoc prof. Mark Fear for providing the human primary cells and all the lessons and scientific recommendation. I would like to thanks all the members of the Iyer group for scientific help and discussions and the all the

great time we had together. I particularly like to thank Priyanka Toshniwal and Dr. Helena M. Viola for performing the immunohistology and calcium assays on Dupuytren`s cells in chapter 6. It is my pleasure to thank Dr. Nicole Smith for all of her supports and encouragements. I am so lucky that I had the chance of working with these great and cool scientists and learning from them.

I also extend my whole-hearted appreciation to all past and present members of the Gooding and Gaus groups and people in School of Chemistry and School of Medical Science, EMBL Australia Node in Single Molecule Science at UNSW for making this journey an valuable asset in my life. I will fondly remember our scientific group meeting, coffee times, and fun gatherings. I would like to extend my appreciation to Dr. Nadim Darwish for his help and encouragements especially when I was a newcomer. Thanks to Dr. Abbas Barfidokht for his continuous willing to help in the laboratory and sharing fun outside of the lab. I would like to thank Dr. Alexander H. Soeriyadi, Saimon Moraes, and Dr. Stephen Parker for X-ray photoelectron spectroscopy measurements and related discussions. I again thank Dr. Stephen G. Parker for performing the calculations on RGD spacing shown in chapter 4. Once more, I am thankful from Saimon for proofreading some parts of my thesis. I extend my thanks to Dr. Micheal Carnell from UNSW Biomedical Imaging Facility (BMIF) for his help on microscopy techniques and writing ImageJ plugins used in chapter 4. He was also extremely supportive in discussing both scientific issues and tips to help me get through the experiments especially long-term live cell microscopy. I would like to thank Dr.

Nima Gholizadeh Doonechaly for his kind helps in writing the MATLAB code for modelling section in chapter 5.

My gratitude also goes to all my friends inside and outside the university; you know who you are, the life in Australia means being with you. Thanks my dear friends; Dr. Samaneh Fard, Dr. Abbas Barfidokht, Nasim Googol, Dr. Saiede Emami, Dr. Nima Gholizadeh, Dr. Bahrareh Bahramian and Aidin Salehzadeh. I extend my appreciation to Dr. Damia Mawad, Paris Sowti, Saimon Moraes, Safura Taufik, Dr. Roya Tavallaiee for those fun tea times and helpful discussions from time to time at uni. The Ph.D. stress was never the same after boot camp sessions with warrior girls in Kat`s group, especially Dr. Sophie Pageon, Dr. Gabriella Segal, Natasha Kaushik and Mahdieh (Elham) Mollazedeh. Thanks girls for being awesome supporters.

Finally, I would like to thank my beloved family for their continued love and support throughout these years. All my love goes to my family, to my mum and dad, Parvin and Rasoul, to my brothers, Ali and Meysam, and finally, to my lovely husband, Iman, I am grateful and blessed having you in my life. You have not only been a perfect husband but also a sincere friend and supporter. I am grateful for his help even on designing my experiments, discussing scientific problems and proofreading my thesis. This work is also his own. We started this journey together and will start the next ones together.

Abstract

The ambient signals derived from different soluble or physical cues trigger complicated cellular responses that, often, determine the destiny of cells. The task of understanding the mechanisms behind these cellular actions is crucial in the way of answering cell biology enquiries and designing new therapies. The aim of this dissertation was to study the cellular responses to various environmental cues, comprehensively. The cellular responses in the presence of adhesive and soluble cues occur regularly at multiple parts of the cell and vary in time duration and the place. Therefore, monitoring several aspects of cellular responses is not possible to recapitulate using a single cell-based technique. In this regard, optical microscopy and impedance spectroscopy on cell chips with molecularly engineered surfaces were coupled, simultaneously. This required the presence of adhesive cues in a controllable manner on an inert background on the surfaces. The underlying surfaces, therefore, should provide these possibilities as well as the compatibility with the measurement techniques.

Gold electrodes were modified with zwitterionic antifouling coatings that limited nonspecific proteins adsorption and had low-impedance, considering the advantages of the gold surface for electrochemical measurements. However, the fluorescence quenching property of the gold and the prerequisite of transparency for transmitted light microscopy applications highlighted the need of utilizing indium tin oxide (ITO) as a more appropriate candidate for developing the dual optical/electrical cell-based technique.

A well-controlled chemistry was achieved on interdigitated ITO surfaces by forming defined density of RGD molecules on an inert background using a multi-steps strategy. The simultaneous setup, then, was designed and developed on interdigitated ITO surfaces. The cell attachment and adhesion in the present of different expression of adhesive ligands were investigated using the simultaneous combination of phase contrast microscopy and impedance spectroscopy. Results indicated that live cells attach and spread with different rate on the surfaces with various RGD spatial distributions. The RGD spacing of 31 nm provided the fastest rate for adhesion of the HeLa cells. These results also were used to coordinate the impedance results with the fractional surface coverage of cells on the surface.

The coupling of fluorescence microscopy and impedance spectroscopy was used to investigate whether the presence of adhesive ligands affects the cellular responses to chemical cues. G-protein coupled cell receptors (GPCR) were used as the pathway influenced by, a model soluble cue, histamine on interdigitated ITO surfaces with various RGD spacing. The alteration of impedance readout resulted from the changes in cell shape and adhesion to the substratum. Whereas, the fluorescence microscopy was used to track intracellular Ca^{2+} signalling. Results illustrated that the cells on the surfaces with average RGD spacing of 31 nm displayed a faster histamine-induced release of Ca^{2+} and change in cell morphology and adhesion than cells on the other examined surfaces with less or more adhesive ligand spacing.

As a case study, the developed technique was used to screen the effect of potential antifibrotic compounds. The results of testing PXS64 prodrug on primary human Dupuytren`s cells detected the useful time window and illustrated the capability of this methodology in examining the potential antifibrotic compounds.

The developed dual detection highlighted the importance of controlling the cellular adhesive environment on cell response to drugs. This dissertation demonstrated the power of the developed dual optical/ electrical methodology in achieving a more comprehensive sigh on cell signalling process.

LIST OF TABLES AND FIGURES

Table of Contents

CHAPTER 1

INTRODUCTION AND OUTLINE

1.1 GENERAL OVERVIEW

Many animal models have been victimized for testing food, cosmetic, and biomaterial products on live cells and developing new drugs and vaccines [1, 2]. The use of animals in scientific discoveries is back to hundreds of years BC. Currently, significant advances in understanding the mammalian physiology have been achieved by employing animal models [3]. However, since the implementation of the "Animal Welfare Guideline" in 1986, supporting the development of alternative methods that can replace, reduce or refine the use of animal models in biomedical research, testing or education purposes is the declared policy of the European institutions [4]. The principles of replacing, reducing or refining the animal studies were defined based on the survey done by Russell and Burch in 1959 [5]. In Australia, the National Health and Medical Research Council (NHMRC) has adopted the ethics of recruiting animals in research and teaching following a report by the Senate Select Committee in 1984 [6]. It aimed not to stop using animals in laboratories but to guide the way that animals should be treated in experiments and always considering the possible replacement approaches. Accordingly, animal studies in laboratories are acceptable when there is no alternative or the risk assessment is involved with either human health or environment safety [7]. During the last 25 years, several efforts have been made towards the development and international acceptance of alternative methods to animal experiments [4, 8].

In addition to ethical concerns, scientific reasoning about the validity of animal studies due to the high rates of failure reported in clinical assessments following preclinical confirmations on animals have been presented [9, 10]. Previously, 92 % of the failure rate of clinical trials that were performed following successful animal experiments was reported by the U.S. Food and Drug Administration (FDA) in 2004 [11]. One of the factors in the decrease in the number of new therapies in 2004 was reported to be misleading information obtained based on animal experimentation [12]. Part of the reason for this discrepancy is the fundamental physiological differences between human and animal bodies which make it challenging to extend the reaction of the animal body to the examined product, or stimuli to the response of the human body. One of these policies is running comprehensive *in vitro* assays and characterizations prior to animal studies. This approach can reduce the number of needed animal experiments in the process of developing new bioproducts including therapeutic drugs. In these regards, using high-throughput biochemical assays and cell-based techniques have been considered to reduce unnecessary animal studies and to increase the reliability of the screening process in advance of running *in vivo* experiments or even as an alternative for animal studies. Validated *in vitro* high-throughput studies aid in providing a deeper understanding of the cellular behaviour as it provides a less complex environment *in vivo* and limits the number of interfering parameters [7]. High-throughput biomedical assays recruit selective molecules such as enzymes, antibodies, DNA or RNA strands to sense the analyte by altering the immediate environment of the signals [13, 14]. Such sensors provide

valuable information on specific compounds, but would not determine the potency of those agents in complicated environment of the living cells. Cell-based assays have emerged as a more physiologically relevant alternative to biochemical high-throughput measurements that circumvent the need of purifying protein and enzymes in many studies [15].

1.2 BASIC FEATURES OF CELLS AND EXTRACELLULAR MATRIX

Eukaryote cells are composed of the plasma membrane, cytoplasm, nucleus and different organelles such as endoplasmic reticulum, mitochondria, and Golgi apparatus. Interconnected networks of filaments and tubules inside the cytoplasm form the cytoskeleton. This structure not only supports the mechanical structure but also regulates a lot of cell functions. There are three main types of proteins in cytoskeleton structure including microtubules (actin filaments), thin filaments and intermediate filaments.

Cells are surrounded by extracellular matrix (ECM) which acts as a scaffold for cell ingrowth and proliferation [16]. The ECM composes of two main subclasses. First, polysaccharide glycosaminoglycans such as hyaluronic acid serve as mediators for cell proliferation and nutrient transfer. Second, fibrous proteins consisting of two types mainly acting as structural supports and adhesive agents. For instance, elastin and collagen play critical roles in cell supports and fibronectin and laminin aid in providing adhesive points. The majority of

mammalian cells tend to attach and adhere to each other and to the substratum to be able to precede cell spreading, proliferation, migration, and signalling.

1.3 CELL ADHESION

Integrins are cell membrane receptors bridging cells to ECM. These receptors act as mediators connecting the intracellular actin cytoskeleton inside the cells to the extracellular proteins such as vinculin, fibronectin, and collagen. These receptors consist of unique high molecular weight polypeptide chains, named α and β.The integrin family is highly diverse, where each receptor connects to a specific matrix protein. Almost half of the known integrins on cell membrane can recognize Arg-Gly-Asp (RGD) [17]. RGD is the most frequent sequences in ECM proteins responsible for cell adhesion [17]. The integrins undergo conformational change by a signalling process called inside-out signalling that switches integrins to a high-affinity state. The binding of RGD ligands and the cell integrins generates a major recognition block for cell adhesion and regulate multiple intracellular signalling pathways. Upon interaction of integrins with RGD sequences, large molecular complexes so-called focal adhesions (FAs) forms [18, 19]. Focal adhesions compose of integrin ligands, integrin molecules, and associate plaque proteins. Focal adhesions mediate the cell anchoring process to the ECM and is the gateway that through that ECM regulate cell functions. The widely diverse proteins in focal adhesions have a unique responsibility in activating specific cellular responses.

1.4 CELLS ARE RESPONSIVE UNITS

Cells are responsive to various environmental stimuli. The way that cells decide to react to these signals, often, determines their destinies [20, 21]. Environmental signals can arise from exposure to different soluble or physical cues. The cells responses are, often, incredibly complicated and vary in the space and timescale [22]. Soluble cues such as cytokines, growth factors, hormones and soluble synthetic molecules elicit multiple responses in the target cell. These cues arise from various sources such as the cells themselves, nutrient molecules, therapeutic agents or chemical residues released from biomaterials [23]. Beside soluble molecules, cells also sense the mechanotransduction forces of their environment at the nano and micrometer range [24-26]. These forces can be derived from the ECM components [16, 27], membrane-bounded proteins, the physical property of cell environments such as the geometry [28, 29], topography [30, 31] and external local forces [24]. As explained, ECM acts not only as the supporting scaffold for cell adhesion but also as a crucial regulator of various cellular behaviours [32-34]. Cells sense the mechanic force of the extracellular environment through integrins that trigger the activation of intracellular associated cytoskeletal and signalling components of focal adhesions, and the cytoskeleton. At the same time, cells regulate the ECM structure in order to maintain overall shape and functionality by deposition, rearrangement or removal of the ECM [35]. These bilateral relationships between cells and their extracellular structure define different aspects of the cell behaviours.

1.5 CELL-BASED ASSAYS

Cell-based techniques have attracted a tremendous amount of attention in monitoring the function of cells or tissues in the presence of various signals in a controlled and reproducible environment *in vitro*[36]. The global cell-based assays market is expected to be valued at USD 18,329.37 million by 2020 from USD 10,799.53 million in 2015, with the annual growth rate of 11.16% [37]. Cell-based biosensors can be used in many applications related to health and environment sciences such as screening drugs, foods, biomaterials and other bioproducts [38]. These tools can be employed to examine the biocompatibility of biomaterials [39] and to test the influences of applying different mechanical [40-42], electrical [43-47] and electromagnetic [48, 49] stimuli on cells.

In the early 1970s, tremendous progress in diverse pharmaceutical fields was achieved, which especially occurred in understanding the biochemical and biomolecular mechanisms behind various types of disease [50]. This had an enormous impact on the current progress of the drug discovery processes. With these great strides that have been accomplished in designing new therapeutic compounds, there is a crucial need for screening these agents and their side effects *in vitro* both in terms of accuracy and scale.

A cell-based biosensor live cells are often cultured in a 2-D or 3-D artificial structure, ideally with a well-controlled environment. The physical and chemical properties of cell interaction area with the artificial environments are crucial in defining cell functions. Cell chips are mainly coupled to high-throughput read-

out technologies convert the cell response into understandable signs and can be based on optical, electrochemical or mass detection.

1.6 CELLS IN A CELL CHIP

Live cells are recruited as the sensing elements in a cell-based assay that recognize and respond to soluble or physical cues. Cells have an array of naturally evolved receptors, channels and other signalling proteins that are targeted by different soluble and adhesive cues. The signals usually cause a conformational change in the receptor structure or biochemical and ionic changes. In addition, cells act as a primary transducer in this system. The receptor activation triggers multiple intracellular pathways of events resulting in regulations in morphology, adhesion, gene expression or metabolism of cells that can be collected using an appropriate read-out system in research laboratories. In addition to mammalian cells, various microorganisms also have been employed in cell-based assays for environmental science applications, monitoring of pollutants in particular, and human health safety [15, 51-54]. There are important constraints related to using live cells as the primary sensing agents *in vitro*. For instance, the culture and maintenance, the specification of the cells such as the number of passage or the density of the cells and the presence of a few unhealthy cells may cause misleading information [55]. Therefore, specific considerations and care should be followed while treating cells to act as a crucial element in cell-based assays.

1.7 CELL-SURFACE INTERFACE

The interactions of cells and their surrounding environment, especially the ECM plays a profound role in cell functions. The ECM function is mimicked *in vitro* by engineering the cell-environment interface. It has been shown that the physical and chemical characteristics of the underlying surface play a major role in modulating cellular responses. The properties at the cell/surface interface such as geometry, stiffness and the presence of adhesive ligands significantly regulate the cell behaviour [56]. Consequently, in a cell-based assay that cells are supposed to be cultured on foreign materials in a 2-D or 3-D structure, the interface ideally mimic the native extracellular environment of cells as close as possible. A well-controlled environment allows driving the cell functions into desired direction [20, 57].

The 3-D cell-based models such as microgravity bioreactors [58] synthetic and natural polymeric scaffolds [59-61] and micro/nanoporous substrates [62] provide an environment to evaluate the effect of applying different treatment and stimuli on live cells. The structure of these models can be designed to mimic natural cellular environments of various parts of the body, such as tissues, tumours, and vessels. Recently, Yang and his co-workers [63], have reviewed the applications of three-dimensional cell culture systems in cell-based assays. These devices propose efficient and reliable tools for drug discovery, toxicology, stem cell and cell sorting applications, where the cell responses to different stimuli need to be investigated *in vitro*. The 3-D cellular structures are fabricated using different technologies such as inkjet printing [64] and microfluidics [65, 66].

In some studies, 3-D cell-based platforms propose a model that mimic the *in vivo* condition in a more reliable way than 2-D cell chip assays [67]. However, they are not a replacement for specific applications that require the devices based on silicon, glass or conductive electrodes, such as electrophoresis on glass or electrochemical measurements on electrode plates. In addition, the ease of coating the surface of 2-D chips provides a well-controlled environment where the response of a single cell or population of cells can be investigated. The focus of this study is on modifying the 2-D structures (surfaces) for different cell-based sensing applications. The temporal response, spatial considerations, and sensitivity of the substrate must be optimized for the specific biological application [68]. The appropriate interface for a cell-based assay should possess the possibility of being modified with appropriate molecules and provide the appropriate physical characteristics to be used in coupled with the suited high-throughput read-out detection system and is chosen based on the biological inquiry.

1.8 MODIFICATION OF SURFACES IN CELL-BASED ASSAYS

It has been indicated that the surface characteristics modulate various cellular functions, such as adhesion, proliferation, differentiation and migration [18, 19, 33, 69, 70]. Coating the surfaces with ECM proteins such as fibronectin or collagen is a straightforward and efficient approach for mimicking the ECM structure in many studies. For very fundamental understanding, that requires

precise control over the composition and the arrangement of the surface modification [71], the ambiguity of how the actual cell adhesive ligands are presented in protein and polymeric adhesive surfaces can compromise the robustness of the conclusions reached [72]. The other factor restricting the use of whole proteins for this application is the difficulties of controlling the adsorption of non-specific biomolecules that decreases the selectivity and sensitivity of cell-based sensors. Surfaces with rigorous molecularly engineered chemistry are needed to remove ambiguity regarding cell adhesive ligand presentation of the cell-based assays and provide the insight into how cells sense different physical cues [20, 56]. The cell-based chips may be modified with adhesive ligands to mimic the ECM contribution in cell adhesion process. Controlled RGD ligands expression is possible by immobilizing the ligands on surfaces in a form of a monolayer [20, 73].

The types, spacing, surrounding microenvironment and organization of RGD adhesive ligands on the surfaces can be tightly defined using chemical immobilizing techniques. Slight changes in the expression of adhesive ligands alter cellular phenotype dramatically [20]. It highlights the importance of applying a well-controlled chemistry into the surfaces that are for in cell-based assays.

1.8.1 Impact of RGD expressions on cell function

Monolayer modified surfaces can provide greater control over the expression of RGD adhesive cues on a cell-inert background [56]. The chemistries that restrict nonspecific protein adsorption using oligo(ethylene glycol) moieties molecules

[74] or zwitterionic monolayers [75, 76] can be used to provide a cell inert surface to which the RGD sequences can be attached. In this way, excellent control over the extent of cell adhesion can be achieved.

The type, spacing, organization and the surrounding molecules of adhesive ligands influence the behaviour of cells. For instance, the study performed by Kato and Mrksich [77] demonstrated the sensitivity of nucleation rate and the growth of focal adhesion (FAs) of fibroblasts to the type of RGD adhesive ligands (Figure 1-1-A). In this study, the self-assembled monolayers of alkanethiolates attached to tri(ethylene glycol)-terminated alkanethiol molecules was used to expose either a linear or cyclic Arg-Gly-Asp peptide at identical densities to 3T3 Swiss fibroblasts. This study confirmed the importance of controlling the structure of the adhesive ligands. This is in agreement with the report by Xiao and Truskey [78], where a higher cell attachment to immobilized cyclic RGD peptides compared with linear peptides was reported.

In addition to the type, several studies have investigated the importance of the RGD-RGD spacing on cell functions [79-81]. The Figure 1-1-B shows an example of the dependency of cellular performance on different density of RGD ligands on silicon surfaces studied by Gooding and co-workers [81]. In this work, silicon surfaces were coated with undecenoic acid and various ratios of 1-amino hexa(ethylene oxide) monomethyl ether (EO6) to 1-amino hexa(ethylene oxide). The attachment of RGD ligands to hydroxyl groups provided the surfaces with various ligand spacing. The results of this study demonstrated that not only the number of the cells, spreading, adhesion and the migratory ability of endothelial

cells but also the signal transduction efficacy were regulated by presenting variety range of RGD densities.

The impact of the nanoscale order of RGD ligand patterning on the adhesion of tissue cells has been demonstrated. It was first studied by Spatz and co-workers [82], where glass surfaces were modified by gold nanoparticles with ordered and disordered arrangement (Figure 1-1-C). The spaces between nanoparticles on the surface have been modified with PEG-silane (2-[methoxy(polyethyleneoxy)propyl]trimethoxysilane molecules to avoid nonspecific cell adhesion [79, 83]. Gold nanoparticles were coated with c(-RGDfK-)-thiol ligands via thiol groups. The experiments on MC3T3-E1 osteoblasts revealed that integrin clustering and such adhesion induced by RGD ligands depends on the local arrangement of RGD ligands on the substrate while the global average ligand spacing is greater than 70 nm. The fluorescence images with stained actin in Figure 1-1C shows that the cell adhesion and spreading is more pronounced on the surfaces with the disorder RGD nanopattern compared with those for cells on the surface with ordered RGD nanopattern when the ligand spacing is controlled to be similar.

Various cellular functions depend not only on the expression of the RGD ligands but also on the groups surrounding these peptides. Houseman and Mrksich [84] studied the impact of the length of the oligo(ethylene glycol) groups coupled to the self-assembled monolayers surrounding the RGD peptides on cell attachment and spreading. In this work, the average distance separating the glycol groups and the peptide ligand was altered using thiols with either tri-, tetra-, penta-, or

hexa(ethylene glycol) units, while the structure of the background monolayer remained unchanged. The example showed in Figure 1-1D, illustrates the decrease in cell attachment to RGD ligands when the length of the oligo(ethylene glycol) molecules increased. These studies showed the degree of the presentation of adhesion motifs regulates different aspects of cellular behaviour in a very precise manner.

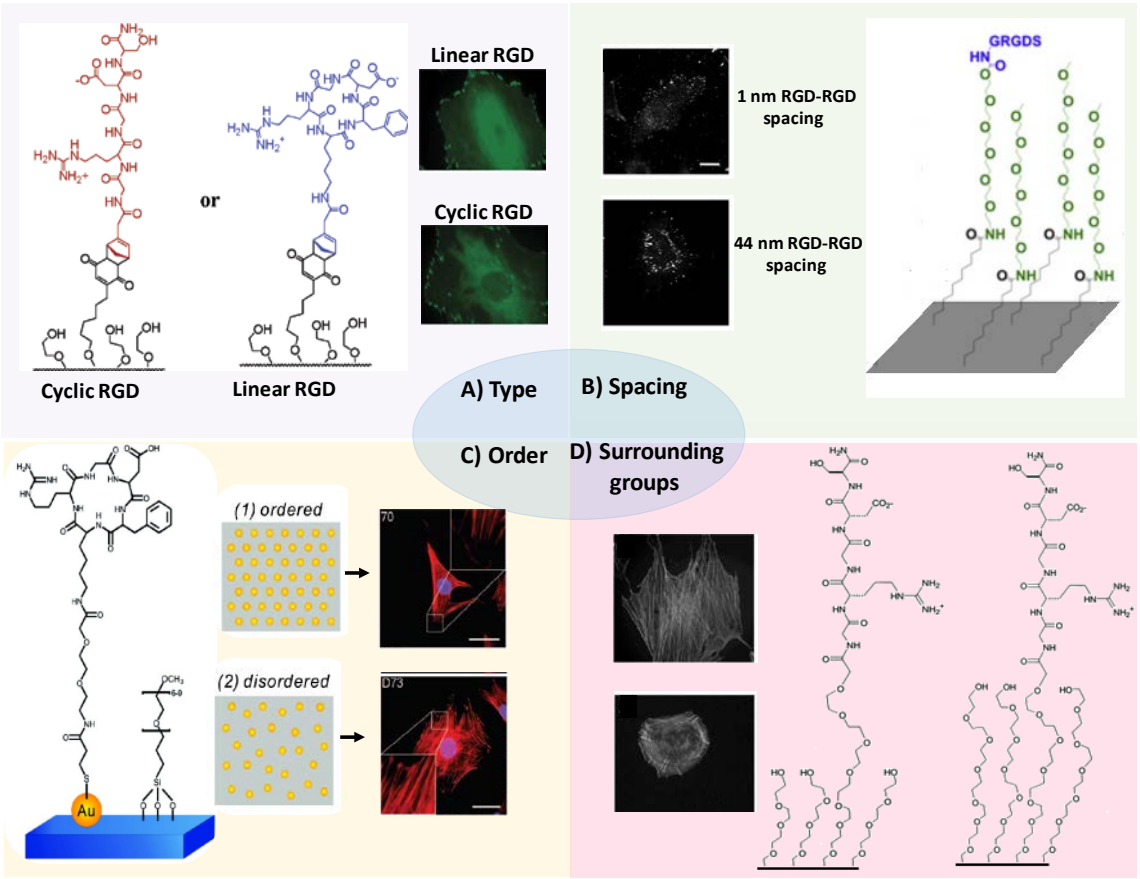

Figure 1-1. Examples of surface chemistries that provide different expression of RGD ligands by controlling type, spacing, arrangement and the surrounding environment with respective fluorescence images. (A) Schematic of the gold surfaces used by Kato and Mrksich [77] where the cyclic or linear cell adhesive ligands are attached to a cell-inert oligo(ethylene oxide) layer. The cyclic RGD provide twice the number of FAs with smaller length in average than that on the surface with linear RGD. (B) Schematic of the silicon surfaces prepared by Gooding and co-workers [81] with different RGD spacing.

The spacing is controlled by altering the concentration of 1-amino hexa(ethylene oxide) monomethyl ether (EO6) to 1-amino hexa(ethylene oxide). Components incorporated into the SAM. (C) Schematic of the glass surface adapted by Spatz and colleagues [82] for the control of ligand density and order presented to cells. By controlling the arrangement of gold nanoparticles, the organization of RGD ligands were defined. The space between the nanoparticles was modified with oligo(ethylene oxide) molecules as a cell-inert layer. The images show 3T3 fibroblast cell with the staining of actin stress filaments. (D) Schematic of the gold surface modified with RGD ligands used by Houseman and Mrksich [84] showing modulated effect of the RGD spacing on cell attachment as the length of the oligo(ethylene glycol) groups altered. Fluorescence micrograph of actin filament of Swiss 3T3 fibroblasts on two surfaces modified with tri(ethylene glycol) group that leaves the peptide ligand more accessible (left) than does the longer hexa(ethylene glycol) group (right)

1.9 READ-OUT SYSTEMS OF CELL-BASED ASSAYS

The cell is the recognition species; the transducer must turn the cell response to an electronic signal. Cells do not do this; therefore, a transducer is selected based on the cellular response of interest to process the cell signal. These transducers are mainly electrical, optical, acoustic or magnetic. The detection methodology is crucial to be selected with care to provide the capability of obtaining the information on cellular behaviour in a relatively comprehensive way with minimum interference with cell activity. Cell-based biosensors can be categorized based on the final readout signals and the second transducer that has been used. Optical and electrical cell-based biosensors are the most documented assays [85-87].

1.9.1 Optical cell chips

Optical cell-based biosensors are mainly label-based methods for measuring changes in luminescence [88-90], fluorescence [91-97] or colour [98] of cells loaded with optical tags. In addition, there are label-independent optical

biosensors that have been recently reviewed by Fang [99] such as surface plasmon resonance (SPR) [100-102], resonant waveguide grating (RWG), dynamic mass redistribution (DMR) [103-105] and photonic crystal optical cell assays [106, 107]. Among different optical instruments, fluorescence microscopy dominates for studying various cellular components and cell responses to stimuli. This is due to its intrinsic selectivity and commercial availability of various fluorescence labelling tools.

Fluorescence cell-base assays

Fluorescence-based assays have become the main technique for answering biological questions on cellular behaviour in response to stimuli. Fluorescence imaging can provide detailed subcellular information at single and population cell levels. Moreover, with the recent advances in the microscopy field, fluorescence microscopy can monitor the alterations of intracellular behaviour at single-molecule level using photoactivated localization microscopy (PALM) [108, 109] and stochastic optical reconstruction microscopy (STORM) [110, 111]. The change in ionic state in cells, (e.g. Ca^{2+} or Zn^{2+}), the exocytosis events, and concentration of different chemical species (i.e. nitric oxide and hydrogen peroxide), cell organelles (i.e. mitochondria and endoplasmic reticulum) and biomolecules (i.e. DNA and membrane lipid bilayer) can be monitored using fluorophores. Different compounds have been used as fluorescence tags including organic fluorophore, natural biological dyes and various fluorescence nanoparticles such as quantum dots [96] and upconversion fluorescent

nanoparticles [112]. Each particular application and biological condition require the use of specific type of fluorophores.

The availability of organic dyes with large spectral range and tuned biological properties has made them the most common fluorophores in cell imaging. Some of these dyes such as fluorescein isothiocyanate (FITC), rhodamine, and recently developed Alexa Fluor® dyes can be conjugated to different proteins and biomolecules such as proteins, antibodies, nucleic acids. Whereas some of these dyes are membrane permeable that targets the specific part inside the cells suitable for live cell imaging. Using acetoxymethyl ester derivatives as cell-permeant dyes is a common method for live cell imaging [113]. For instance, the acetoxymethyl groups in fura 2- acetoxymethyl ester (fura 2-AM) provide the intracellular dye loading in a non-invasive manner. The ester groups of fura 2-AM degrade inside the cell, and the dye becomes polar and Ca^{2+} sensitive (Figure 1-2).

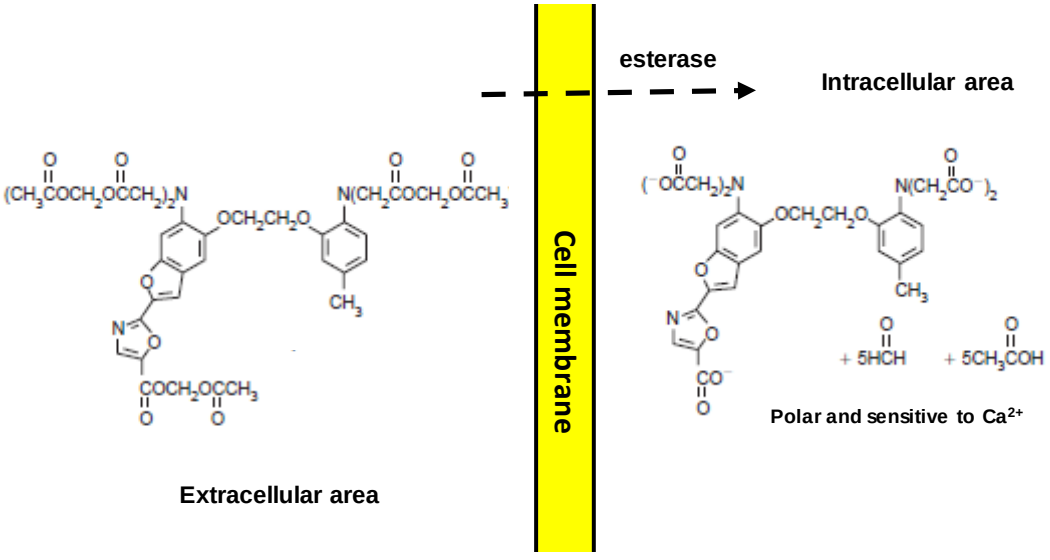

Figure 1-2. The acetoxymethyl ester groups of fura 2-AM make the dye cell-permeable, and dye becomes Ca2+ sensitive in intracellular environment.

Most of the organic dyes in live cell imaging undergo phototoxicity and photobleaching in long-term. For instance, it has been shown that Fluo 4-AM over 1 h of confocal imaging caused phototoxicity. There are studies where the phototoxicity is mentioned as a potential limitation of fura 2 AM, which can restrict the duration of microscopy study effect [114]. However, experimentally Monteith and co-workers [115] have shown that the phototoxicity of fura 2 over short timescales was not a major concern. Thus, the potential phytotoxicity of the organic dyes could be a limitation. In that case, using different microscopy techniques that decrease the exposure time or increase the excitation wavelength such as two-photon microscopy [114], pulsed light-emitting diodes [116] and controlled light exposure microscopy (CLEM) [117] can be considered as possible solutions.

Green fluorescent protein was discovered in jellyfish *Aequorea Victoria* by Saiga and co-workers in 1962 [118]. In the 1990s, the green fluorescent protein (GFP) gene was cloned, and it was demonstrated that the transfer of the gene in other organisms fluorescently mark proteins [119-121]. The high-resolution crystal structures of GFP propose unprecedented insight into the relation between protein structure and spectroscopic behaviour [122]. Many different GFP derivatives such as allophycocyanin, phycocyanin, phycoerythrin, and phycoerythrocyanin were later developed. These biological compounds have been transferred to different mammalian and bacterial cells to monitor the function of particular

proteins. However, the risk of phototoxicity as a result of overexpression of light producing proteins that causes the production of reactive oxygen species is one of the challenges involve with using these biological fluorophores. Slow formation of the post-translational chromophore, the oxygen requirement, and high background fluorescence when the GFP is not highly expressed or densely localized are some other limitations of using GFPs [123]. In addition, fluorescent proteins appear to display lower fluorescence count rate than small organic fluorophores such as rhodamine derivative, and therefore not preferred for super-resolution microscopy applications [124].

The emergence of new fluorescence microscopy methods and instruments such as the developments in laser scanning confocal, two-photon and time-gated microscopies, Förster Resonance Energy Transfer (FRET), fluorescence lifetime

imaging (FLIM), total internal reflection fluorescence (TIRF), fluorescence recovery after photobleaching (FRAP) and fluorescence correlation spectroscopy (FCS), highlights the capability of fluorescence-based methods for advanced future applications among the most powerful monitoring techniques [125]. The future advances are toward improving the 3-D imaging and visualizing the function of cells in deep tissues with minimum auto-fluorescence. Using fluorescence microscopy leads to acquiring extremely precise information at subcellular levels about specific cellular pathways.

1.9.2 Electrical cell chips

Electrochemical biosensing is based on coupling of electrochemical transduction units with biological recognition units, which is the whole cell in cell-based assays. A living cell can be assumed as a dynamic electrochemical unit since many redox reactions and ionic transport normally occur in intracellular environment. Cell-based electrochemical assays have found a wide range of applications in pharmacology, cell biology, toxicology, neuroscience and environmental pollution [126]. Patch clamp, amperometry, impedance and fast scan cyclic voltammetry are the common techniques used in electrical cell-based biosensing assays for various applications. Assessing the changes in electrical current and impedance signals are the two of the most common electrochemical techniques in cell-based assays that in many ways are complementary to fluorescence microscopy.

Amperometry cell-base assays

Measuring the change in current resulted from the electrochemical oxidation and reduction of electroactive species at a constant applied potential, called amperometry [126], is a sensitive method, useful for tracking various intracellular interactions. Amperometry-based methods can provide precise information on the kinetics of secretion and the oxidization of chemical intracellular messengers in the well-controlled biological environment [68]. The amperometry cell-based assays have been used to quantify the exocytosis events in endocrine cells or to detect neurotransmitters where the specific nerve terminal has been stimulated [127-132]. Among the oxidizable species, nitric oxide (NO), adenosine

triphosphate (ATP), and monoamine neurotransmitters such as norepinephrine (noradrenaline), dopamine, serotonin are of particular importance and common in many biological systems [126]. In amperometric techniques, an electrode is placed a few micrometres far from a single cell or population of cells and is used to detect the electron transfer in the limited environment around the cells, which particularly increase the sensing sensitivity [133]. A lot of efforts has been put to design more sensitive electrodes for amperometry measurements [134, 135].

One of the critical applications of amperometry cell-based assays is in detecting exocytosis of secretory vesicles in single cell level and even with the capability of recognition of a single event [136, 137]. Exocytosis of secretory vesicles is an important event for signalling between cells and organs in living elements. Triggered by related stimulators, vesicles containing bioactive molecules such as neurotransmitters, peptides, hormones are transported to interact eventually with the cell membrane at high concentration, which consequent in releasing of the contents of the vesicles into extracellular matrix [138]. The secretory process involves various steps since formation till the mobilization from cell membrane to ECM, which happens incredibly fast. Some steps of exocytosis can be tracked real-time using amperometric recordings with carbon fibre electrodes [130, 139]. Recognition and understating these events and the involved steps are essential in understanding many cell signalling processes.

Amperometry techniques have been widely used to quantify the exocytosis events in different cell types *in vitro* [140-142], *in vivo* [143] and, recently, *in vivo*-like [144] environments. In a recent work performed by Huang and co-

workers [144], a co-culture of superior cervical ganglion neurons and their effector smooth muscle cells were grown in a microfluidic device to simulate the neural network in live complex cells in the laboratory. The schematic of the work is shown in Figure 1-3. In this system, the carbon fibre nanoelectrode was used to measure the amperometric signals, while a glass nanopipette electrode was used to monitor the postsynaptic potential. These electrodes were placed near to smooth muscle cells, while the stimulant that evoked the neuron cells. These amperometry techniques are extremely sensitive as can afford the quantification of a single event in real-time.

The applications of amperometry techniques in cell-based biosensor chips are limited to the events that involve electron transfer mechanisms. On the other hand, the capability of amperometric techniques on providing information on a specific subset of electroactive intracellular reactions will be an issue when the bulk information of the response at whole-cell level is required. Impedance cell-based biosensors, on the other hand, can provide information on the change in cell shape and cell adhesion to the other cells and to the substratum of the whole cell, and subsequently, fail in obtaining detail information on specific electrochemical reactions. In fact, the information acquired using these two techniques are in many ways complementary.

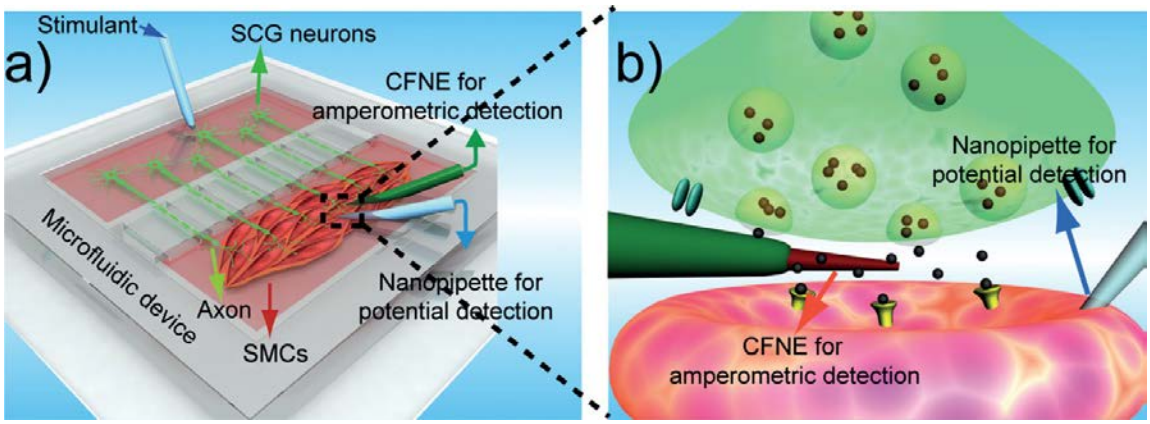

Figure 1-3. a) Representation of in vivo-like neuromuscular junction. b) Schematic of amperometric detection using a carbon fibre nanoelectrode insertion inside a synapse and a glass nanopipette inside a smooth muscle cell for monitoring the post-synaptic potential [144].

Impedance cell-based assays

Electrochemical impedance cell-based sensing (ECIS), was first invented by Giaever and Keese in 1984 [145]. This technique offers instantaneous and quantitative means to study many cellular events, such as cell attachment, spreading, growth, mortality, and morbidity of c cells [146]. In ECIS technique, cells are cultured on the electrode substrates, and a non-invasive weak alternative current of around 4 mA/cm^2 with frequencies usually in the range of 10^5-1 Hz is applied to measure the alterations in impedance signals over time [55]. Since seeding cells, as the attachment and spreading to the electrode happens, the effective open area available for current flow decreases, and, subsequently, impedance value increases. In addition, any external stimuli or internal aberration that changes the cell morphology and cytoskeletal arrangement alter the impedance results. The alteration in cell morphology derives from changes in cell-cell and cell-substrate connectivity. The impedance measurement can detect

the alteration of nanometres in cell diameter and changes in the range of sub-nanometres in the distance between the ventral cells membrane and the electrode surface [147]. The first and most common electrodes that were used in impedance cell-based assays were small gold electrodes on the bottom of a regular tissue culture dishes [147]. Thereafter, the application of other novel metals such as platinum [148] or metal oxides become a common approach. In 2001, indium tin oxide (ITO) was used to study the effect of thrombin on the permeability of endothelial cells recruiting impedance monitoring [149]. The first application of ITO in cell-based assays goes back to the work done by Schwalm and co-workers [150] to record spike potential of many neuron cells. In 1995, Watanabe and colleagues [151] confirmed that culturing primary adrenal chromaffin cells on ITO electrodes keep the cell function not interrupted. In order to improve the sensitivity of the impedance measurements, interdigitated electrodes were offered first by Wolf and co-workers [152] by introducing interdigitated platinum film, PhysioControl-Microsystem (PCM®). In 2004, using gold interdigitated electrodes to develop the real-time cell electronic sensing (RT-CES®) for detecting cell-based parameters was reported by Zheng and co-workers [153]. RT-CES® system became the predecessor of a new technique which is now on the market through Roche referred to as xCelligence with improved functionality compared with RT-CES® [154]. Impedance cell-base assays have been used in various applications ranging from studying the micromotion, shape and spreading of cells over time or cell responses to different physical and soluble cues [155].

The common impedance cell-based techniques such as xCelligence need a high population of cells per well per measurement. The large number of cells that propose more coverage on the electrode, substantially, improves impedance characteristics of the sensor and provide the tool with higher sensitivity for the recognition of small cellular alterations induced by external cues such as drugs or toxins [156]. Recently Zhang and co-workers [156-158] have demonstrated a single cell-based impedance assay on gold electrodes. These assays are based on, firstly, designing the underlying electrode as small as the size of a cell to achieve a full-covered surface and, secondly, providing covalently-bound adhesive peptides on the surfaces to provide the tight cell-surface connections. Single cell-based sensors circumvent the contribution of cell-cell adhesion in changing impedance, and therefore, make the fundamental studies on cell-surface adhesion possible [156].

In addition to high-throughput impedance information, different mathematical and circuit models can be applied to extract detail information about cell morphology and average cell-cell and cell-surface adhesion [147, 159]. The following sections introduce the way that impedance data on cells can be used to investigate the cell attachment and adhesion over time in addition to extracting adhesion and morphological information by modelling the results (part A) as well as how the response is regulated in the presence of physical cues (part B) or soluble signals (part C).

A) Study cell attachment and spreading using impedance cell-based assays

Cells generally in suspension retain the round shape, and when they found the appropriate interface they start to interact by initial contact or attachment. Subsequently, attached cells undergo morphological alterations and increase their contact area with the surfaces, known as spreading, followed by going through proliferation stage. The spreading and growth states of cells are very crucial parameters that need to be precisely investigated during cultivation. Impedance spectroscopy can detect the minute changes in cell attachment to the surface and the cell coverage on the surfaces in real-time of many cells at the same time. Figure 1-4 illustrates the schematic of detecting different stages of cell growth using impedance measurement.

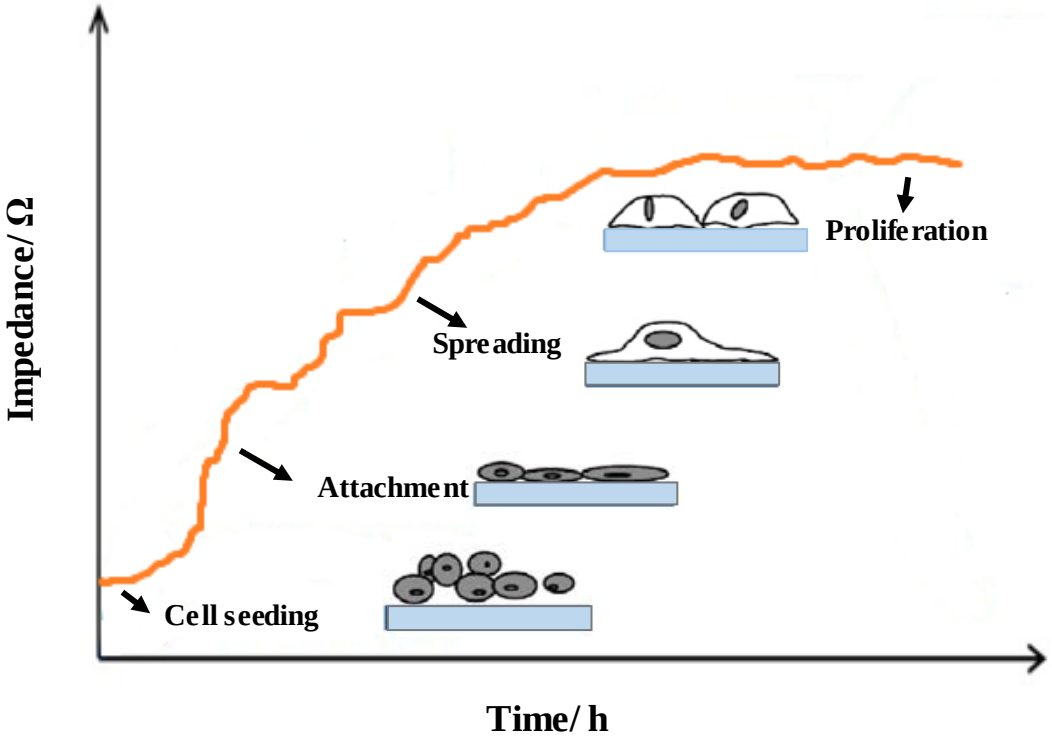

Figure 1-4. Schematic of the change in impedance value when various stages of cell attachment and spreading occur over time.

The compatibility of impedance measurement with many different adherently growing cell types such as bacteria [53], mammalian cells [160], stem cells [161] and even insect cells [162, 163] has been confirmed. Designing the experimental setup is a very crucial step before testing various cellular responses using impedance spectroscopy. The impedance response is sensitive to the cell type, species of origin, passage numbers, seeding density and cell culture on the electrode array [55]. The impedance value also depends on the frequency, and current chooses to cross through or between cells based on the applied frequency. Figure 1-5 illustrates the current behaviour at low and high frequencies with the equivalent circuit models that can be approximated for these systems. If the whole cell-based design is assumed as an electrical circuit (Figure 1-5C); live cells can be assumed as a resistor in series with a capacitor. The resistor and capacitor are modelling the intracellular spaces and lipid membrane of cells, respectively. The practical contribution of cell units in changing impedance is dominated by the cell membrane. Thus the cell can be approximated as a capacitor (C_m).Moreover, the cell/electrode interface in the cell media is approximately defined as a constant phase element (CPE), as it displays a non-ideal capacitive behaviour. The capacitive behaviour of cell-surface is due to the accumulation of ionic species at this interface. The area beneath the cells and the cell-cell junctions can be approximated as resistors represented with $R_{cell\text{-}cell}$ and $R_{cell\text{-}surface}$, respectively [164]. At low frequencies, the capacitance of cells becomes highly resistive, and the current mainly pass from the spaces between cells. Whereas in the high-frequency range, the membrane capacitance becomes negligible, and the current

can enter the intracellular area by passing through the membrane. Therefore, the measurement at high frequencies is more sensitive to cell spreading.

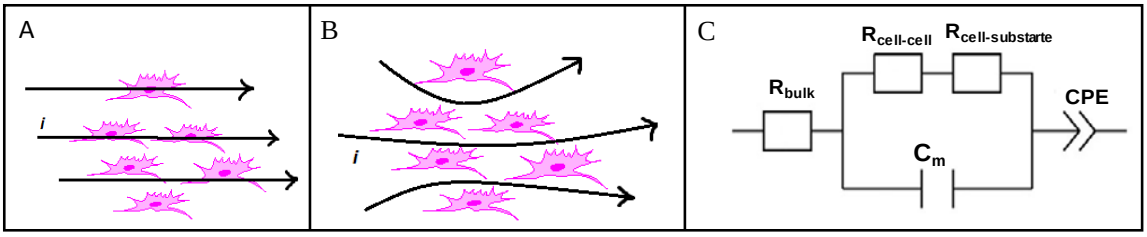

Figure 1-5. (A) At high frequencies, current crosses the cell membrane and enter the intracellular space. (B) At low frequencies, lipid membrane prevents the current to enter inside the cell. (C) Cells on the electrode surface can be approximated by a circuit model where C_m refers to the cell membrane, $R_{cell-cell}$ and $R_{cell-surface}$ represent the resistance in the cell-cell and in the gap between cells and the surface, respectively. R_{bulk} relates to the resistance of the extracellular area, and CPE describes the media/ surface interface property.

The impedance of the cell-free electrode either before seeding cells or after detaching cells at the end of the experiment has to be measured in a cell-based impedance measurement. This value is used during data analyses to normalize the impedance results. The normalized impedance values are obtained by dividing the acquired impedance of cell-covered electrode over time into the impedance of the cell-free electrode. The normalization process removes the effect of media and media/surfaces interferences in the obtained data. The impedance measurement for a cell-free electrode at low frequencies is dominated by the electrode capacitance and in high-frequency ranges; the ohmic resistance of the bulk phase dominates.

The frequency resolved impedance data of cell-free electrode and cell-covered electrodes can be used to obtain useful morphological information about cell shapes and identify the contribution of change in cell-surfaces, cell-cell adhesions and cell membrane capacitance in altering the impedance values using a

mathematical model developed first by Giaever and Keese [147, 165]. In this model, the current is assumed to flow radially into the space between the cell`s ventral side of cells membrane and the substrate and escapes between cells. In addition, the current density is assumed to be consistent in vertical "z" direction. According to this model the specific impedance for a cell-covered electrode can be written as has been shown in equation 1 [147, 159].

Equation (1):

$$\frac{1}{Z_c} = \frac{1}{Z_n}\left(\left(\frac{Z_n}{(Z_n + Z_m)}\right) + \left(\frac{\left(\frac{Z_m}{(Z_m + Z_n)}\right)}{\left(\frac{\alpha\left(\sqrt{\frac{1}{Z_n}+\frac{1}{Z_m}}\right)\left(I_0\left(\alpha\left(\sqrt{\frac{1}{Z_n}+\frac{1}{Z_m}}\right)\right)\right)}{2I_1\left(\alpha\sqrt{\left(\frac{1}{Z_m}+\frac{1}{Z_n}\right)}\right)}\right) + R_b\left(\frac{1}{Z_n}+\frac{1}{Z_m}\right)}\right)\right)$$

Where I_0 and I_1 are modified Bessel functions of the first kind of order 0 and 1. Z_n ($\Omega.cm^2$) is assumed equal to constant phase element (CPE), impedance associated with electrode/electrolyte interface, measured as the impedance of the cell-free electrode at different frequencies. Z_c ($\Omega.cm^2$) is the specific impedance for cell-covered electrode obtained experimentally. α and R_b are describing the contribution of cell-surface and cell-cell adhesions in defining the total cell-covered impedance. As the values of α and R_b are dependent on modified Bessel function, they cannot be explicitly solved and have to be obtained by curve fitting.

The resistance of the media (R_{bulk}) value need to be subtracted from the measured impedance before the calculations and then will be added back for comparing the experimental and calculated data. To precisely detect this value running measurement in higher frequencies is recommended [166]. Z_m ($\Omega.cm^2$) is cell impedance dominated by membrane capacitance (C_m) as is shown in (Equation 2).

Equation (2):

$$Z_m=1/2\pi fC_m$$

In the described model, cells are approximated as disk-shaped objects of the radius of r_c having insulating membrane surfaces and filled with conducting electrolyte. The cell morphological parameters can be obtained using the calculated value of α according to (Equation 3).

Equation (3):

$$\alpha = r_c\sqrt{\rho/h}$$

Where r_c (μm) is the assumed cell radius, ρ (Ω.cm) is the specific resistivity of the cell culture medium, and h is the average height between the basal cell surface and the substratum. ρ is a temperature sensitive parameter and is commonly measured using a simple conductometer in cell culture media. It is worth mentioning the model later was extended to the conditions that cell morphology is more logical to be assumed as rectangles and not disks [167].

The attachment and spreading of cells on the surface can be regulated by the presence of different physical cues on the surfaces or various soluble molecules

that interfere with cell adhesion and morphology. This dynamic regulation can be monitored using impedance cell-based assays in a label-independent and sensitive manner.

B) Study the effects of physical cues using impedance cell based assays

Mammalian cells adhere and interact with ECM, and this interaction is vital for many of cell functions. ECM composed of proteins such as collagen and fibronectin that contain RGD adhesive ligands. These ligands are the responsible for cell adhesion as was explained in section 1.2. In cell-based assays, the ECM function is mimicked by coating the surfaces with ECM proteins or RGD molecules. Many aspects of cell behaviour depend on the expression of these physical cues of their underlying substrate as was discussed in section 1-5. For instance, cell attachment and spreading are among the cell functions that become regulated by the molecules immobilized on the surface. Understanding the cell-surface interactions is crucial in order to optimize these interactions and achieving a more comprehensive view of cell-ECM connections.

A rather limited number of instruments and experimental methodologies offer the possibility of studying the cell-substratum interactions quantitatively. The majority of techniques to measure the strength of cell-substrate adhesion are based on centrifugal acceleration [168, 169] or exposing the anchored cells to laminar shear stress [78]. In these methods, a mechanical force is applied to detach cells from the substrate and counting the number of cells that have resisted the force and stayed connected. Another common method to quantify cell-substrate force is using an atomic force microscope [170] that measures the force

required for the detachment of a single cell from the substratum. An additional challenge is to measure how such physical cues influence cell response even if the magnitude of the adhesive forces is known. In some cases, optical microscopy techniques are employed to investigate the cell density, cell morphology or quantify the focal adhesion points and relating that to cell adhesion to the surface. The adhesion process of mammalian cells on artificial surfaces is a time-dependent process [171]. Endpoint methods that need to separate the cells from the surface or pre-treating cells require stopping the cell attachment or adhesion process.

Recruiting of label-free and non-invasive methods enable in situ monitoring of the cell attachment and adhesion processes over extended periods of time. The excellent time resolution of impedance cell-based assays provides the potential for an in-depth investigating on the kinetic of attachment and spreading of cells in response to different physical cues offered by the surface coatings. For instance, by employing impedance measurement, it has been shown that coating the substrate with cell matrices derived from different cell lines including astrocytes, pericytes, and endothelial cells, alter the kinetic of change in the resistance values of cerebral endothelial cells and ultimately their barrier function [172]. In addition to employing different types of ECM, the presence of different concentration of ECM proteins such as fibronectin also was shown to regulate the kinetics of cell adhesion to the microelectronic arrays as was detected using RT-CES® system [57]. In a study by Giaever and co-workers [173] the attachment and spreading of Madin–Darby canine kidney (MDCK) epithelial

cells to gold electrodes coated with different proteins has been studied. It was shown that the capacitance measured at 40 kHz reflect the cell attachment and spreading in a linear way on surfaces coated with different proteins on gold electrodes. The data demonstrated that a significantly faster kinetic of cell attachment and spreading on the surfaces modified with fibronectin occurred compared with cells on surfaces with vitronectin, laminin, or bovine serum albumin coatings. In addition to studies run in cell media, a Faradaic impedance measurement [174] also has been used to examine the cell adhesion to surfaces modified with different proteins. The results confirmed a linear relationship between cell adhesion rate and the specific resistance of the cell layer to negatively charged examined protein.

The RGD adhesive peptides immobilized electrodes have been employed to provide a well-controlled environment in impedance cell-based assays [157, 175]. However, how the expression of adhesive ligands, the spatial distribution of these peptides in particular as an example, influences the kinetic of cell attachment and spreading has not been studied.

C) Study the effects of soluble cues using ECIS

It has been demonstrated that minute changes in cell adhesion and spreading influence the impedance signal characteristics significantly. These alterations can be caused by soluble cues such as pharmacons, toxins, food molecules, and biomaterials that interfere with cell shape and adhesion. Therefore, impedance measurement has the capability of recognizing the cell responses to various soluble signals. For instance, it has been shown that the addition of β-agonists

(isoproterenol, forskolin, IBMX) [160] or cAMP [166] lead to the increase in resistance value due to strengthening the cell-cell junctions, while agents such as β-antagonists (proterenol) [160] or thrombin [149] decrease the impedance value because of increasing the cell permeability and raising the gap between neighbouring cells. In another example, the apoptosis induced by cycloheximide (CHX) has been monitored using impedance measurement, and it was shown that the disassembly of cell-cell tight junctions precedes the alteration in cell-surface adhesion and correlate well with the time course of protease activity [176]. Real-time impedance measurement using the whole cell have been used to study the effect of various soluble agents on cells in many different applications such as environmental pollutant monitoring, drug discovery, and cytotoxicity assays and study cellular functions including cell differentiation [39, 154, 177-179]. Impedance cell-based systems have been used to perform cytotoxicity assays on different fibroblasts, human hepatocellular carcinoma cells, human colon adenocarcinoma or cells from kidneys of monkey [180-183].

A large population of drugs interferes with cell shape and morphology or cell viability, therefore the capability of impedance measurement to monitor the cell functions in long-term in a non-invasive and label-free manner offers it as one of the prominent tools for drug discovery and drug screening applications, in particular through screening the activity of GPCRs [55, 184, 185]. These receptors can be targeted by soluble cues such as drug molecules, hormones, neurotransmitters, cytokines, growth factors or nutrients and some adhesive cues such as cell adhesive ligands. More than half of all current drugs and nearly one-

quarter of the top 200 best-selling drugs target G-protein-coupled receptors (GPCRs) to regulate the cell function [186]. Because of the enormous economic impact of drugs, companies are interested in developing methods and new techniques for high throughput screening of GPCRs. One way is monitoring the response of second messengers upon agonist stimulation [187]. Examples include measuring intracellular calcium flux [188]. Stimulation of GPCRs activates phospholipase C (PLC), which hydrolyzes phosphatidylinositol bisphosphate (PIP2) to form two second messengers, inositol 1,4,5-triphosphate (IP3) and DAG. DAG activates protein kinase C (PKC), and IP3 activates the IP3 receptor on the endoplasmic reticulum resulting in an efflux of Ca^{2+} from the endoplasmic reticulum to the cytoplasm and an elevation of intracellular Ca^{2+} [3]. Calcium ion concentration can be readily detected with a variety of organic fluorescent dyes and calcium sensing proteins. The activation of GPCRs is, often, associated with alterations in cytoskeleton arrangement [69, 189]. It is shown that these alterations in cell morphology and adhesion induced by GPCRs stimulators cause the change in impedance signal [184, 190, 191]. One of the significant advantages of impedance cell-based sensing in drug screening over techniques such as fluorescence microscopy is its capability to track cellular responses for long-term without interfering with cell functions. This addresses one of the critical issues in cell-based drug screening assays of finding the endpoint where the effect of the potential therapeutic compound becomes evident. The time duration of the exposure to understudy compounds depends on the specific goal of the screening. The brief incubation time of the cells with the drug may be used to detect the

acute toxicity and necrotic influences or to measure the signal transduction which usually takes a few seconds to minutes to be generated and measured. Commonly, the exposure of several days is necessary to examine the effects of the agents on cells proliferation, migration or differentiation. Figure 1-6 illustrates the common scheme of testing the effect of compounds on live cells using a label-based screening approach. Most of the fluorophore and luminescent dyes and viability indicators exhibit toxicity properties after a rather short time of incubation with cells, usually between 0.5 h to 1 h. Some of the viability markers such as ATP and apoptosis indicators such as caspase may be expressed transiently and are detectable only within limited time duration [86]. The majority of the fluorescence dyes quench the fluorescence in a limited time window. These together highlight the importance of developing the label-free screening methods, such as impedance-based ones, that measure the effects of the test compound in real-time. Additionally, label-free methods reduce the risk of artifacts resulted from the interaction of the examined compound with assay chemistry.

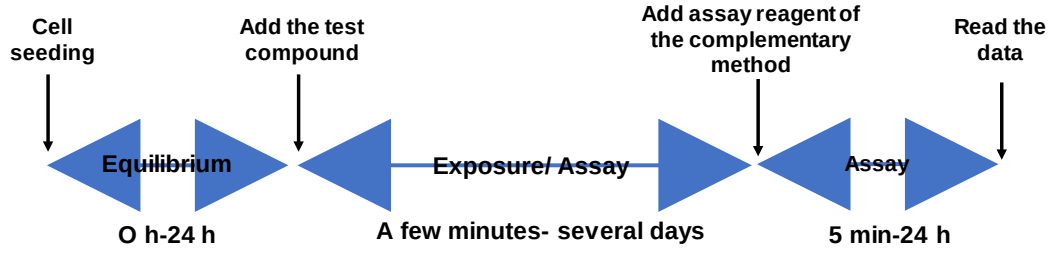

Figure 1-6. General scheme representation labelled-based approaches to examine the effect of various compounds on live cells.

Two important points need to be considered while planning to use impedance cell-based techniques to investigate the cellular functions to environmental signals.

First, the knowledge of how the presence of physical cues may regulate the dynamic cellular response to different soluble cues is quite in its infancy. The surface of a cell chip should have a well-controlled environment both chemically and physically. In fact, by providing more *in vivo*-like cell environment, the *in vitro* screening models could address the growing concerns about the lack of efficacy or unexpected side effects which lead to drug failures [192]. As was indicated the modification of cell interfaces in cell-based tools with controlled exposure of RGD adhesive ligands is a solution.

Second, the provided information by impedance measurement is an ensemble data. The subcellular information that can help in undersetting both the impedance results and the cell behaviour is not possible to be interpreted from impedance measurement solely. Another unique challenge involved with using label-free systems, such as impedance cell-based sensing techniques, is the possibility that the activation of multiple signalling pathways with opposing influences can result in a lack of overall response, leading to a false outcome [193]. One solution will be developing more sophisticated devices by combining the impedance measurement with other traditional techniques such as optical microscopes. Such an approach would enable a more comprehensive insight into cellular responses.

It seems that the combined devices are becoming increasingly implemented in applied and basic assays on cellular behaviour aiming at gaining more biological insight on cellular responses at different time scales and locations. This combination also can cover some of the challenges associated with using optical cell-based biosensors. Optical microscopy is limited to the numbers of cells in the field of view, and thus may fail in imaging many cells at the same time. The cells cultured *in vitro* display heterogeneous behaviour even when cultured under controlled condition [86]. The response of all cells under the culture to a stimulus may not be synchronized. The time to response may vary depending on the concentration, volume and the duration of the exposure of the chemical compound which can alter the drug diffusion rate. In combination with appropriate strategies on engineering the surface chemistry, the coupled techniques can aid to achieve a more comprehensive view of the effect of soluble and physical cues on cell functions.

1.10 RESEARCH AIM AND THESIS OUTLINE

Live cells respond to various signals that they are subjected to in their environment, and the way they choose to react, often, determines their fate. These signals are vary in time scale and space. The mechanisms behind the responses are even more complicated as physical properties of the surrounding environment (adhesive cues), such as ligands in the extracellular matrix (ECM), also play a major role in signalling processes and the overall cells responses. Specifically, the Arg-Gly-Asp ligands present in ECM have been mainly known for

determining the extent of the cell attachment and spreading in its environment through binding to cellular integrins. Most of the current methods of monitoring cell responses provide an incredible way to monitor just specific steps of the whole cellular event. This study was aimed at developing a dual optical microscopy and impedance cell chip for monitoring cellular responses to soluble cues. This helps in finding the possible correlation between intracellular events such as Ca^{2+} signalling and change in cell cytoskeleton in response to soluble cues. In addition, this study was aimed to achieve a more comprehensive view of cellular responses to soluble cues in the presence of different expression of adhesive ligands. In order for these goals to be accomplished, the study started off by examining and modifying various substrates that are compatible with electrochemistry measurements. In the earlier parts of the research (**Chapter 3**), the surfaces of gold electrodes have been coated with low impedance and antifouling coatings. The layers were assessed for their ability to limit nonspecific proteins adsorption using fluorescence microscopy and electrochemical impedance spectroscopy. Although gold is the most common surface for bioelectrical measurements, it was decided to change the interface for the dual cell chip application as gold quench the fluorescence. In addition, for transmitted optical microscopy applications such as phase contrast microscopy, the transparency is a prerequisite. In **chapter 4**, as a transparent and conductive interface, indium tin oxide (ITO) electrodes were modified with controlled density of Arg–Gly–Asp (RGD) adhesive ligands. The RGD spacing on these surfaces was estimated, and the regulation of cell enumeration and spreading

based on RGD spacing was demonstrated using fixed-cell fluorescence microscopy. A Simultaneous setup for running simultaneous live optical microscopy and impedance spectroscopy were designed based on interdigitated ITO electrodes to monitor the dynamic of attachment and spreading of cells on the surfaces. The results also were used to coordinate the impedance data with the amount of cell coverage on the surface. **Chapter 5** illustrates the application of the dual readout system using live fluorescence microscopy and impedance spectroscopy to investigate how surface chemistry influences the signalling pathways that are stimulated by soluble cues and cell adhesion pathways. G-protein coupled cell receptors were used as the pathway interrupted with soluble cues, histamine model drug, inducing changes in cell shape, intracellular signalling (e.g., calcium signalling) and remodelling of cell adhesion to the substratum all with significantly different time scales. This part of the study highlights the importance of controlling the cellular adhesive environment on cell response to chemical cues in a quantitative and dynamic manner. **Chapter 6** demonstrates the developed cell chip efficacy to acquire biological information by screening the effect of potential therapeutical compounds cells. The impedance spectroscopy on interdigitated ITO surfaces was used to detect the useful time window of a potential antifibrotic agent on primary human cells. There is no other reported method to screen the potential antifibrotic compounds on live cells in real-time. The microscopy analyses performed afterward provided quantitative subcellular information on the effects of the examined agent at

individual cell level as well as confirming the validity of using impedance spectroscopy for such applications.

This study demonstrates the requirements of making a simultaneous opto/electrical cell chip and highlights the power of the dual approach in screening the cell behaviour toward soluble cues in the presence of adhesive cues.

CHAPTER 2

EXPERIMENTAL PROCEDURES AND METHODS

2.1 MATERIALS

2.1.1 Chemicals

All chemicals, unless noted otherwise, were of analytical grade and used as received. Dichloromethane, ethyl acetate, and ethanol were redistilled prior to use. Sodium nitrite, potassium chloride, potassium dihydrogen phosphate, dipotassium hydrogen phosphate, potassium ferricyanide, potassium ferrocyanide, O-(2-mercaptoethyl)- O'-methyl-hexa(ethylene glycol) ($C_{12}H_{32}O_7S$), 1-dodecanethiol ($C_{12}H_{25}SH$), albumin_fluorescein isothiocyanate conjugate (FITC-BSA), N-hydroxysuccinimide (NHS), carbon disulphide, 16-Phosphohexadecanoic acid of 99.5% purity (PHDA), dichloromethane, Potassium carbonate (K_2CO_3), N,N′-disuccinimidyl carbonate (DSC), 4-(dimethylamino)pyridine (DMAP), Hoechst (33342), ethylene glycol tetraacetic acid (EGTA), anhydrous dimethyl sulfoxide (DMSO), histamine and methanol were purchased from Sigma- Aldrich (Sydney, Australia).

Fura-2/acetoxy-methyl ester (Fura 2-AM) (10 × 50 μg), 16% paraformaldehyde, triton x 100, phalloidin-Alexa488 (A123779), pluronic F-127, Dulbecco's modified eagle's medium (DMEM), phenol red-free DMEM, Dulbecco's phosphate buffer saline (DPBS), nutrient mixture F-12, PBS, fetal bovine serum (FBS), Alexa Fluor 488 conjugated secondary goat anti-mouse antibody and Fluorobrite were purchased from Invitrogen (Sydney, Australia).

Hydrogen peroxide, hydrochloric acid (32%), sulfuric acid (98%), and chloroform were obtained from Ajax Finechem. (Sydney, Australia). 4-

Aminophenyl phosphorylcholine ($C_{11}H_{19}N_2O_4P$) was bought from Toronto Research Chemicals Inc. (North York, Canada), 1-(3-dimethylaminopropyl)-3-ethylcarbodiimide hydrochloride (EDC, 98 %) and dl-thioctic acid (a-lipoic acid, 98%) were purchased from Alfa Aesar Inc. (Heysham, UK). The antifouling molecules 1-aminohexa(ethylene oxide) (H_2N-EO_6-OH) and 1 aminohexa(ethylene oxide) monomethyl ether (H_2N-EO_4-OCH_3) were obtained from Biomatrik Inc (Jiaxing, China) . Peptide GRGDS was from Genscript (Sydney, Australia). Hank's buffered salt solution (HBSS) was purchased from Gibco® (Eggenstein, Germany). Mouse anti-human collagen I monoclonal primary antibody and mouse monoclonal IgG1 were purchased from Santa Cruz Biotechnology (Santa Cruz, CA, USA). Ficoll PM 400 and 70 were from GE Healthcare (Buckinghamshire, UK). TGF-β1 was purchased from R&D Systems Inc (Minneapolis, MN, USA).

2.1.2 Electrodes

Glassy carbon (GC) (3.0 mm diameter disk) and polycrystalline gold (1.6 mm diameter disk) electrodes were obtained from CH instruments Inc. (Austin, TX, USA). Gold-coated polyester films were purchased from Materio Inc. (California, USA) and used for X-Ray photoelectron spectroscopy (XPS) and fluorescence microscopy studies in chapter 3.

Plain Indium tin oxide (ITO) surfaces were from SPI (Pennsylvania, USA). Interdigitated indium tin oxide (ITO) electrodes were purchased from ALS Co., Ltd (Tokyo, Japan). The interdigitated indium tin oxide (ITO) electrodes that were used in this study consist of 65 pairs of finger electrodes with 10 μm width

and 5 μm spacing between each electrode and approximately 100 nm thickness on rectangular AT-cut quartz crystals of around 0.45 mm thickness. An insulating Novolac resin-based membrane on the surfaces confines the sensing area to the interdigitated working electrode.

2.2 SYNTHESIS

2.2.1 Preparation of dithiocarbamate phenyl phosphorylcholine solution

Dithiocarbamate phenyl phosphorylcholine solution was prepared by following a method presented by Zhu et al. [194]. Briefly, a 5 mM amine solution was prepared by dissolving an appropriate amount of phenyl phosphorylcholine (PPC) in 40 μl Milli-Q water and the addition of 3 ml ethanol followed by degassing for 15 min with argon. Then, this solution was treated with dithiocarbamate (CS_2), agitated, and bubbled with argon for 30 min to create a 2 mM CS_2 solution. In this method, CS_2 works as the limiting reagent to minimize the side products formation, and excess amine acts as a basic agent to increase the efficiency of the reaction of amine groups with CS_2.

2.2.2 Synthesis of lipoamide PPC

The synthesis route of PPC-lipoamide molecule is shown in Schematic 2-1. To synthesize lipoamide PPC, an aqueous solution containing 2.5 mM PPC with one equivalent EDC, two equivalents NHS and 1.1 equivalents α-lipoic acid was mixed and stirred vigorously. Thin layer chromatography on silica was used to monitor the progress of the reaction. The reaction was stopped after 10 h. The

water was removed by adding anhydrous ethanol and using a vacuumed rotary evaporator at room temperature. The product was purified by flash chromatography on a silica column using a mixture of water, ethanol, and chloroform (0.5:2:1.3). Thin layer silica chromatography and 1H NMR (MeOD, 300.2 MHz) was used to characterise the final product.

The retention value (R_f) for the product was 0.44 using this mixed eluent. The product was visualized as dark spots under UV, and as blue spots after dipping the silica plate into AMCS solution, which contains ammonium molybdate, cerium sulphate and sulfuric acid (10%). The final white compound was characterized using 1H NMR (MeOD, 300.2 MHz) (Figure 2-1): δ 1.15-1.35 4H, 1.42-1.95 5H, 2.33-2.55 5H, 3.18 9H, 3.62 2H, 4.34 2H, 7.18 2H, 7.49 2H and 31P NMR (HZ) δ -7. The solution of the synthesized lipoamide molecules in methanol was used to prepare gold modified surfaces with lipoamide PPC layer.

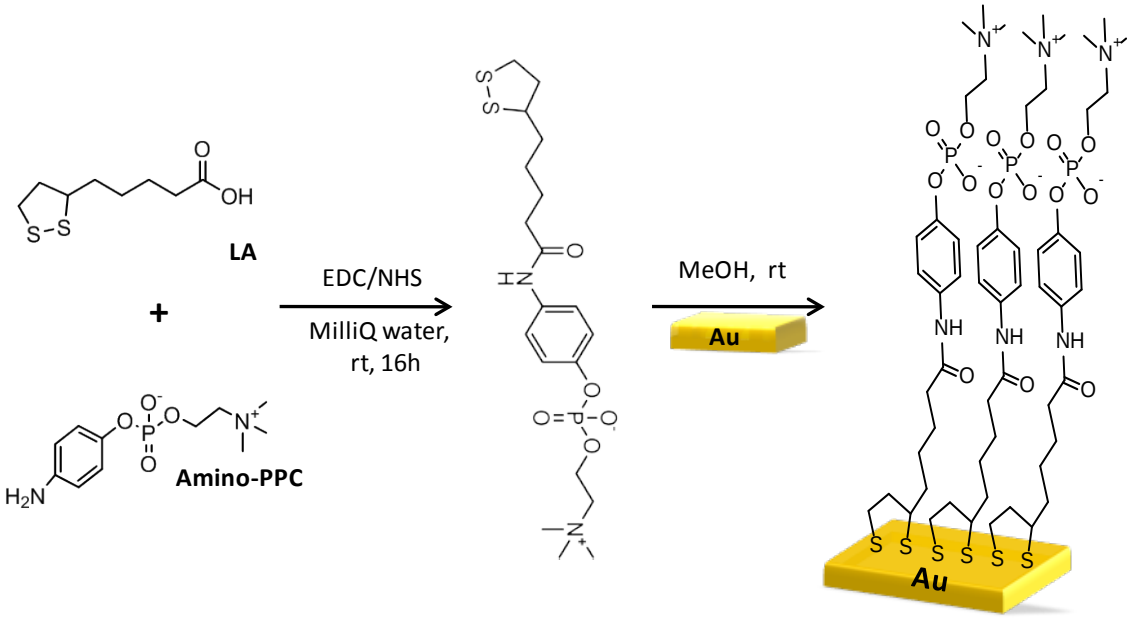

Schematic 2-1. Process of coupling 4-amino phenyl phosphorylcholine to α-lipoic acid to produce lipoamide PPC using EDC/NHS zero-length crosslinkers, followed by

modification of gold surface using the prepared zwitterionic lipoamide PPC molecule. The reaction was run at room temperature (rt).

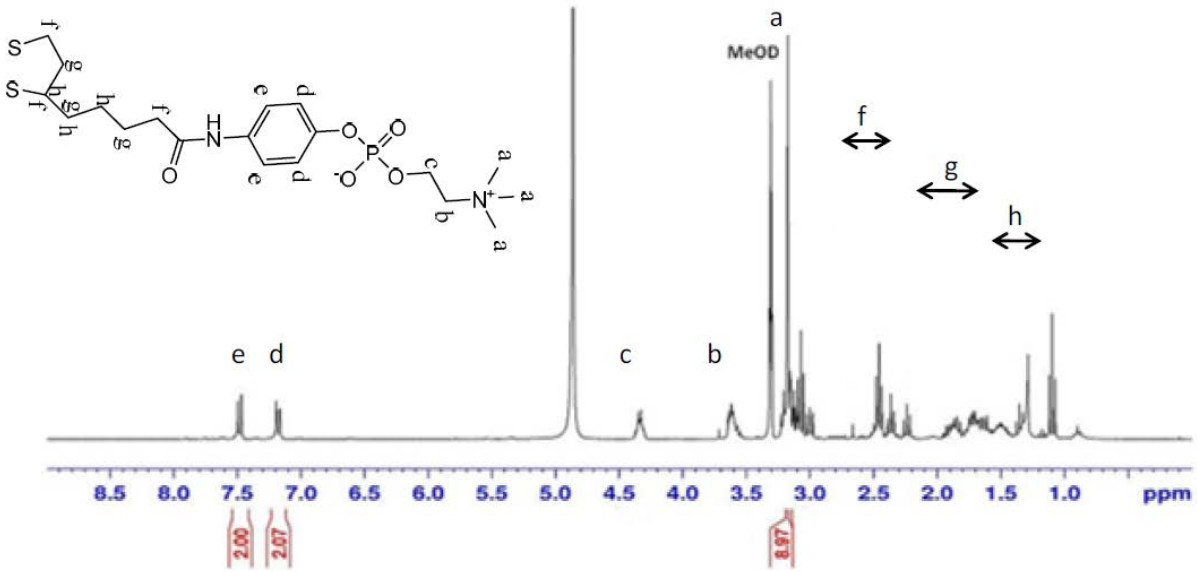

Figure 2-1. The ^{1}H -NMR spectra of the synthesized lipoamide PPC molecule the structure of the molecule and related important peaks. The formation of lipoamide PPC molecules (the structure is shown in the picture) were verified by ^{1}H NMR spectra.

2.3 SURFACE MODIFICATIONS

2.3.1 Electrodes cleanings

Gold and glassy carbon electrodes were polished with alumina slurries of 1.0, 0.3, and 0.05 mm on micro cloth pads. The GC electrodes were thoroughly rinsed with Milli-Q water after polishing and were dried under nitrogen gas. For XPS characterization and fluorescence microscopy studies, glassy carbon plates were used. The GC plates were cleaned in the same way as was performed for disk electrodes. The polishing of gold electrodes was followed by electrochemical cleaning in 0.05 M H_2SO_4 by cycling the potential between -0.1 and 1.5 V (vs.

Ag |AgCl|KCl (3 M)) until a reproducible voltammogram was obtained. Gold-coated polyester films were cleaned by rinsing with ethanol followed by immersing for 1–2 min in piranha solution (a 1:3 mixture of 30% hydrogen peroxide solution and concentrated sulphuric acid) followed by rinsing with copious amounts of Milli-Q water. The piranha solution was left to cool down to room temperature before use to avoid damaging the polyester films.

Caution: piranha is extremely powerful oxidiser and potentially explosive in contact with organic materials and therefore should be handled with extreme care.

ITO surfaces were first cleaned in an ultrasonicator with dichloromethane and then methanol for 10 min each, followed by sonication in 0.5 M K_2CO_3 and in a 3:1 methanol: Milli-Q water mixture for 30 min to remove any residual organic contaminants. The surfaces were then rinsed with copious amounts of Milli-Q water followed by methanol. To clean interdigitated ITO surfaces, the surfaces first were rinsed with copious amounts of Milli-Q water and methanol and then were placed in an oxygen plasma cleaner (Harrick Plasma Cleaner/Sterilizer PDC-32G, Ossining, NY) for 5 minutes after being dried under a stream of nitrogen.

2.3.2 Electrochemistry of reductive adsorption of *in situ* generated PPC diazonium salt

The modification of gold and glassy carbon (GC) electrodes with PPC was performed using the electrochemical reduction of 4-aminophenyl phosphorylcholine diazonium salt on the surface. The electrochemical

modification of electrodes was performed in a deaerated aqueous solution of 5 mM PPC and an equivalent amount of $NaNO_2$ and 0.5 M HCl by cycling potential for five times between 0.2 and -0.6 V at a scan rate of 0.1 Vs^{-1}.

2.3.3 Modification of gold electrodes with dithiocarbamate PPC, lipoamide PPC, 1-dodecanethiol (C12) and O-(2-mercaptoethyl)-O'-methyl-hexa(ethylene glycol) (OEG)

To form Au/dithiocarbamate PPC, the clean gold electrodes were soaked in the freshly prepared solution of 2 mM dithiocarbamate PPC in ethanol for 16 h. To construct Au/lipoamide PPC, gold electrodes were incubated in 2 mM solution of lipoamide PPC in methanol for 16 h. Gold electrodes were soaked for 12 h in 1 mM OEG and C12 solutions in ethanol to form OEG and C12 SAMs on the surfaces, respectively.

2.3.4 Preparation of ITO surfaces modified with different RGD densities

A multi-step strategy was followed to modify the surfaces chemically with RGD molecules with defined spacing. A 5 mM PHDA in methanol solution was used to assemble PHDA SAMs for 12 h followed by rinsing with methanol. The substrates were then annealed at 150 °C for 48 h under vacuumed. The carboxylic acid terminal groups of the PHDA SAM was activated with 50 mM EDC and 50 mM NHS in an aqueous solution for 2 h followed by rinsing with Milli-Q water and ethyl acetate. Carboxyl activated ITO surfaces were incubated in acetonitrile containing various ratios of 10 mM 1-aminohexa(ethylene oxide) to 1-

aminohexa(ethylene oxide) monomethyl ether. The modified surfaces were rinsed with ethyl acetate several times and dried under a stream of nitrogen. The hydroxyl-terminated hexa(ethylene oxide) molecules were activated with a 0.1 M solution of dry acetonitrile containing DSC and DMAP for 12 h. The activated surfaces were then washed with a copious amount of ethyl acetate and dried under a stream of N2. The samples were then immersed in 20 mM phosphate buffer containing 15 μg/mL of Alexa Fluor 647-tagged GRGDS for 30 min at room temperature. The modified ITO surfaces were washed with Milli-Q water and PBS and were used the same day to seed the HeLa cells on. Before culturing cells on the samples, they were washed using 70 % ethanol followed by PBS under safety cabinet.

2.3.5 Preparation of ITO surfaces modified with fibronectin

900 μl Milli-Q water was added to the Eppendorf containing 100 μl fibronectin (1 mg/ml) solution. The minimum possible of diluted fibronectin was applied to the surface followed by incubation at 37°C for 30 min. The excess fibronectin was removed and rinse three times with water. It is worth noting that the sonication in K_2CO_3 or using an oxygen plasma cleaner should be avoided as they cause the surface to become hydrophilic and non-adherent to fibronectin.

2.4 *IN VITRO* STUDIES

2.4.1 Cell culture

HeLa cells were grown to confluence in DMEM culture media supplemented with 10% fetal bovine serum, 0.1% glutamine at 37 °C in a humidified atmosphere with 5% CO2. Every 3−4 days, the cells were detached from the culture flask using trypsin and washed with PBS containing 0.9% sodium chloride and then were resuspended in fresh media.

2.4.2 Plating cells on ITO modified substrates

When the cells reached 80% confluence, they were removed from the flask with 0.25% trypsin, and were counted using TC20™ automated cell counter, and the appropriate amount of cells were separated for plating on different surfaces.

2.4.3 Primary cell culture and plating

Cells were subsequently grown in T75 flasks in a humidified incubator (Heraeus, Germany) containing 5 % CO_2 at 37 °C, and maintained in DMEM/glutamax media containing 10 % FBS and penicillin/streptomycin (1% v/v). The cell culture medium was changed every 2 days, and all experiments were conducted on cells between passages 3 to 5.

2.4.4 Fixed cells staining with Hoechst 33342 and Alexa fluor® 488 phalloidin

The cell-covered surfaces were washed three times with PBS. To fix the cells, 1 ml of 4% (v/v) paraformaldehyde (PFA) in PBS was placed on the substrate. The container was covered with aluminium foil and was put in the incubator for 15

minutes followed by rinsing three times with PBS. For washing, enough amount of solution was transferred to the well-plate using a pipette, the well-plate was shaken gently including shaking for 5 min in PBS for the last washing, and the solution was transferred into a waste bottle. Cells were permeabilized for phalloidin staining by putting 0.1% Triton × 100 in PBS on the surface for 5 minutes at room temperature. Then, the substrate was washed three times with PBS. To reduce nonspecific background staining with these conjugates, samples were incubated with 1 mg/ml BSA in PBS for 1h at room temperature.

For Phalloidin staining, Alexa fluor® 488 phalloidin (excitation/emission: 495/518 nm, green) or Alexa Fluor® 647 phalloidin (excitation/emission: 650/668 nm, red) were used. A solution of dye conjugated phalloidin solution in PBS (1:200) was prepared and placed on the substrate followed by incubation for 20 minutes, while it was covered with aluminium foil. To visualize nuclei, Hoechst staining (33342, Trihydrate - 10 mg⁄mL Solution in Water from life technology) (excitation/emission 350/461 nm, blue) was carried out next. A solution of 1:1000 Hoechst (10 mg/ml) 33342 solution in PBS (1µg/ml) was made up and added to the well-plate followed by incubation for another 5 minutes while the plate was covered with foil. The substrate was washed three times with PBS.

For storing, the fixed cell-covered substrates can be either submerged in PBS (with Ca^{2+} and Mg^{2+}) at 4 °C or be mounted onto glass slides using mounting media (mowiol gel) that contains an anti-bleaching agent. The later one is suitable for long term storage.

2.4.5 Live cells staining with fura-2 AM

Fura-2/acetoxy-methyl ester (fura-2 AM) was selected to stain the plated HeLa cells on modified ITO surfaces for live cell calcium signalling measurement. The chemical structure and excitation spectra of fura-2 AM are shown in Schematic 2-2.

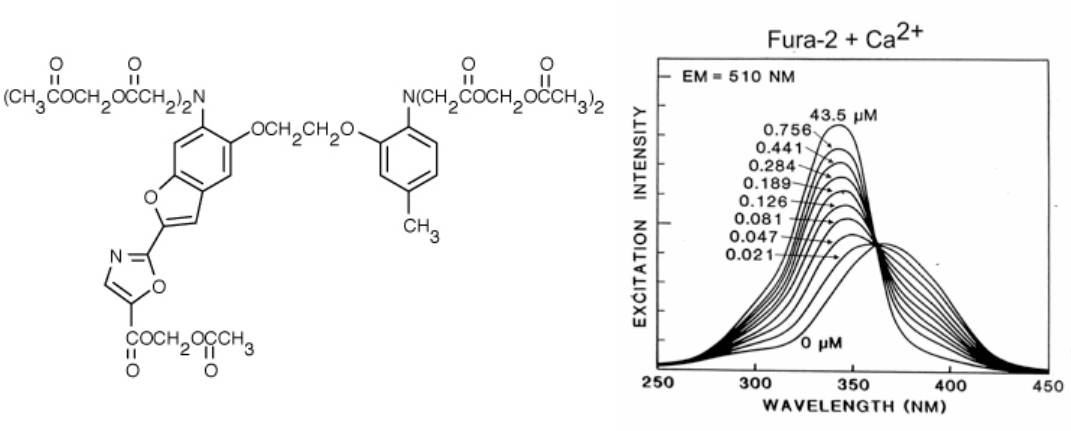

Schematic 2-2. (Left) The chemical structure of fura-2 AM, and (right) The excitation spectra for 1 µM Fura-2 at 20 °C in buffers with free Ca^{2+} values ranging from <1 nM to >10 µM [11].

The loading was performed using the protocol developed in the Herman group [195]. The temperature and incubation time were optimized for the conditions of the current study as will be discussed in chapter 5. Finally, as the optimum condition, cells were incubated in phenol red-free DMEM containing 10% FBS, 2 µM fura-2 AM and 1µl of 10% w/v pluronic F-127 in DMSO for 45 min at room temperature. Cells were washed twice with the imaging buffer made of Hanks' balanced salt solution plus 0.8 mM $MgCl_2$, 1.6 mM $CaCl_2$ and 5% FBS.

2.4.6 Immunocytochemistry for collagen visualization

The cell-covered electrodes were washed with PBS and were blocked with 3% bovine serum albumin (BSA) in Fluorobrite for 10 min. After that, the primary antibody solution was added. This solution was prepared by diluting the primary collagen 1 mouse monoclonal IgG1 antibodies in blocking solution (1:1000 v/v). The cell-covered surfaces were then placed in a cell culture incubator for 90 min and then were washed two times in Fluorobrite (5 min per wash). After that, the cells were fixed in 4% paraformaldehyde solution for 10 min at room temperature. The secondary antibody solution was prepared by diluting the secondary goat anti-mouse antibody conjugated to Alexa-fluor 488 in Fluorobrite (1:500 v/v). The solution was incubated with cells at 37°C for 30 min following washing cells in Fluorobrite twice (5 min per wash). To stain the nuclei, Hoechst® staining solution (1:1000 v/v in Fluorobrite) was incubated for 10 min at room temperature with cells. The coverslips were mounted on the slides using Prolong® Gold anti-fade mounting solution (Life Technologies, USA). The mounted slides were stored in a light-proof box at 4°C until imaging for quantifying the amount of collagen per cell or for coherency analysis.

2.4.7 Coherence analysis

The prepared slides with stained collagen fibres and nucleus were imaged using Leica TCS SP2 multiphoton confocal microscope with a Leica confocal software (LCS). Slides were imaged using a 40x oil objective and a 488 nm laser wavelength. Each slide was imaged in at least three separate areas, randomly chosen by the assessor. A z-stack of each region was taken, as determined by the

top and the bottom of the collagen layer. Once the top and bottom of the z-plane were set, images were taken at 0.05 µM intervals and then condensed into a single frame using the maximum projection function. The coherency of collagen fibres was analysed on confocal images using the orientation J plugin of Fiji software [196] and the orientation J package methodology. Briefly, six regions of interest (ROIs) were chosen at random, excluding those areas with deformations or hole [197]. The ROIs were kept as large as possible to examine the orientations of the collagen bundles, as opposed to the local variations within the bundles. The 'measure' feature was then used to determine the coherence of each ROI. The coherency function draws an ellipse that indicates the coherency of the ROI. The coherence formula takes into account the largest eigenvalue (major axis) and the smallest eigenvalue (minor axis). The coherency equal to 0 means that the ellipse has become a circle, with no elongation and no aligned structures present in the position of the image. The coherency value of 1 represents that the ellipse has become a line segment, with very high elongation and oriented structures present in the position of the image.

2.5 CHARACTERISATION TECHNIQUES AND INSTRUMENTATION

2.5.1 Electrochemical measurements

All electrochemical experiments were conducted in a conventional three-electrode system, comprising gold or glassy carbon as the working electrode, a

platinum foil as the auxiliary electrode, and an Ag|AgCl|3.0 M potassium chloride as reference electrode (CH Instrument Inc., Austin, TX, USA).

Cyclic Voltammetry

The cyclic voltammetry data were acquired using a μAutoLab III potentiostat (Metrohm AutoLab B. V. Netherlands).

Faradaic Impedance Spectroscopy

Electrochemical measurements were performed in an aqueous solution of 1 mM ferri/ferrocyanide ($[Fe(CN)_6]^{-3/-4}$) containing 0.1 M potassium chloride. After rinsing the modified samples with copious amount of water, ethanol and methanol and drying under a stream of argon gas, the blocking properties of the grafted layers toward the electrochemical response of ($[Fe(CN)_6]^{-3/-4}$) redox probe were investigated. Solartron SI 1287 electrochemical interface coupled with an SI 1260 frequency response analyser (Solectron Analytical, Hampshire, England) was used for EIS measurements. EIS spectra were recorded in the frequency range of 10^5 to 10^{-1} Hz. An AC potential, with 0.01 V peak to peak amplitude, was superimposed on a DC potential of 0.2 V. Impedance data were recorded using Zplot and Zview 3.1 software (Scribner Associates, Inc.). R_{ct} of each system was obtained by fitting the Nyquist plot with a Randles equivalent circuit. The circuit consists of the R_{ct}, ohmic resistance of the electrolyte, Warburg impedance (resulting from the diffusion of the redox species), and a constant phase element (modelling the double-layer capacitance). A constant phase element was used to compensate for lack of ideal capacitance behaviour of the interface.

Non-Faradaic Impedance Spectroscopy

EC-Lab® V10.33 (BioLogic, Science Instruments) software was used to analyse the impedance data. For impedance measurement and analysis, the interdigitated ITO surfaces were probed with a weak non-invasive AC signal within the range of frequency between 40000-400 Hz (10 mV). The active surface area of the interdigitated ITO area was 1.3×10^{-4} cm^2. The impedance of modified cell-free interdigitated ITO electrodes was measured as baseline data. Then, the real-time impedance read-out of the cell layer before and after histamine addition was monitored. The impedance value has been normalized by dividing the impedance of cell-covered electrode to the baseline impedance.

2.5.2 X-ray photoelectron spectroscopy (XPS) measurement

XPS analyses were conducted using an Escalab220-IXL spectrometer equipped with a monochromatic Al Ka source (1486.6 eV), a hemispherical analyser, and a multichannel detector. The spectra were accumulated at a nominal photoelectron take-off angle of 58º with a 0.79 mm^2 spot size at a pressure of less than 10^{-8} mbar. Wide surveys were obtained at a pass energy of 100 eV with 1.0 eV step sizes and a minimum of 25 scans. Narrow survey scans (N 1s, P 2p, S 2p, O 2p and C 1s) were conducted with 0.1 eV step size, 100 ms dwell time, and 20 eV pass energy. The experimental energy shifts were corrected with reference to C1s at 284.8 eV. XPSPEAK 4.1 data analysis software was used to calculate the elemental compositions from peak areas. Percentage coverage for the different elements and sub-groups were estimated from the related fitted area and attributed sensitivity factors.

2.5.3 Optical Microscopies

Phase Contrast and Epifluorescence Microscopy

The sequences of fluorescence and phase contrast images were acquired on a Zeiss Axio Observer X.1 Spinning Disk/TIRF inverted microscope with Zeiss ZEN software. The microscope was equipped with the lambda DG4 light source switcher and a scientific complementary metal-oxide semiconductor (sCMOS) camera (Orca Flash 4). The wavelength switcher allows shifting between two wavelengths in less than 1.2 ms useful for fura-2 ratiometric measurements. Depends on the experiment, different objective of 10×, 20× or 40× have been used. For ratiometric imaging, the exposure time was set to 50 ms.

A Leica DMIL inverted fluorescence microscope (Leica Microsystems Pty Ltd, USA), equipped with transmitted light LED back illumination and EL6000 Fluoro system (mercury lamp) was employed to investigate cells density and spreading with a relatively good resolution at 10× or 20× magnifications. At least three samples were prepared for each experiment, and five adjacent fields were counted for each sample under 250 ms exposure time. The obtained images were processed using ImageJ analysis software with appropriate plugins for distance, area, and cell counting analysis

2.5.4 NMR Spectroscopy

^{1}H NMR spectra were recorded using a Bruker ACF300 (300 MHz) spectrometer, employing MeOD as the solvent.

2.6 STATISTICAL ANALYSIS

Data are displayed as means ± SD unless otherwise stated. Data were analysed using the GraphPad Prism version 6.0 data management software to conduct ANOVA on groups of data. Statistically, significant differences between each treatment were determined using Bonferroni post hoc tests.

CHAPTER 3 FORMATION OF STABLE AND LOW IMPEDANCE ANTI-FOULING COATINGS

3.1 INTRODUCTION

One of the essential components of cell-based assays is the substrates to accommodate cells. One of the required features of these surfaces, especially in electrochemical cell-based assays, is the ability to resist nonspecific adsorption of proteins [198]. Antifouling surfaces are also important in applications such as tissue engineering [199], carriers for targeted drug delivery [200], and implantable biomedical devices such as catheters and contact lenses [201, 202]. Nonspecific protein adsorption on an electrode may lead to a decrease in sensor selectivity by interfering with the interaction of target species with the sensing surface, or may result in fluctuations in sensor sensitivity by blocking the electron transfer pathway of redox active species [198]. Furthermore, for implantable electrodes, the initiation of protein adsorption often provokes the immune and coagulation systems [203, 204]. Hence the antifouling capability of an electrode is crucial for electrodes used in biological fluids [201, 202, 205].

Poly(ethylene glycol) (PEG) [201] and oligo(ethylene glycol) (OEG)-alkanethiol self-assembled monolayers (SAMs) [206] in limiting protein adsorption has led to their wide application in biosensing. In attempts to obviate the potential high impedance problem of these molecules [207, 208], the interest has been drawn to develop low impedance antifouling layers comprising zwitterionic molecules [75].

The use of zwitterions as antifouling materials traces back to the use of phosphorylcholine (PC) zwitterionic molecules to improve antithrombogenic

property of biomaterials [209, 210]. Since then the use of similar molecules for surface modification has become progressively more common [211]. Although zwitterions are expected to be highly protein resistant, experimental and molecular studies of the antifouling property of phosphorylcholine molecules on gold surfaces [210, 212-214] show that the charge balance, dipole-dipole interaction and packing density are important parameters determining protein resistance ability of zwitterions. Therefore, apart from the chemical structure, different synthetic and coating methods have been stated to be considered in the fabrication of zwitterions-bearing coatings [214-216]. Incorporating phosphorylcholine zwitterions into alkanethiols to form phosphorylcholine-terminated zwitterionic SAMs was initiated by both the Whiteside and Cooper groups [208, 211]. SAMs with zwitterionic head groups anchored by short chains of alkanethiols face poor stability problem due to oxidation of the gold-thiolate bond in most physiological solutions which results in loss of the layer from the surface [217, 218]. On the other hand, the use of long chain alkanethiols is not desirable because of their high impedance property, which limits the Faradaic electrochemistry to proceed at the underlying electrode. As an alternative to alkanethiols is to use aryl diazonium salts derived layers on gold electrode surfaces because of their greater stability [219, 220]. Aryl diazonium salts derived layers to anchor antifouling moieties have just started to be explored [221, 222]. Recently, the Gooding group has shown the utility of modification of GC electrode surface in resisting protein adsorption using different low impedance aryl diazonium salts bearing zwitterion molecule [75]. It has been

shown that aryl diazonium salt derivatives can form stable layers, with efficient electron transfer kinetics on different surfaces [219, 223-227]. Details on surface modification using aryl diazonium salts and their properties have been extensively reviewed [220, 223, 228, 229].

The purpose of this chapter is to create low impedance antifouling coatings on gold surface for electrochemical bioassay applications. In this regard, three new PPC bearing gold surfaces were constructed, one is PPC diazonium salt reductively adsorbed onto gold (Au/PPC) (Schematic 3-1, surface 1) and the other two are PPC self-assembled onto gold, i.e., dithiocarbamate PPC (Au/dithiocarbamate PPC) (Scheme 3.1, surface 2) and lipoic acid coupled PPC (Au/lipoamide PPC) (Schematic 3-1, surface 3) to give monolayers. The protein resistance ability of these interfaces were compared to those of 1-dodecanethiol SAM-coated on gold (Au/C12) (Schematic 3-1, surface 4),O-(2-mercaptoethyl)-O'-methyl-hexa(ethylene glycol) SAM grafted gold (Au/OEG) electrodes(Schematic 3-1, surface 5) and PPC diazonium salt reductively adsorbed on GC surface (GC/PPC) (Schematic 3-1, surface 6). Electrochemical impedance spectroscopy (EIS) was used to measure charge transfer resistance (R_{ct}) of the modified surfaces before and after exposure to bovine serum albumin (BSA) solution in phosphate buffered saline (PBS) detecting the protein resistant ability of the surfaces. Furthermore, visualizing and quantification of protein adsorption were conducted using fluorescence microscope imaging.

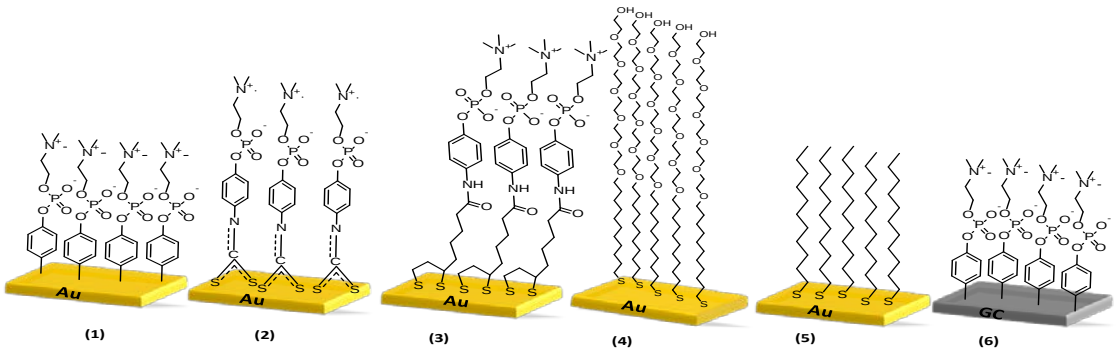

Schematic 3-1. Illustration of gold surfaces modified with (1) PPC; (2) dithiocarbamate PPC SAM; (3) lipoamide PPC SAM; (4) (11-mercaptoundecyl) hexa(ethylene glycol) SAM and; (5) 1-dodecanethiol SAM and (6) glassy carbon electrode modified with PPC diazonium salts. Interfacial impedance and antifouling nature of the newly developed (1), (2), and (3) surfaces were investigated and were compared with the conventional (4) antifouling surface, (5) fouled surface and (6) a previously developed antifouling surface with low impedance from the Gooding group in ref. [17].

3.2 EXPERIMENTAL METHODS

3.2.1 Electrochemical Measurement

The electrochemical cyclic voltammetry (CV) and electrochemical impedance spectroscopy (EIS) were performed to modify or characterise the surfaces as has been explained in Chapter 2, § 2.5.1.

3.2.2 Preparation of Solution of Dithiocarbamate PPC

Dithiocarbamate phenyl phosphorylcholine solution was prepared as has been explained in Chapter 2, § 2.2.1.

3.2.3 Synthesis of Lipoamide PPC molecules

The synthesis route of PPC-lipoamide molecule and its characterisation using thin layer chromatography and 1H NMR (MeOD, 300.2 MHz) are described in Chapter 2, § 2.2.2.

3.2.4 Preparation of Phenyl Phosphoryl Choline-based Layers on Gold

The PPC molecules were immobilized on gold surfaces using electrochemical reduction of 4-aminophenyl phosphorylcholine diazonium salt on the surface described in Chapter 2, § 2.3.2.

The modification of glassy carbon with PPC involve the electrochemical reduction of 4-aminophenyl phosphorylcholine diazonium salts [75]. This process was similar to that for Au/PPC, but the potential range from 0.6 to −0.8 V was used during the electrochemical adsorption process. Figure 3-1 illustrates the process of in-situ generation of PPC diazonium salt and modifying gold and glassy carbon surfaces.

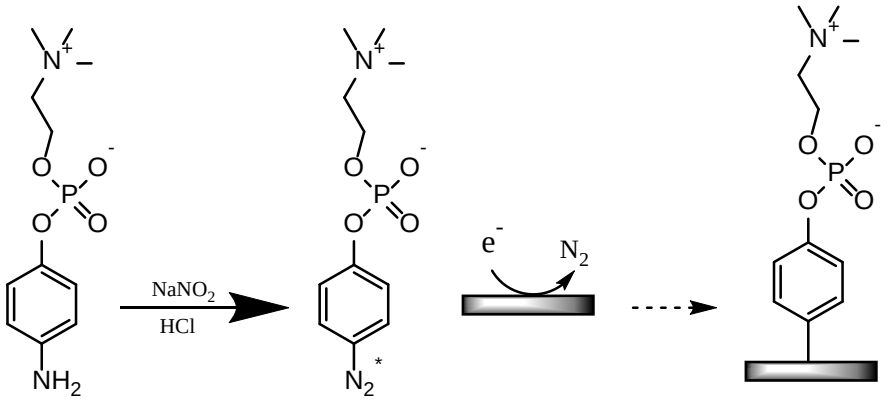

Figure 3-1. The processes of in situ generation of PPC diazonium salt and coupling to gold or glassy carbon surface. The aromatic amine is converted to the diazonium salt and then binds to the carbon surface with loss of nitrogen.

3.2.5 XPS Measurement

The instrumental setup and data processing of XPS are detailed in Chapter 2, §2.5.2.

3.2.6 Protein Adsorption and Fluorescence Microscope Imaging

The modified samples and the control samples were soaked in 1 mg/ml FITC labelled BSA solution in PBS (pH 7.4) for 0.5 h at 4 ºC. The containers were wrapped in aluminum foil to protect FITC fluorophores from light. To be able to read the background fluorescence, necessary for fluorescence intensity analyses, samples were placed in plain PBS solution. After removing the solutions, the samples were washed with PBS three times followed by rinsing with Milli-Q water. Fluorescence microscopic images were captured as described in Chapter 2, § 3.3.4.

3.3 RESULTS AND DISCUSSION

3.3.1 Electrochemistry of reductive adsorption of in situ generated PPC diazonium salt on gold and glassy carbon electrodes

The cyclic voltammograms of the reduction deposition of *in situ* generated PPC on gold and glassy carbon electrodes are shown in Figure 3-2. On gold surfaces, the first reduction peak was observable at around −0.03 V in the first cathodic scan. From the second scan onward, the reduction peak was dramatically attenuated. The attenuation is an indicator of increasingly bounded phenyl groups to the surface. The formed layer of PPC serves as an insulating organic layer, which limits further reduction of the reduction deposition the aryl diazonium salt onto the surface. On glassy carbon, unlike on gold, the reduction peak of *in situ* generated PPC was not clearly observable. However, although there was no

distinct reduction peak observed in the case of glassy carbon, the dramatic decrease of cathodic current between +0.15 to -0.75 V in the second scan indicated the formation of phenyl layers on the electrode surface[75]. The potential at which the reductive adsorption occurs was more positive on gold compared with on glassy carbon electrode. This observation is consistent with the previous works by the Gooding group, where carboxyphenyl [227], 4-sulfo phenyl [225] and 4-nitrophenyl [224] diazonium salts were electrochemically bonded to gold and glassy carbon electrode surfaces. The presence of the reduction peak even after the 5th cycle, on both gold and glassy carbon surfaces, is tentatively suggesting that the surfaces have not been completely passivated by PPC molecules.

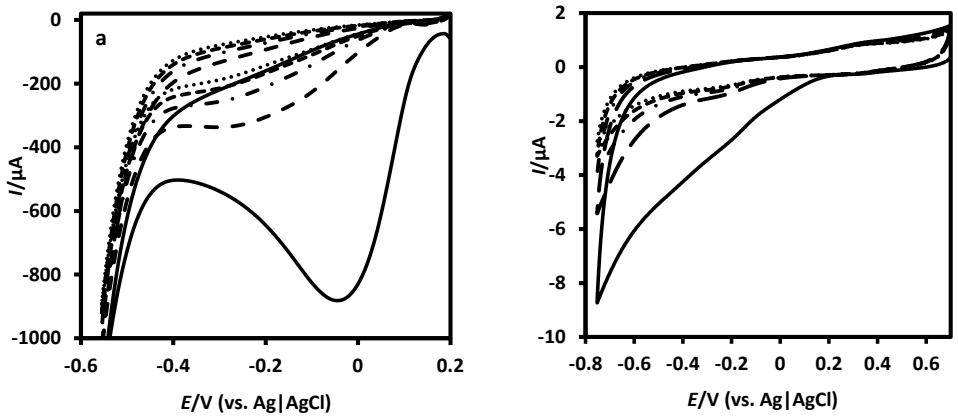

Figure 3-2. Cyclic voltammogram of the reductive adsorption of in situ generated PPC diazonium salt in an aqueous solution containing 5 mM PPC, 5 mM $NaNO_2$ and 0.5 M HCl, at 0.1 V s-1 on (a) gold electrode and (b) glassy carbon electrodes. Each scan is represented by solid line (1st scan), large dash curve (2nd scan), dash-dot curves (3rd scan), small dash curve (4th scan), and dotted curve (5th scan). The suppression of the electrochemistry after the first scan being indicative of passivation of electrode surfaces by grafted PPC molecules.

3.3.2 Characterisation of Lipoamide PPC molecules

The retention value (R_f) for the product was 0.44 using the mixed eluent of water, ethanol, and chloroform (0.5:2:1.3). The product was visualized as dark spots under UV, and as blue spots after dipping the silica plate into AMCS solution, which contains ammonium molybdate, cerium sulphate and sulfuric acid (10%). The final white compound was characterized using 1H NMR (MeOD, 300.2 MHz) (Figure 3-3): δ 1.15-1.35 4H, 1.42-1.95 5H, 2.33-2.55 5H, 3.18 9H, 3.62 2H, 4.34 2H, 7.18 2H, 7.49 2H and 31P NMR (HZ) δ -7. The solution of the synthesized lipoamide molecules in methanol was used to prepare gold modified surfaces with lipoamide PPC layer (Au/lipoamide PPC).

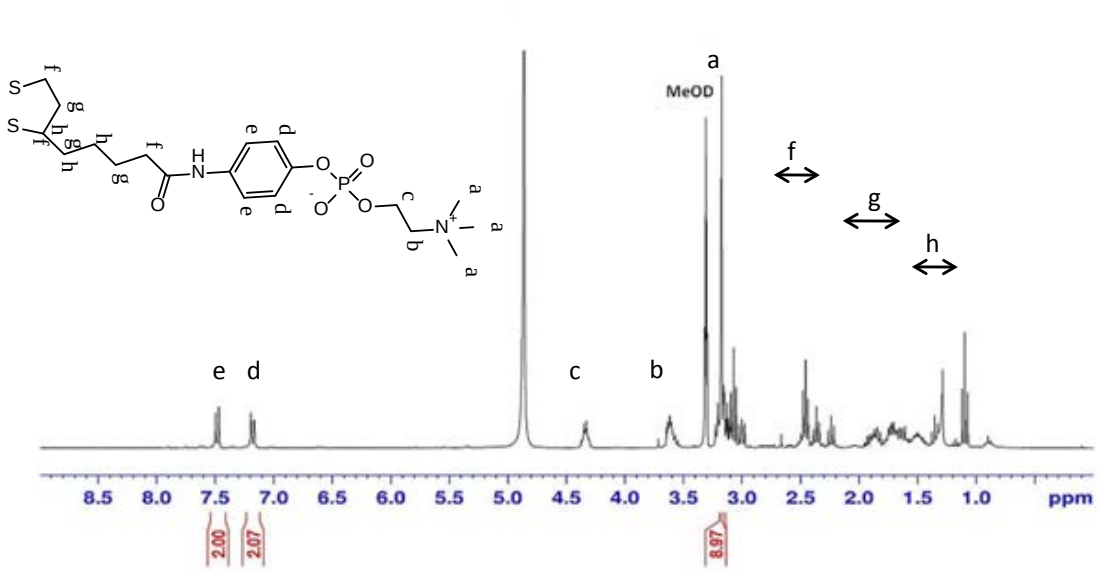

Figure 3-3. The 1H -NMR spectrum of the synthesized lipoamide PPC molecule. The structure of the molecule and the related important peaks have been illustrated. The formation of lipoamide PPC molecules was verified by 1H NMR spectroscopy.

3.3.3 XPS Characterization of Gold and Glassy Carbon Modified Surfaces

The core level XPS spectra for carbon, nitrogen, oxygen and thiol of the three new interfaces (i.e., Au/PPC, Au/dithiocarbamate PPC, and Au/lipoamide PPC) are shown in Figure 3-4. The C 1s high-resolution spectra were fitted with several peaks with a main peak centred at about 284.5 eV, which corresponds to the C-C binding energy. The fitted peaks at around 286.5 eV in C 1s regions are characteristic of the carbon atoms bound to nitrogen and oxygen. The emergence of new peaks at 288.7 and 289.0 eV in the C 1s core level spectra of Au/dithiocarbamate PPC revealed the formation of S-C-N and S-C-S bonds, respectively. A peak at the binding energy related to carbonyl group, which is 287.5-288.1 eV [230], was observed in the C 1s core level region of Au/lipoamide PPC. In the N 1s narrow scans of the three interfaces, the spectra were fitted with two peaks centred at ~400 eV and ~402 eV. The nitrogen peak at around 402 eV is indicative of the presence of the ammonium nitrogen of phosphorylcholine group. The peaks at ~400 eV in the N 1s core level region of Au/PPC substrate (indicated with N* in Figure 3-4) is often attributed to formation of very small proportions of azo groups (CN=NC), as has been discussed in the literature as a consequence of deposition of aryl diazonium salts on surfaces [231, 232]. However, a very low intense nitrogen peak at ~400 eV for the bare GC surface was observed [75]. Peaks at around this binding energy in the cases of Au/dithiocarbamate PPC and Au/lipoamide PPC (indicated by N** in Figure 3-4) are attributed to the nitrogen atom attached to carbon disulphide and the nitrogen atom of the amide bond in their structures, respectively.

Figure 3-4 also shows the S 2p narrow spectra of Au/dithiocarbamate PPC and Au/lipoamide PPC. The S 2p core level regions show a main peak centred at 161.01 eV for Au/dithiocarbamate PPC and 162.37 eV for Au/lipoamide PPC assigned to the S $2p_{3/2}$ sulphur species. S $2p_{3/2}$ peak corresponds to the chemisorbed organosulphur compounds on Au [233]. The lower value of S 2p3/2 binding energy for Au/dithiocarbamate PPC surface shows that the dithiocarbamate sulphur atoms carry more negative charge (shifted from the nitrogen atom and phenyl group to the CS_2 moiety) than thiolates bound to Au [234]. The presence of phosphorylcholine groups on all PPC-based modified surfaces was confirmed by the appearance of phosphorous peak at ~133 eV (EP2p), nitrogen peak at ~402 eV (EN1s), and oxygen peak at 530-531 eV (EO1s (O1)) (Table 3-1 and Figure 3-5). Table 3-1 also shows the S/Au ratios for Au/dithiocarbamate PPC and Au/lipoamide PPC while the values of S and Au were calculated from the respected percentage coverage of S 2p3/2 and Au peaks from XPS, respectively. The S/Au value is an indicator of sulphur atoms bound to the substrate [233]. This value for Au/lipoamide PPC is about twice as large as that for Au/dithiocarbamate PPC for surfaces modified in a similar manner

(i.e., same incubation time in the equally concentrated modifying solution).

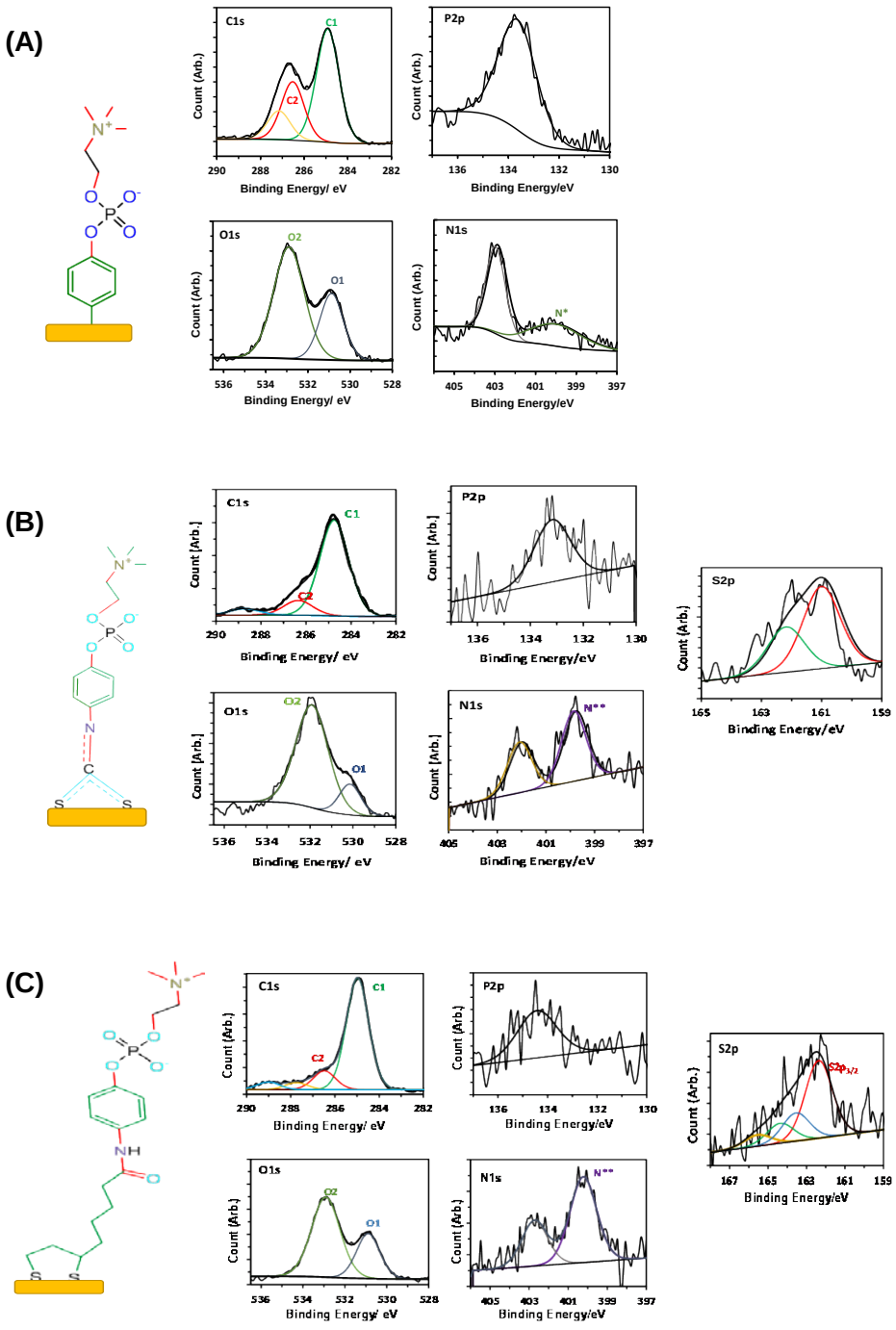

Figure 3-4. XPS spectra of Au/PPC, Au/dithiocarbamate PPC, and Au/lipoamide PPC surfaces in C1s and N 1s core level regions. The nitrogen peak at 402.97 eV is assigned to nitrogen of phosphorylcholine group. Peaks at 288.7 and 289.02 eV in the C1s core level spectra of Au/dithiocarbamate PPC and Au/lipoamide PPC confirm the formation of S-C-N and S-C-S bonds.S 2p3/2 binding energy corresponds to the chemisorbed

organosulphur compounds on Au, which is lower for Au/dithiocarbamate PPC surface indicating that dithiocarbamate S atoms carry more negative charges.

The conclusion on the degree of coverage (or surface density) was confirmed by obtaining the estimated values of fractional molecular coverage for Au/dithiocarbamate PPC and Au/lipoamide PPC based on the adlayer approximation model introduced by Fadley. In Fadley modified model, ratios of adsorbate species to surface atoms on Au(111) plane (N_{ML}/N_{Au}) from XPS results is estimated as an indicator of the fractional coverage of monolayer (ML) of formed SAMs [194, 235]. This method relies on the measured value of adlayer-to-substrate intensity ratios and assumes a non-attenuating adlayer. In this regard, the Au/lipoamide PPC and Au/dithiocarbamate PPC are ideal as the formed SAMs allow the S 2p and Au 4f signal intensities to be collected without minimal extinction. The model accounts for experimental factors such as XPS sampling geometries and elemental sensitivities. The polycrystalline Au surface was approximated as Au(111) facet in order to relate the observations to the structural data available for alkanethiols on defined gold surfaces[236]. Using this model, the fractional coverage of monolayer for Au/lipoamide PPC and Au/dithiocarbamate PPC were calculated of 0.21 and 0.12 ML, respectively, by taking account of the two sulphurs that each lipoamide PPC and dithiocarbamate PPC molecules possess. The fractional coverage of monolayer of close-packed alkanethiol SAMs for a $(\sqrt{3} \times \sqrt{3})$ *R*30° superlattice on Au(111) is assumed to be 0.33 ML [234].

The ratio of percentage coverage of the ammonium nitrogens peak centred at ~402 eV in the N 1s core region and phosphorous peak centred at ~133 eV in P 1p core region can also provide information on the quality of these layers (N/P values in Table). Jiang and co-workers [214] have used the N/P value as an indicator of the charge balance of phosphorylcholine-zwitterionic surfaces, and have concluded that the closer this value is to the theoretical value of 1:1, the higher the quality of the phosphorylcholine SAMs have formed. The N/P ratios were 0.94 for GC/PPC, 0.67 for Au/PPC, 0.77 for Au/dithiocarbamate PPC and 0.99 for Au/lipoamide PPC. Based on these N/P values, one would conclude the Au/lipoamide PPC and the GC/PPC are closest to charge neutral.

XPS can also be used to estimate the thickness of the formed layers of PPC diazonium salts on gold surfaces in the case of Au/PPC. The attenuation of the substrate signal scales from XPS results was used to estimate the approximate thickness of the grafted layer using Equation 1 [237].

$$d_{ML}/\lambda_{Au,ML}\,(1/\cos\theta) = -\ln(\text{Au 4f}_{ML}/\text{Au 4f}_{clean}) \qquad \text{(Equation 3.1)}$$

where Au $4f_{ML}$ is the integrated area of the Au $4f_{7/2}$ peak, Au $4f_{clean}$ is the Au $4f_{7/2}$ peak area of an unmodified and clean Au substrate, d_{ML} is the thickness of the grafted organic layer, $\lambda_{Au,ML}$ is the mean free path of Au $4f_{7/2}$ electrons travelling across the organic film, and θ is the photoelectron take-off angle with respect to the surface normal. The estimate of PPC layers thickness for Au/PPC is ca. 7 nm, when the mean free path of Au $4f_{7/2}$ electrons travelling across the organic film is

assumed as 4.2 nm. This value in compare to the estimated molecular length, which was calculated as 0.8 nm using semi empirical Mopac calculations in Chem3D Ultra, indicates the formation of multilayers on the surface in the case of Au/PPC as has been commonly observed for aryl diazonium salt derived layers [223]. Note the evidence for multilayers of PPC on gold is despite the cyclic voltammetry showing that there is very little suppression of ferricyanide electrochemistry. The good accessibility of ferricyanide to the underlying gold electrode suggests that despite there being multilayers, the layers are still open and porous to species in solution.

Table 3-1. Elemental ratio, determined by comparison of the normalised peak area from XPS of different modified surface. The ratio of S/Au indicates the packing density of compounds on the surface, and N/P ratio value is an indicator of charge balance of phosphorylcholine zwitterions anchored on the surface. The represented E_{P2p}, E_{N1s} and $E_{O1s\ (O1)}$ are assigned to the presence of phosphorylcholine groups.

Surfaces/ modifying layer	Elemental ratio		$E_{S2p3/2}$(eV)	E_{P2p} (eV)	E_{N1s} (eV)	$E_{O1s\ (O1)}$ (eV)
	N/P	S/Au				
GC/PPC	0.94:1	------	-------	134.09	403.26	531.03
Au/PPC	0.67:1	------	-------	133.63	402.97	530.88
Au/dithiocarbamate PPC	0.77:1	0.044	161.01	133.17	402.09	530.14
Au/lipoamide PPC	0.99:1	0.090	162.37	134.03	402.72	530.89

Furthermore, to confirm the successful preparation of GC/PPC, the XPS analysis was also performed for GC/PPC substrate. The P 2p, N 1s, C 1s and O 1s narrow scans from XPS measurement of the glassy carbon surface modified with PPC diazonium salt (GC/PPC) are shown in Figure 3-4. The phosphorous peak centred at 134.09 eV and the fitted nitrogen peak at 403.2 eV, in addition to the fitted

oxygen peak centred at 531.23 eV are indicative of presentation of phosphorylcholine groups. In addition to the fitted peak centred at 403.2 eV, the N1s core level region also contains another fitted peak at around 400 eV. This less pronounced fitted peak could be from azo linkage of multilayer formation, and also has been observed on bare glassy carbon [75]. The C1s core level region was fitted with three peaks. The fitted peak with the maximum intensity centred at 284.96 eV is attributed to C-C bonds of the phenyl groups and the other two fitted peaks centred at about 286 and 287 eV are assigned to the remaining carbon in PPC structure and carbon atoms on the surface, respectively. The oxygen peak at around 532 eV comes from water residuals and carbon oxygen species on the surface. Figure 3-5 contains the P2p and O1s core level regions from XPS analyses of gold modified with PPC diazonium salt (Au/PPC), Au/dithiocarbamate PPC, and Au/lipoamide PPC. The phosphorous peak at about 133 eV and oxygen fitted peak centred at about 531 eV (O1) are attributed to the formation of phosphorylcholine groups.

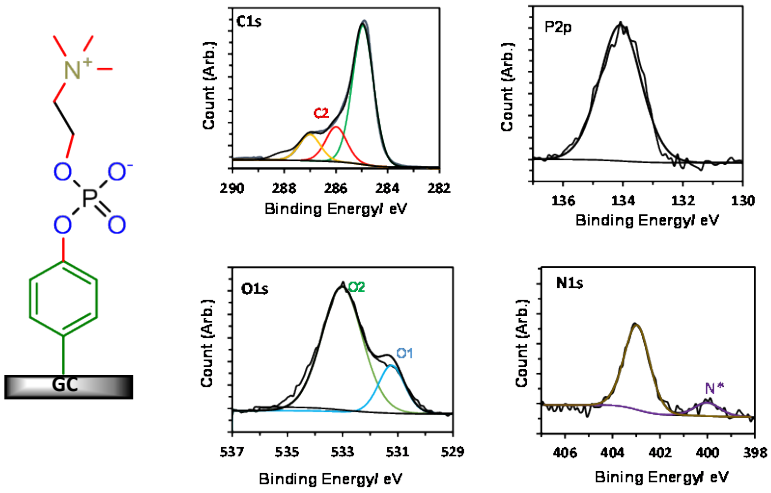

Figure 3-5. XPS spectra of Au/PPC, Au/dithiocarbamate PPC, and Au/lipoamide PPC surfaces in C1s and N 1s core level regions. The nitrogen peak at 402.97 eV is assigned to nitrogen of phosphorylcholine group. Peaks at 288.7 and 289.02 eV in the C1s core level spectra of Au/dithiocarbamate PPC and Au/lipoamide.

3.3.4 Fluorescence Microscopy Studies to Evaluate Protein Adsorption

The ability of the modified surfaces to repel proteins from the surface was examined by visualizing the FITC-BSA adsorbed on the surface using fluorescence microscopy. BSA is a globular serum protein which is frequently used in protein adsorption studies [222]. The normalised mean grey value providing a quantitative comparison of the relative amount of BSA adsorption on the 6 differently functionalised surfaces is shown in Figure 3-6. In this figure, the top fluorescence images are examples of the images used in the quantitative comparison. The values in this diagram are not the absolute quantity of the adsorbed protein, but still are relative indicators of the antifouling properties of each surface compared to the Au/C12 and Au/OEG, which are known as standard fouling and commercial antifouling substrates, respectively. This comparison

becomes more worthwhile as the functionalised gold surfaces are compared with GC/PPC surface regarding their antifouling property. The success of PPC on GC at resisting protein adsorption has been shown, previously [75]. By comparing the adsorption of BSA on various surfaces in the bar chart of Figure 3-6, it can be readily seen that the protein adsorption of the Au/PPC surface is around 116% relative to the conventional fouling Au/C12 being set at 100%. The Au/dithiocarbamate PPC surface has 88% of the adsorption on Au/C12 while modifying the gold surface using lipoamide PPC molecules, which has a higher density of molecules on the surface elicits a more notable decrease in BSA adsorption. Au/lipoamide PPC surface has less than 22% of the level of adsorption on Au/C12 interface. Comparing the level of BSA adsorption on Au/lipoamide PPC with Au/OEG shows that this interface is almost as resistant as Au/OEG to BSA adsorption. The level of nonspecific adsorption is even lower on the GC/PPC surface, being less than 6% of the Au/C12. It is notable that the low level of BSA adsorption on GC/PPC and Au/lipoamide PPC are also the surfaces that had N/P ratios of close to 1. Comparing the shown protein adsorption of GC/PPC and Au/PPC reveals that Au/PPC is much less effective at repelling BSA from the surface despite the molecule, the modification condition and analysis method being the same.

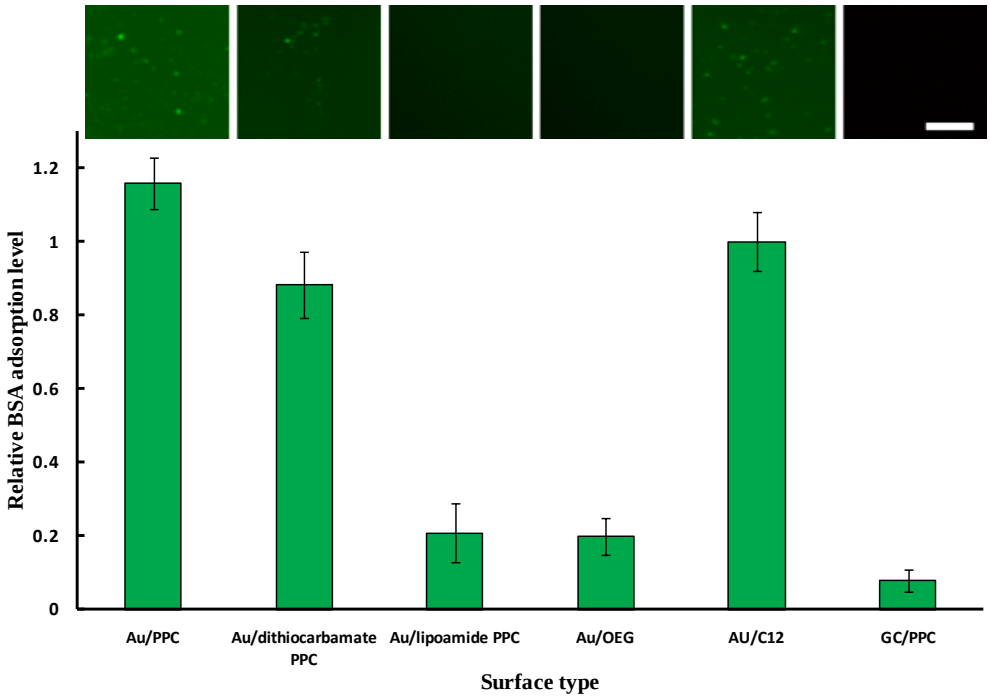

Figure 3-6. The relative level of FITC-BSA adsorption on the different modified surfaces. The average intensity of background has been subtracted prior to normalisation to C12-SAM modified gold surface. Top fluorescence microscopic images are for the FITC labelled BSA adsorbed on the modified electrodes recorded under 10x magnification.

3.3.5 EIS for Evaluation of Nonspecific Adsorption

As the motivation for evaluating the different surface modification layers was for electrochemical applications, it was important that the layers be both effective at limiting nonspecific adsorption and have low impedance. Therefore EIS was measured before and after exposure to BSA. Comparison of the R_{ct} values of the modified surfaces before (R_{ct1}) and after exposure to BSA solution R_{ct2}) is an indicator of their antifouling property. Protein adsorbed onto a surface will decrease the accessibility of the redox species in solution to the surface, hence increasing the R_{ct} value. Examples of the Nyquist plots that have been used to obtain the R_{ct} values reported in Table 3-2 can be found in Figure 3-7. The almost

unchanged value of R_{ct} of GC/PPC and Au/lipoamide PPC surface in BSA-rich solutions highlights the protein resistance properties of these surfaces. The antifouling property of Au/lipoamide PPC and GC/PPC is similar to the exhibited antifouling nature of Au/OEG, as R_{ct} value before and after BSA adsorption for both the cases remains almost the same. The R_{ct2}/R_{ct1} value for Au/dithiocarbamate PPC is 1.7, which is close to this value for fouling Au/C12. Consistent with the obtained high-intensity fluorescence images of Au/PPC after exposure to FITC-BSA, the magnitude of R_{ct} of $[Fe(CN)_6]^{-3/-4}$ showed a significant change of 4.6 times higher upon the exposure to BSA solution for this surface, emphasizing significant BSA adsorption (Table 3-2).

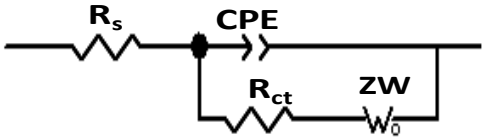

Figure 3-7. A Randles equivalent circuit used to fit the EIS data. The value of Rct is used to compare the passivation effect of modification or adsorbed BSA molecules on surfaces.

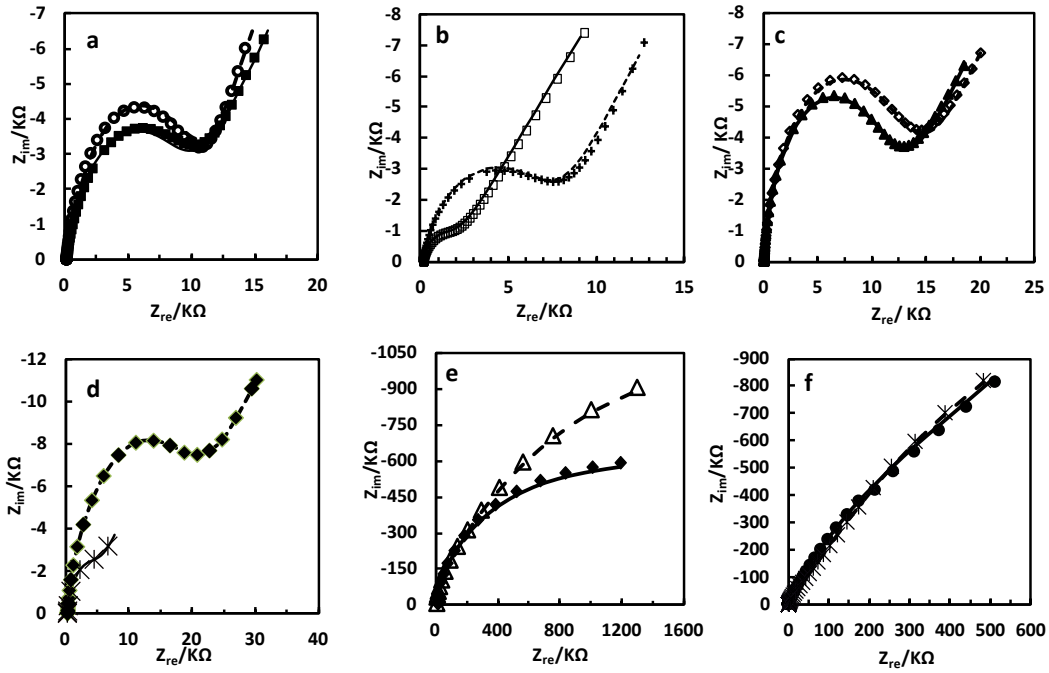

Figure 3-8. Experimental (scattered points) and fitted (lines) Nyquist plot recorded in 1mM ferri/ferrocyanide ($[Fe(CN)_6]^{-3/-4}$) redox at a scan rate of 0.1 V s^{-1} for (a) GC/PPC; (b) Au/PPC; (c) Au/lipoamide PPC; (d) Au/dithiocarbamate PPC ; (e) Au/C12; and (f) Au/OEG. Comparison of Faradaic impedance of the surface before (solid curve) and after (dash-line curve) exposure to 1 mg.ml^{-1} BSA solution for 1 h.

It is worth noting that the R_{ct} values for the modified surfaces are significantly lower for Au/PPC, Au/dithiocarbamate PPC and Au/lipoamide PPC as compared to that measured for Au/OEG, which emphasizes the lower impedance of the newly fabricated gold modified surfaces.

Table 3-2. The charge transfer resistance of different surfaces measured in 1 mM $[Fe(CN)_6]^{-3/-4}$ solution before (R_{ct1}) and after (R_{ct2}) 1 h exposure to 1 mg ml^{-1} BSA. The ratio of R_{ct1}/R_{ct2} is an indicator of the amount of BSA adsorption on surface hindering the electron transfer obtained by dividing the average value of R_{ct1} to R_{ct2}. Average values

and relative standard deviations (RSD) were calculated after carrying out each experiment for 3 samples (n=3).

Modified Surfaces	R_{ct1}/ Ω cm^2	R_{ct2}/ Ω cm^2	R_{ct2}/R_{ct1}
GC/PPC	710.8(RSD=0.07)	728.1(RSD=0.01)	1.0
Au/PPC	83.1 (RSD=0.09)	389.5(RSD=0.07)	4.6
Au/lipoamide PPC	734.7 (RSD=0.11)	844.3 (RSD=0.06)	1.1
Au/dithiocarbamate PPC	480.6 (RSD=0.20)	855.5 (RSD=0.08)	1.7
Au/C12-SAM	56770.1 (RSD=0.02)	90833.1 (RSD=0.005)	1.6
Au/OEG-SAM	17775.3 (RDS=0.04)	19135.7 (RSD=0.03)	1.0

3.4 SUMMARY

Three coatings on gold electrode surfaces that were expected to reduce the nonspecific adsorption of proteins to surfaces but which did not passivate the electrode from undergoing Faradaic electrochemistry were evaluated. The performance of these layers in limiting protein adsorption was compared to OEG and C12 SAMs. The OEG was chosen as a typical antifouling molecule and the C12 SAM as a common fouling substrate. The performance of the layers was also compared to the previously developed dual low impedance/antifouling GC/PPC [75]. Fluorescence microscopy and EIS results together show that the order of

antifouling ability of the coatings on gold was reductively adsorbed PPC diazonium salt <dithiocarbamate PPC SAM <lipoamide PPC SAM. The lipoamide PPC SAM was shown to have similar protein resistance to the ‘gold standard’ of an OEG SAM on gold. The other layers were inferior in their protein resistance to OEG SAMs and GC/PPC layers. The low antifouling property of PPC diazonium salt derived layers, on gold, was related to a lower PPC density, less charge neutral structure of the PPC layers on gold compared with on glassy carbon. Gold surfaces modified by lipoamide PPC short zwitterionic molecules exhibit low impedance property, which is required for electrochemical application as has been discussed above. The results contribute to the engineering of the low impedance/antifouling films on gold surfaces, a substrate widely used in electrochemistry measurements.

Regarding designing the appropriate cell-based tool for studying cell functions as the ultimate goal of this study, it was decided to provide the opportunity of performing both electrochemistry and optical microscopy. It was discussed in Chapter 1, § 1.9.2, impedance measurements as one of the most common electrochemical methods for study cells provide real-time information on slight changes in adhesion of cells to cells/surfaces at the whole-cell level over long-term in a label-free manner. On the other hand, fluorescence microscopy is capable of precise monitoring of short-term specific subcellular processes. Therefore, to provide more comprehensive information on cell responses to different environmental stimuli the study aimed at designing and fabricating a simultaneous optical/electrochemical cell-based assay.

It is challenging to use gold films for optical microscopy applications due to lack of transparency and quenching fluorescence properties, although it is one of the most ideal interfaces for optical imaging. The researches to find the appropriate substrate for the optical/electrical assays resulted in selecting indium-tin oxide (ITO) as the substrate to accommodate cells. ITO is conductive and transparent surface, desirable to fulfil the compatibility with both optical and electrical monitoring techniques. To study the feasibility of using ITO in such a assay; i) the feasibility of modifying ITO surfaces with a cell-adhesive layer that control the adsorption of nonspecific bio-agents, ii) the compatibility of the setup with optical microscopy techniques, especially fluorescence microscopy, and iii) the system compatibility with non-Faradaic measurements in cell media were required to be examined.

CHAPTER 4 MONITORING THE KINETICS OF CELL ADHESION TO ENGINEERED ITO SURFACES

4.1 INTRODUCTION

The stationary and dynamic interactions of the extracellular matrix (ECM) and cells are of particular importance not only to provide the mechanical support but also to modulate many cell functions. Precise control over the composition and the arrangement of the cell-surface interface is needed to provide fundamental understanding of cell behaviors *in vitro* [71]. Artificial surfaces have been broadly coated with ECM proteins [172], adhesive polymers [73], or a monolayer of RGD molecules [157] to mimic the function of ECM. In some cases, the ambiguity of how the actual cell adhesive ligands are presented in protein and polymeric adhesive surfaces may compromise the robustness of the conclusions reached [72]. Surfaces with rigorous molecularly engineered RGD expression can be used to achieve more comprehensive understanding on cell surfaces interactions [20, 56]. The importance of the expression of RGD expression was discussed in Chapter 1, § 1.8. It has been shown that slight alterations in type [77, 78], the organization [82], the surrounding molecules [84], and spacing [79-81] of RGD ligands significantly modulate different aspects of cell behavior including cell adhesion and spreading.

Optical microscopy techniques have been widely used to acquire information on cell-surface interaction based on cell density, spreading and the state of focal adhesions and adhesion proteins [81, 238, 239]. However, due to the complexity of cell adhesion processes, it is crucial to recruit methodologies that can provide more detailed information on different aspects of these events [240, 241]. Recent

advances in methods such as infrared spectroscopy, microgravimetry and probe microscopy provide valuable information about different steps of cell conformational alterations[171]. Non-invasive and label-free methods represent a significant advance in cell biology as there is the possibility to provide precise insights into cell adhesion and spreading processes in a real-time manner.

The excellent time resolution of impedance spectroscopy in cell-based assays provides the potential for an in-depth investigation on the kinetic of cell adhesion. In this technique, the attachment and spreading state of cells on the electrode surfaces define the impedance values that are employed to analyze the cell function. The applied alternative current is weak and non-invasive (around 4 mA/cm^2) that enable the measurement over extended periods of time [55]. Impedance measurements are sensitive to changes within the nanometer range in cell diameter and sub-nanometer range in the distance between the ventral cells membrane and the electrode surface [147]. For instance, this system has been used to study many aspects of call-surfaces interactions including the impact of modifying the surfaces with various ECM proteins on the dynamic of cell adhesion [173, 174]. These studies demonstrated that the type, concentration and electrical charge of the coated proteins modulated the dynamic and kinetic of cell adhesion. The application of impedance spectroscopy can be extended to investigate the impact of the expression of RGD as the most frequent sequences in ECM proteins on the kinetic of cell attachment and spreading. [17]

These chapters aimed to study the modification of engineering the electrode surfaces with different densities of RGD molecules, developing the simultaneous

optical/electrochemical impedance setup on the engineered interface, and using the setup to study the effect of RGD spacing on the kinetic of cell attachment and adhesion.

A major research tool to study cell spreading is the use of live-cell optical microscopy. This powerful technique is difficult to implement on gold due to thin films of gold not being completely optically transparent and quenching of fluorophores. Due to these limitations and the fact that ITO is optically transparent and therefore superior to gold surfaces for cell biological behavior studies requiring optical microscopy techniques. Therefore the measurements were performed using real-time impedance spectroscopy and optical microscopy on interdigitated indium tin oxide (ITO) electrodes. The most sensitive and relevant condition for measuring the alterations in cell spreading was determined by correlating the resistance and capacitance values with the amount of cell coverage on the surface. The cell area was calculated by analyzing the phase contrast microscopy images. Impedance spectroscopy and microscopy images were monitored since seeding cells until the formation of the cell monolayer, while cells were seeded on interdigitated ITO surfaces with dense or spare RGD spacing.

4.2 EXPERIMENTAL SECTION

4.2.1 Electrode surface modification

Plain ITO and interdigitated ITO electrodes were cleaned according to Chapter 2, § 2.3.1.Then, ITO surfaces were modified using a multi-step method as has been summarized in Schematic 4-1 as explained in Chapter 2, § 2.3.4.

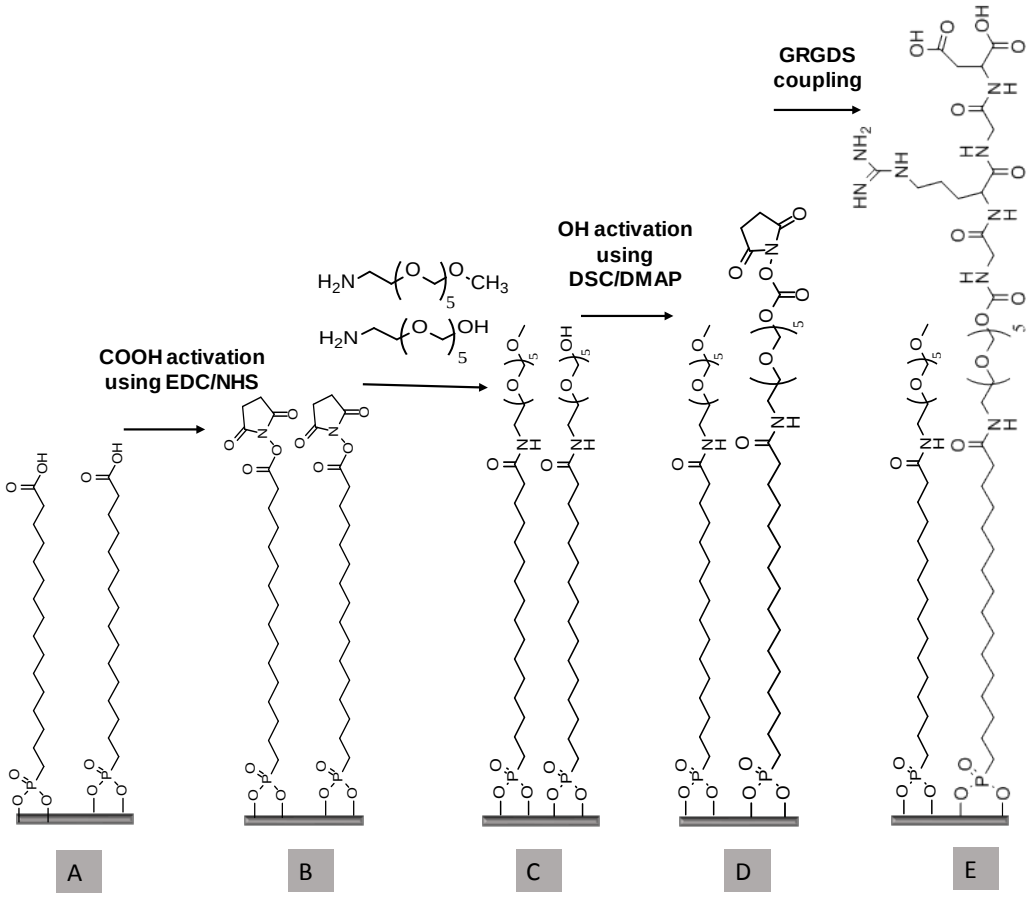

Schematic 4-1. ITO surface modification steps; Carboxyl-terminated PHDA base layer SAMs were activated with EDC/NHS, followed by coupling with different ratios of 1-aminohexa(ethylene oxide) to 1- aminohexa(ethylene oxide) monomethyl ether molecules. Hydroxyl-terminal groups of tetra(ethylene oxide) were activated and coupled with GRGD

4.2.2 XPS measurement

XPS measurements were performed after each step of ITO surface activation and medication using the strategy explained in Chapter 2, § 2.5.2. The calculations

on RGD spacing was carried out based on XPS characterizations on these surfaces except in the last step of modification, which includes the coupling of GRGDS peptides, GRGDC−Alexa Fluor 647 was used. Alexa Fluor 647 contains thiol groups detectable using XPS measurements.

4.2.3 Cyclic voltammetry

The cyclic voltammetry (CV) for evaluating the modification process was performed as explained in Chapter 2, § 2.5.1.

4.2.4 Cell culture

HeLa cells were grown as explained in Chapter 2, § 2.4.1. To plate the cells on the surfaces, the detached cells were re-suspended in fresh media and counted followed by seeding 7×10^4 cells/ cm^2 on each modified interdigitated ITO surface.

4.2.5 Phase contrast microscopy

The sequences of phase contrast images were obtained using a Zeiss Axio Observer X.1 Spinning Disk/TIRF inverted microscope as discussed in Chapter 2, § 2.5.3.

4.2.6 Electrochemical impedance spectroscopy

The non-Faradaic frequency-resolved impedance values of the cells on the surfaces were recorded after seeding cells for 15 h in real-time on interdigitated ITO electrodes (with an active surface area of 1.3×10^{-4} cm^2) with a weak non-invasive AC signal within 40000-400 Hz (10 mV) as described in Chapter 2, §

2.5.1. The impedance values of modified cell-free interdigitated ITO electrodes were monitored to obtain the baseline data before seeding cells. The impedance value has been normalized by dividing the impedance of cell-covered electrode to the impedance of the respective cell-free electrodes.

4.3 RESULTS AND DISCUSSION

4.3.1 XPS Characterization of ITO Modified Surfaces and RGD spacing estimation

The core level XPS spectra for carbon, nitrogen and phosphorous on ITO surface after each steps of modification including (A) modification of ITO with PHDA, (B) activation of COOH groups using EDC and NHS (C) attachment of H_2N-EO_6-OH and H_2N-EO_6-OCH_3, (D) activation of NH_2 groups using DSC and DMAP (E) attachment of the GRGD peptide is shown in Figure 4-1.

The P 2p core level regions of XPS analyses show a main peak centered at around ~133.5 eV assigned to the phosphonate group. The C 1s high-resolution spectra were fitted with several peaks with the main peak centered at ~284.5 eV, which corresponds to aliphatic carbon bonded carbon (C−C). The fitted peaks at ~286.5 eV in C 1s regions are characteristic of the carbon atoms bound to oxygen, which shows an increase in its size in the case of the modifying surface using ethylene oxide rich molecules. The high binding energy peak at around 289.5 eV assigned to the carboxyl functional groups. The emergence of new peaks at the binding energy related to the carbonyl group, which is 287.5–288.1 eV,[242] were

observed in the C 1s core level region of surfaces after carboxyl activation, ethylene oxide molecules attachment, DSC activation, and GRGDS coupling. The N 1s region shows the absence of nitrogen peak after the first step of modification using PHDA layer. However, after activation with EDC and NHS, the N 1s signal was detectable at ~402 eV in the survey scan assigned to an active succinimide ester-terminated SAM, and at ~399.8 eV attributed to *N*-acylurea intermediates. After putting ethylene oxide molecules on the surface, the high-resolution N 1s scan was deconvoluted with fitting to two functions: a peak at ~399 eV, attributed to *N*-acylurea intermediates and a peak at 400.1 eV correlated to the formation of an amide bond, which show successful nucleophilic binding of the 1-aminohexa(ethylene oxide) molecules. In the N 1s narrow scans of the DSC-activated ITO surface (D), the spectra were fitted with two peaks centered at ~400 eV and ~402 eV attributed to amide bound and the succinimidyl esters, respectively. The GRGDS modified surface was fitted with the similar peaks as 1-aminohexa (ethylene oxide) in the N 1s region; however, an increase in the peak at 400 eV, originating from amide groups within the peptide on the surface further supports that cell adhesive GRGDS peptides were attached to the activated succinimidyl ester terminated SAM via formation of amide bonds.

XPS results were used to estimate the RGD spacing of the prepared surfaces using a strategy that reported in The Gooding group, previously [238]. Briefly, the coupling efficiency of the connecting of 1-aminohexa(ethylene oxide) molecules to SAM and GRGDS to activated hydroxyl groups were calculated from XPS data to be approximately 72% and 42%, respectively. Thus, the overall efficiency

was calculated to be 34%. The surface coverage of organophosphonate has been reported to be around 4×10^{14} molecules/cm^2 by the Reven group [243]. Therefore, the estimated average spacing between adhesive ligands for the surface modified with 100% 1-aminohexa(ethylene oxide) molecules was calculated to be 1 nm. Subsequently, the average RGD spacing for surfaces modified with 1:10^3, 1:10^6 or 1:10^9 ratios of 1- aminohexa(ethylene oxide) monomethyl ether to 1-aminohexa(ethylene oxide) were estimated to be 31 nm, 968 nm, and 30597 nm, respectively.

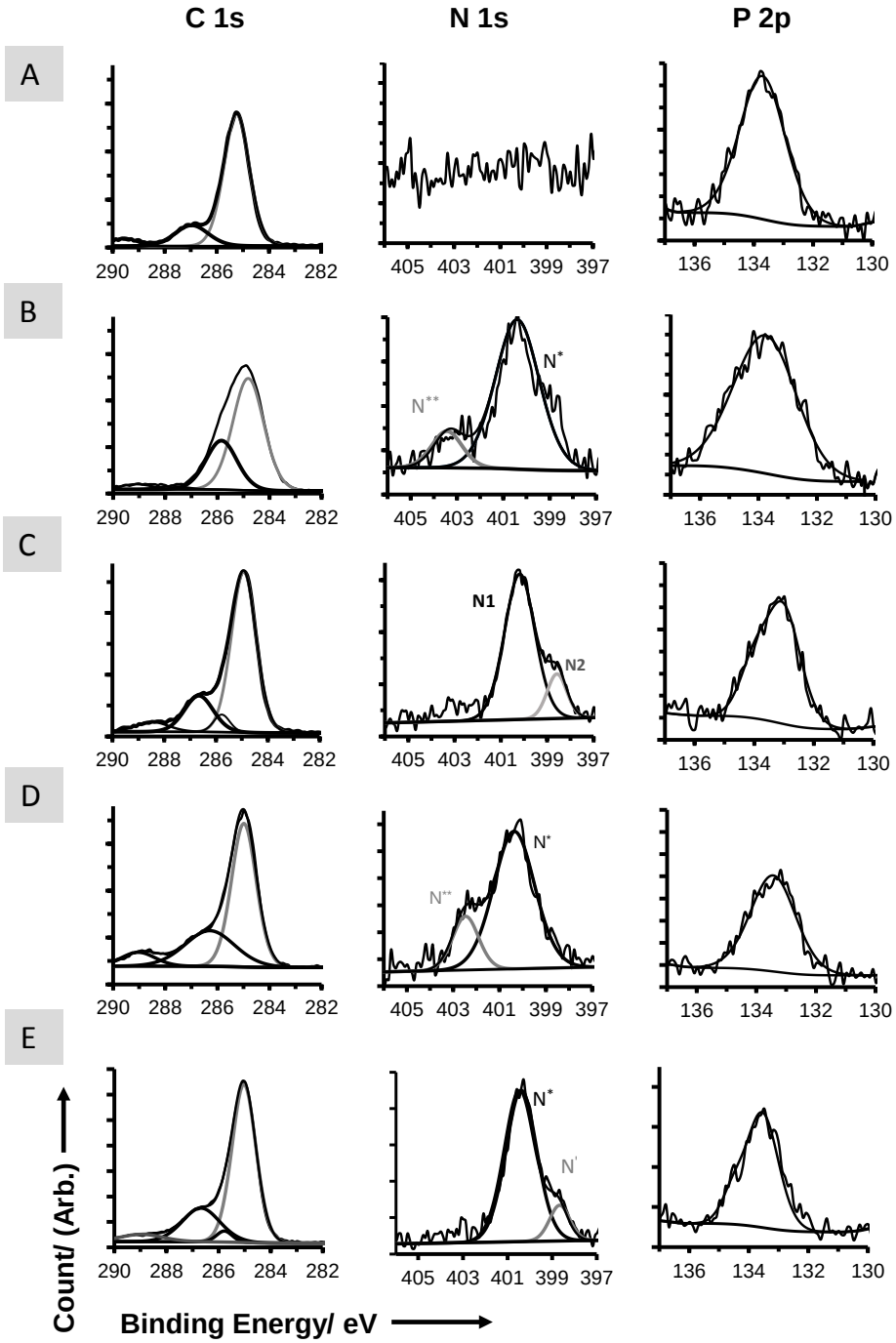

Figure 4-1. C 1s, N 1s, and P 2p XPS analysis of ITO surfaces after each step of modification: (A) carboxyl terminated PHDA SAM, (B) carboxyl group activation using EDC/NHS (C) 1-aminohexa (ethylene oxide), (D) hydroxyl group activation using DSC/DMAP, and (D) GRGD attachment.

4.3.2 Electrochemistry for PHDA SAM on ITO surface

Passivation of ITO surfaces after self-assembly of the PHDA on the ITO surface was confirmed using potassium ferricyanide as the redox probe. Figure 4-2 shows cyclic voltammograms before and after modification of an ITO electrode with self-assembled PHDA and then with GRGDS in 1 mM ferricyanide at a scan rate of 100 mV s^{-1}. The self-assembled layer shows suppression effect compare to bare ITO, providing good evidence of a well formed PHDA layer on the ITO surface. The ITO was then modified next with GRGDS peptides via activated OH groups grafted onto the ITO. Figure 4-2 b shows the modification with GRGDS peptides suppressed the cyclic voltammogram more than modification with SAM PHDA.

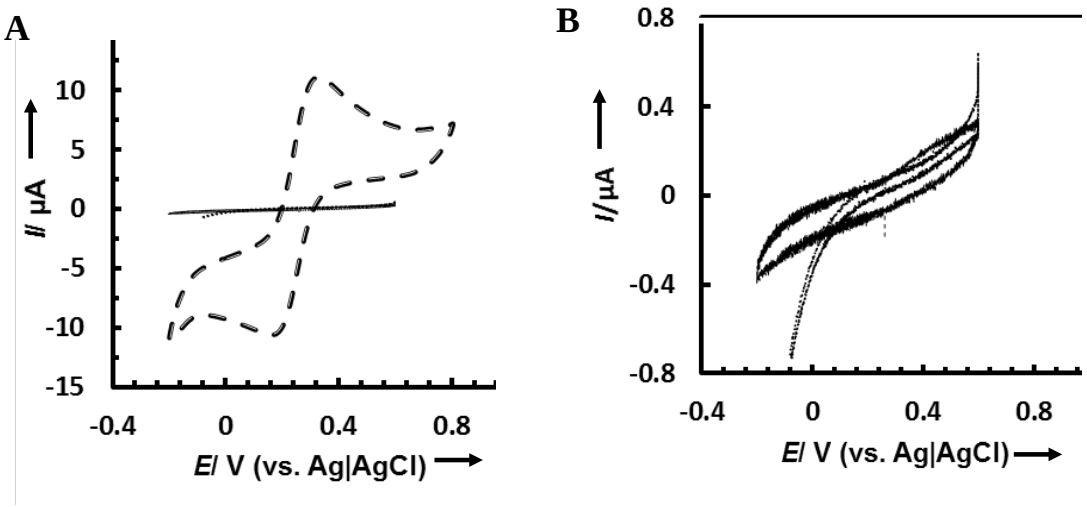

Figure 4-2. (A) Cyclic voltammograms recorded in 1 mM ([Fe(CN)6]−3/−4) redox couple containing 0.1 M potassium chloride at the scan rate of 0.1 Vs-1 for bare interdigitated ITO (dashed line), PHDA SAM- (solid line), and GRGDS (dotted line) modified surfaces. (B) Magnified presentation of cyclic voltammograms of PHDA SAM-modified ITO (solid line) and GRGDS modified ITO surface (dotted line). The reduction in current is an indication of the surface passivation after each step of modification.

4.3.3 Simultaneous impedance spectroscopy and optical microscopy setup

To perform optical microscopy and impedance spectroscopy, simultaneously, a primary design compatible with inverted microscopy and electrochemistry measurements were implemented in a glass Petri dish. It was by adhering wires to specific places for different electrodes on interdigitated ITO electrodes (Figure 4-3).

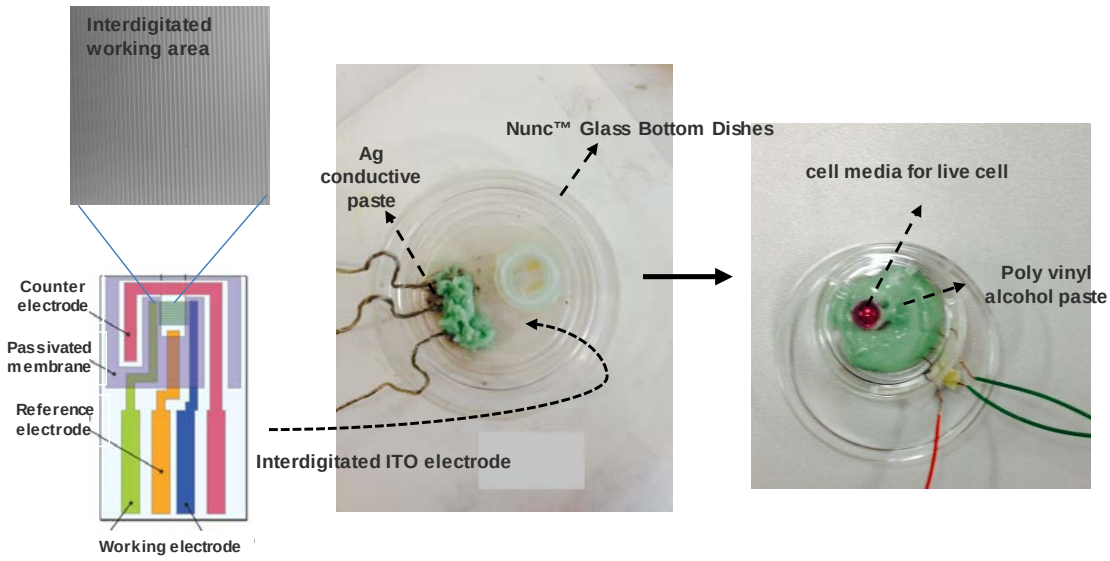

Figure 4-3. The Primary design of the optical/electrical chamber for interdigitated ITO electrodes.

Based on the primary design, a chamber compatible with electrochemical and inverted microscopy measurements and suitable for the interdigitated electrodes was designed (Figure 4-4). The chamber was equipped with a printed circuit board and electrical pins that connect to the counter, reference and interdigitated working electrodes, made by Micrux Technologies (Oviedo, Spain). It was placed on microscope stage and was connected to the potentiostat (SP 200,

BioLogic, Science Instruments) to run optical and electrochemical measurements, simultaneously. For this purpose, after inserting a modified interdigitated ITO electrode into the chamber, the cell media containing HeLa cells were placed on the surface. Pictures taken from the simultaneous setup and the custom-made electrochemical/optical chamber are shown in Figure 4-5. The chamber has a printed circuit board with electrical pins that connect the counter, reference and interdigitated working electrodes. The experimental conditions were kept ideal for live cells by controlling the temperature at 37 °C and the atmosphere humid with 5% CO_2 in the microscope cage.

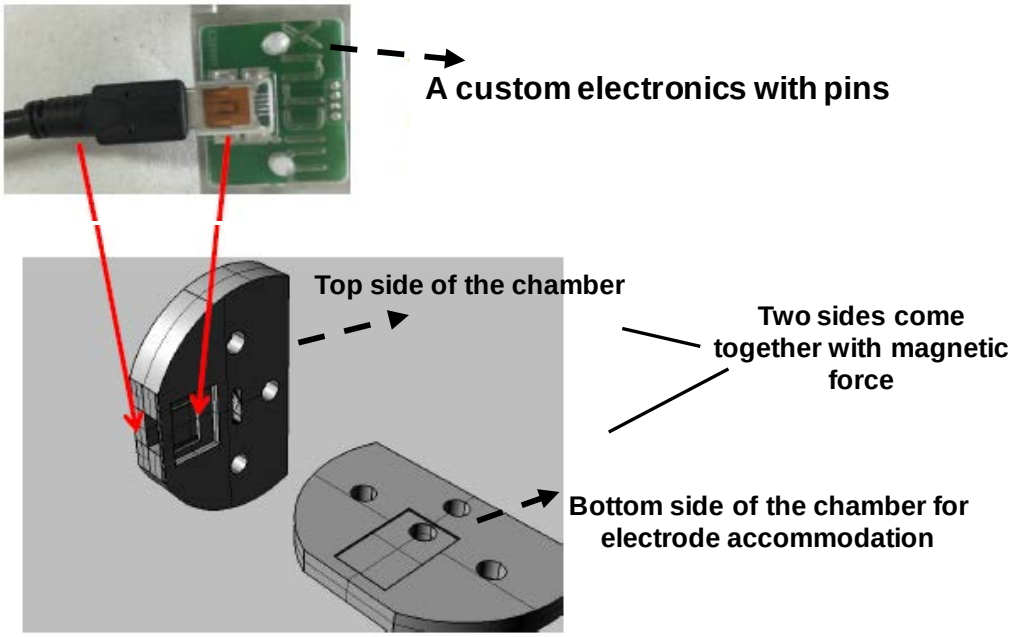

Figure 4-4. The design of the custom-made chamber compatible with inverted optical microscopy, electrochemistry and interdigitated ITO electrodes

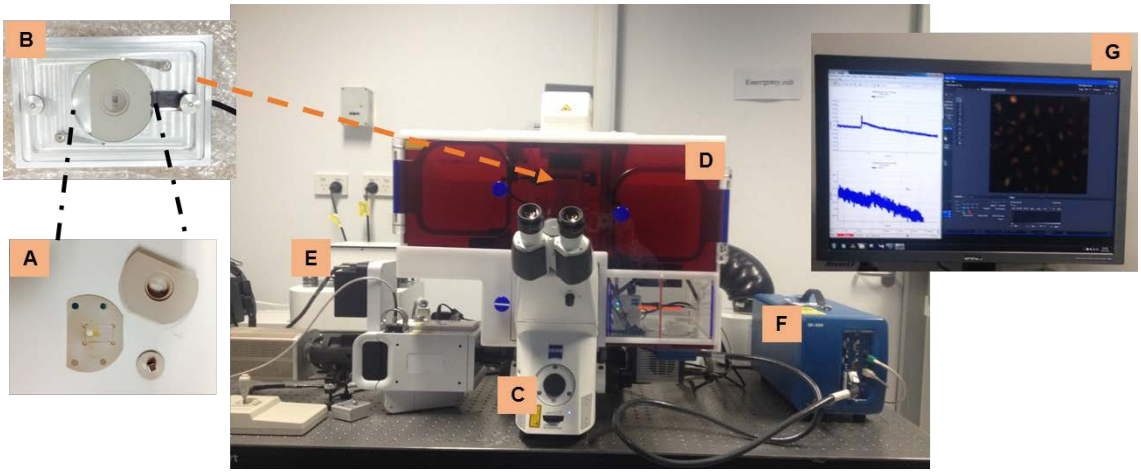

Figure 4-5. Components of simultaneous live microscopy and impedance spectroscopy measurements setup; (A) the custom-made chamber for interdigitated ITO electrodes, (B) the microscope stage, (C) Inverted microscope, (D) the microscope cage, (E) Temperature and CO2 controller units, (F) potentiostat and (G) a personal computer.

4.3.4 Cells spreading on ITO modified surfaces

The feasibility of running phase contrast microscopy and impedance measurement was examined by tracking the attachment and spreading of HeLa cells on interdigitated ITO electrodes modified with fibronectin. HeLa cells were cultured on interdigitated ITO electrodes and their attachment and spreading were followed for 15 h. Figure 4-6 shows an example of simultaneously recorded impedance data and microscopy images. The values of impedance (Z) has been normalized to the corresponding value of a cell-free electrode ($Z_{electrode}$). The impedance value here has been reported for 4000 Hz [173]. The recorded impedance data showed three different time courses. After 3-10 minutes of cell seeding, the value of impedance slowly increased ($t < 1$ h) from the value of cell-free electrode. According to the phase contrast images, the initial binding of cells on the surface contributed in onceasing the impedance values. Then, the

impedance increased dramatically (1 h < t < 4 h) mainly due to the adhesion and spreading of cells. After 6 h, the changes in impedance was predominantly attributable to the establishment of cell-cell junctions rather than increase in cell spreading based on optical microscopy images. The formation of mature cell junctions restricts the current flow through the gaps between cells

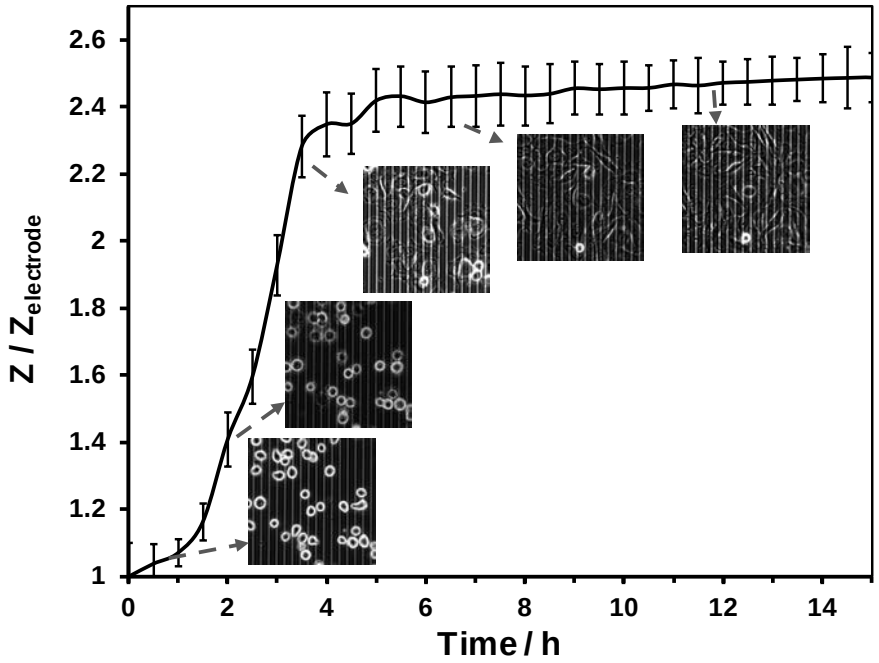

Figure 4-6. The time course of impedance spectroscopy is attributed to various steps of cells attachment and spreading according to simultaneous impedance spectroscopy and phase contrast microscopy measurements. The normalized impedance values were obtained by dividing the relevant impedance value of the cell-cultured electrode (Z) to the value of cell-free electrode ($Z_{electrode}$). The arrows indicate the time point of the relevant phase contrast microscopy images. Interdigitated ITO electrodes were inserted into a custom-made chamber compatible with both inverted microscopy and impedance spectroscopy.

The frequency used for the impedance measurement is one of the most crucial parameters that dictate the sensitivity of experiments that use impedance to

monitor changes in cells. In order to recognize the most sensitive frequency, the resistance and capacitance of cell-covered ITO electrodes during the attachment of initially suspended HeLa cells over the frequency range of 40000-400 Hz were monitored. The changes in these values were compared versus the alteration in the surface coverage by cells over time. In this study, three major frequencies explored were explored being 400, 4000 and 40000 Hz as has been reported previously [244]. The strategy of measuring cell area using phase contrast images are illustrated in Figure 2. The electrodes were covered with an insulating membrane to restrict the electrochemical measurement to the interdigitated ITO area (65 pairs with 10 μm width and 5 μm spacing between each electrode). A motorized stage was used to capture the whole electrochemically active area of the interdigitated ITO every 15 or 30 minutes. The cell covered area was calculated using ImageJ software (US National Institutes of Health, Bethesda, MD) by removing the trace of ITO and calculating the area of cell regions. To provide a more systematic comparison, the amount of cell coverage was divided by the total area of the images to acquire relative surface coverage values. Furthermore, the resistance and capacitance values have been divided by the corresponding values of the cell-free electrode and are represented as normalized resistance and capacitance, respectively. As is shown in Figure 4-8, the changes in the resistance values versus surface coverage calculated from the phase contrast microscopy exhibited a slow increase followed by a sharp rise until the whole surface was covered with a confluent layer of cells (relative surfaces coverage of 1). The largest change in resistance occurred at 40000 Hz, whereas

the highest alteration in capacitance happened as 40000 Hz (Figure 4-8). This is in agreement with results reported by Giaever and co-workers, [244] where the changes in resistance and capacitance have been correlated versus the estimated cell area obtained based on a numerical calculation. This mathematical model predicts the morphological parameters of cells based on the impedance of a cell-covered electrode [147, 159].

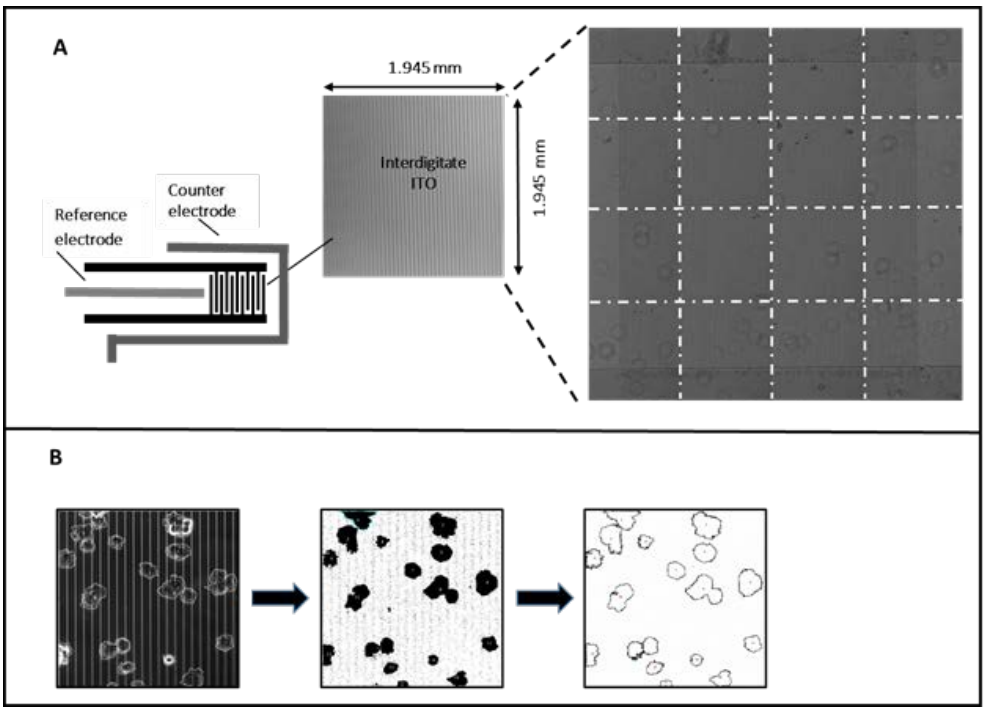

Figure 4-7. The phase contrast images were used to calculate the surface coverage by cells on the electrode. (A) The whole electrochemically responsive area of the electrode was imaged by defining tiles all over the interdigitated part using ZEN software and a motorized stage. Images were recorded every 15 min or 30 min. (B) ImageJ was used to analyze the images. A "clean up" plugin was used to remove the trace of interdigitated electrodes from recorded images and then "Threshold" option was used to calculate the amount of cell coverage on the surface by manually tracing the area around cell regions.

It has been demonstrated that the surface characteristics regulate the cell phenotype and cell signaling [245, 246]. This has motivated chemists to develop

various chemical layers on the surface in order to optimize the cell function or provide a more comprehensive understanding of various cell behaviors [20, 247]. Here, the potential influences of various spatial distribution of RGD on the dynamic of cell adhesion and spreading were investigated. For this purpose, interdigitated ITO electrodes were modified with dense and spare GRGDS molecules using a multi-step strategy. XPS was used to confirm the attachment of different molecules after each step, and the results were used to estimate the average RGD spacing on the surfaces based on the method developed by the Gooding group [238]. To this end, the coupling efficiencies of the attachment of 1-aminohexa(ethylene oxide) molecules to 16-phosphohexadecanoic acid self-assembled monolayer (PHDA-SAM) and to GRGDS moieties were approximated from XPS data to be 72% and 42%, respectively. Therefore, the overall efficiency was calculated to be 34% for the surface modified with 100% of 1-aminohexa(ethylene oxide) molecules. The Reven group [243] has reported the surface coverage of organophosphonate molecules on the surfaces to be 4×10^{14} molecules/cm^2. Thus, the estimated average spacing between RGD adhesive ligands for the surface modified with 1-aminohexa(ethylene oxide) molecules in the absence of 1-aminohexa(ethylene oxide) monomethyl ether was estimated to be 1 nm. Subsequently, the average RGD spacing for surfaces modified with $1{:}10^3$, $1{:}10^6$ or $1{:}10^9$ ratios of 1-aminohexa(ethylene oxide) monomethyl ether to 1-aminohexa(ethylene oxide) were calculated to be 31 nm, 970 nm, and 31000 nm, respectively.

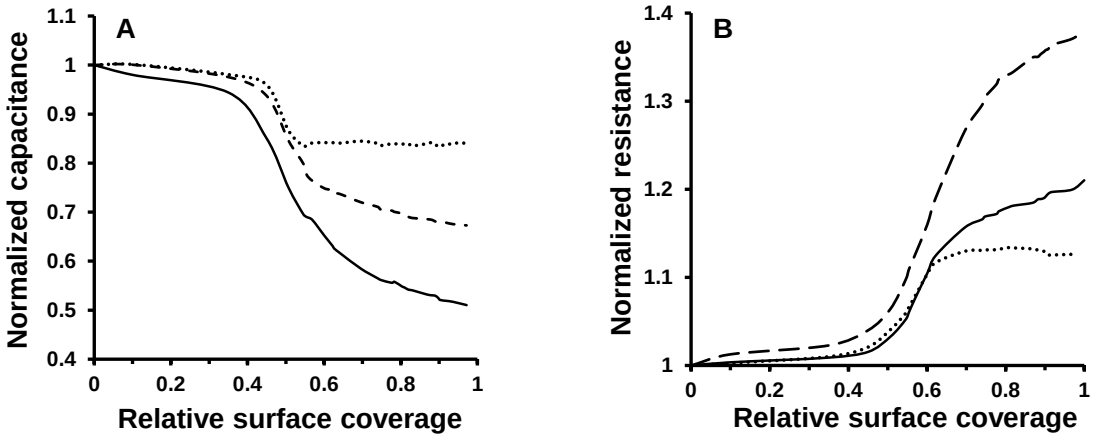

Figure 4-8. Normalized resistance (A) and capacitance (B) as a function of the relative surface coverage. The cell-covered area was manually calculated by analyzing recorded phase contrast microscopy images as was explained in Figure 4-6. The results were reported at 40 kHz (dash curve) 4 kHz (Solid curve) and 400 Hz (dot curve) frequencies. For better comparison, the resistance and capacitance values were normalized to the corresponding value of naked electrode. The relative surface coverage was calculated by dividing the area of the cell-covered region to the total image area. Normalized resistance and capacitance show the biggest change at 4 kHz and 40 kHz, respectively, by alteration of cell converge.

Figure 4-9A illustrates the time course of change in capacitance at 40000 Hz with a time resolution of fewer than 2 minutes for cells on surfaces modified with average RGD spacing of 1 nm, 31 nm, 970 nm and 31000 nm. In addition, the adhesion process was also studied for the surfaces modified with only 1-aminohexa(ethylene oxide) monomethyl ether molecules and not 1-aminohexa(ethylene oxide) molecules (No RGD). The capacitance of cells on interdigitated ITO surfaces with various RGD densities reached to their minimum values in different time scales. Based on the study by Giaever and co-workers [244], two factors from the time course of capacitance data have been extracted; the required time to reach the half-maximum capacitance decrease ($t_{1/2}$) and the average slope of capacitance change ($-\Delta C/\Delta t$). In their study, these parameters

have been used to compare the cell adhesion on gold surfaces coated with different ECM proteins. This provides a more systematic comparison on the kinetic of cell adhesion processes. The parameter of capacitance shift ($-\Delta C/\Delta t$) was determined based on the average slope of the curve between the normalized capacitance of 0.9 and 0.7 by means of a linear regression. According to Figure 4-8, in this range of capacitance shift, cells have covered 45-55 % of the surface area. This term represents the relative rate of cell spreading [244]. From Figure 4-9, $t_{1/2}$ was determined to be 1.4 h on the surfaces with 31 nm average RGD spacing, 2.2 h for the surface with 1 nm average RGD spatial distribution. This value was 3 h and 3.4 h for the surfaces with 970 and 31000 average RGD spacing, respectively. The value of $t_{1/2}$ was determined to be 5.5 h for cells on the surface with no RGD. The capacitance shift (Figure 4-9B) for cells on the surface with 31 nm RGD spacing was shown to be at least 2.2 fold higher than on the surface with 970 nm or 31000 nm average RGD spacing. These results demonstrated the faster kinetic of cell adhesion and spreading on a surface with average RGD spacing of less than 31 nm.

An expansion of the normalized capacitance for the first 2 h after cell seeding are shown in Figure 4-9C and D as wells as the phase contrast images recorded at time points of 15 min, 1 h, and 2h. The normalized capacitance decreased immediately on the surfaces with 1 nm and 31 nm average ligand spacing. In early stages of adhesion process, cells extend protrusions of cell membrane toward the adhesive ligands on the surfaces [248]. These protrusions reach stability by adhesions between the integrins in the actin cytoskeleton to RGD

adhesive ligands on the surface. Figure 4-9E shows that higher number of cells have developed protrusions in first 1 h on the surface with 31 nm RGD spacing compared with on surfaces with lower or greater RGD spacing. It has been shown that surfaces with less than 70 nm RGD spacing induce the higher cell density and greater cell-covered area [79, 80]. This range of RGD spacing mimics similar RGD distribution in adhesive proteins such as fibronectin [249].

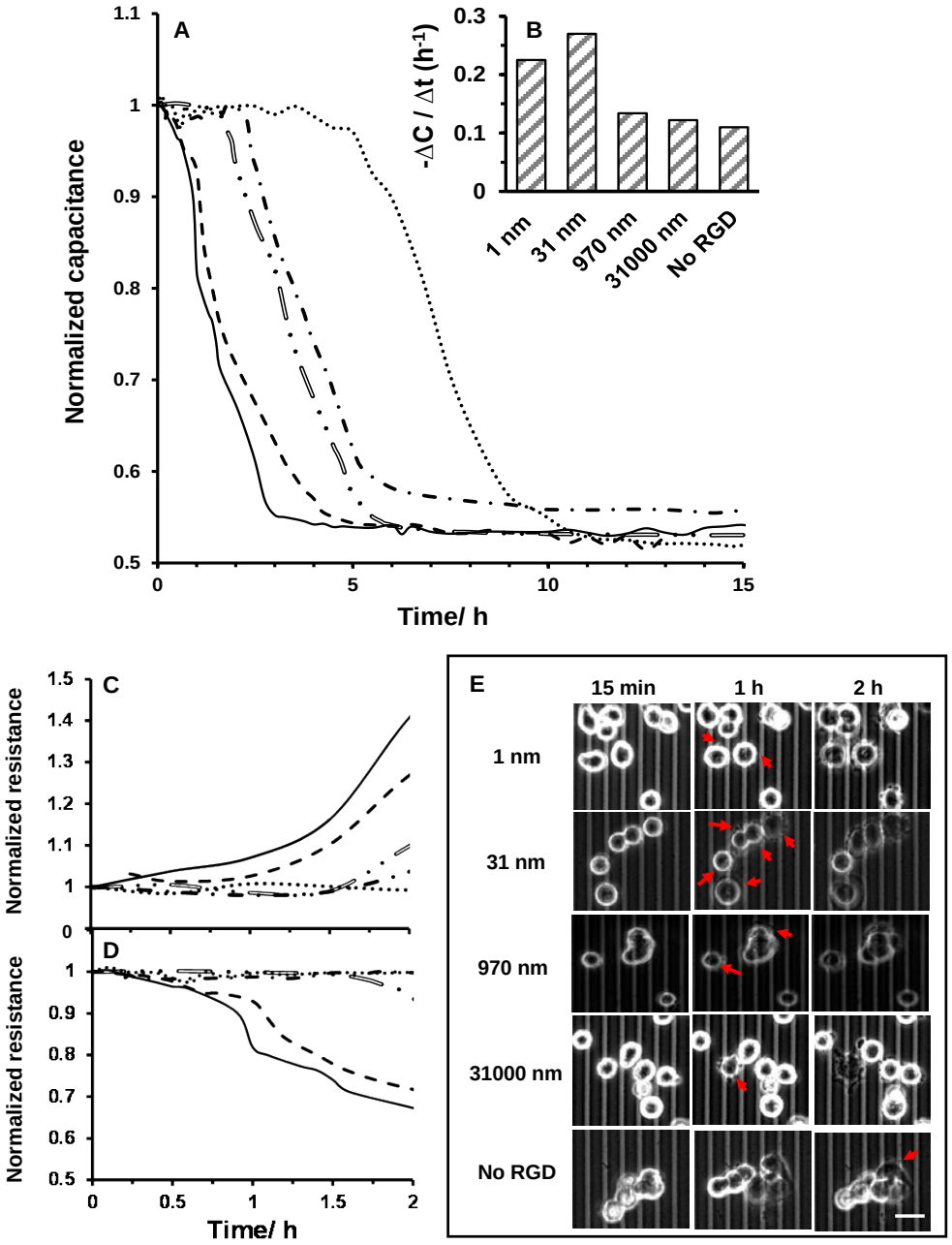

Figure 4-9. Modifying interdigitated ITO surfaces with different RGD spacing regulates cell attachment and spreading. (A) The normalized capacitance over time is calculated by dividing the value of capacitance to the corresponding value of bare electrode ($C_{electrode}$) at 40 kHz for cells on the surfaces of RGD spacing of 1 nm (dashed line), 31 nm (solid line), 970 nm (hollow dashed line), 31000 nm (dash-dotted line) and the surface with no RGD (dotted line). HeLa cells were cultured on interdigitated ITO surfaces modified with different RGD spacing and the attachment and spreading was tracked in real-time over 15 h. The cells on surfaces with 31, 1, 970, 31000 nm RGD spacing and the surface with no RGD demonstrated the fastest to the slowest cell adhesion, respectively. (B) The quantities here called capacitance velocity were

extracted from the respective normalized impedance time courses to improve the comparison of cell spreading on interdigitated ITO surfaces modified with different RGD densities. The values of $-\Delta C/\Delta t$ values were extracted from the slope the curve between C/Celectode = 0.9 and C/Celectode=0.7. Magnified presentation of resistance at 4 kHz (C) and capacitance at 40 kHz (D) during the first two hours of the experiment. (E) Examples of the relevant live cell phase contrast microscopy images, recorded simultaneously with impedance measurement, on different modified surfaces at three time points of 15 min, 1 h, and 2 h after cell seeding. Arrows indicate examples of formed lamellipodia. The cells start to spread on the surface with 31 nm of RGD spacing at a higher rate according to impedance results and developed more membrane protrusions compared to the other studied interfaces. Scale bar is 25 µm.

4.4 SUMMARY

Electrochemical impedance spectroscopy coupled to phase contrast microscopy on chemically modified interdigitated ITO electrodes worked efficiently to study the dynamic of cell-surfaces interactions over long-term. The coupling of impedance spectroscopy and phase contrast microscopy provided the possibility of correlating the resistance/capacitance data to the amount of coverage of cells on the surface. The results demonstrated that the changes in capacitance at 40000 Hz mirror the adhesion and spreading of HeLa cells on the surface with the highest sensitivity. The surfaces with average RGD spacing of 31 nm displayed the highest rate of change in capacitance than other surfaces with greater or lower ligand spacing. The results presented in this chapter confirmed the applicability of the developed simultaneous impedance cell-based system on interdigitated ITO was confirmed in providing precise and real-time information on complex cell-surface interaction. These findings revealed the importance of RGD, adhesive cues, expression in regulating the kinetic of cell-surface interaction. Next, the effect of the expression of these physical cues on regulating the cell responses to soluble cues has been studied using the developed setup.

CHAPTER 5

SIMULTANEOUS IMPEDANCE SPECTROSCOPY AND LIVE CELL FLUORESCENCE MICROSCOPY

5.1 INTRODUCTION

Many environmental cues, including a large number of prescription drugs, target cells through G-protein-coupled receptors (GPCRs) as the largest family of cell surface receptors [250, 251]. The binding of an external signal to a GPCR typically results in the stimulation of complex interconnected signalling pathways through which cells coordinate a wide variety of fate decisions. Therefore, there is a tremendous interest in developing cell chip technologies based on monitoring different events upon the activity of GPCRs [187]. The kinetics of these cellular pathways differ significantly from the millisecond's timescale (e.g., GPCR conformational changes or Ca^{2+} flux) to hours (e.g., cytoskeletal modulation) [252]. The GPCRs monitoring technologies are mainly based either on optical measurement [253] or electrical detections [190, 254, 255]. Among them, fluorescence microscopy [256] and electrical impedance spectroscopy [55] are two of more popular methods, which, in fact, are complementary. Fluorescence microscopy enables the precise monitoring of short-lived specific subcellular processes, organelles and proteins with labelled fluorescent tags [256]. In contrast, cell-based impedance measurements, pioneered by Giaever and Keese [147], provide real-time information on minute changes in adhesion of cells to cells/surfaces at the whole-cell level over extended periods of time in a label-free manner.

In organisms, cells are surrounded by an extracellular matrix which contains adhesive ligands that modulate cell behaviour. Hence, using molecularly

engineered surfaces with controlled expressions of cell adhesive ligands is beginning to become more prevalent in the development of cell chips [20]. It has been demonstrated that various spatial distribution of adhesive RGD ligands regulates not only the cells phenotype but also the outside-in and inside-out signalling processes [69, 80, 81]. However, the knowledge of how the dynamic of cellular responses to a soluble cue is influenced by surface chemistry is in its infancy and is of significant importance in testing drugs *in vitro*.

Here, the combination of impedance spectroscopy and live fluorescence microscopy, simultaneously, to provide a platform technology to investigate GPCRs activity in a more comprehensive manner was studied. This is achieved using optically transparent interdigitated indium tin oxide (ITO) electrodes which have been shown can be precisely modified with self-assembled monolayers to given biointerfaces with the precise presentation of cell adhesive ligands. The fluorescence microscopy was utilized to monitor transient histamine-induced Ca^{2+} release from endoplasmic reticulum (ER) stores. Impedance spectroscopy was employed to acquire information on dynamic changes in cell adhesion that can be regulated by both surface chemistry and the soluble GPCRs stimulators. The coupling of the fluorescence and impedance readout methods is particularly relevant for tracking events with significantly different time scales but connected through GPCRs which would not be possible using a single detection method. Furthermore, the developed technique was employed to not only investigate the effect of surface design in modulating the cellular responses to soluble cues but also reveal possible correlations between the timescales of the connection of

calcium signalling and cell spreading. The measurement principles of the work have been summarized in Schematic 6-1.

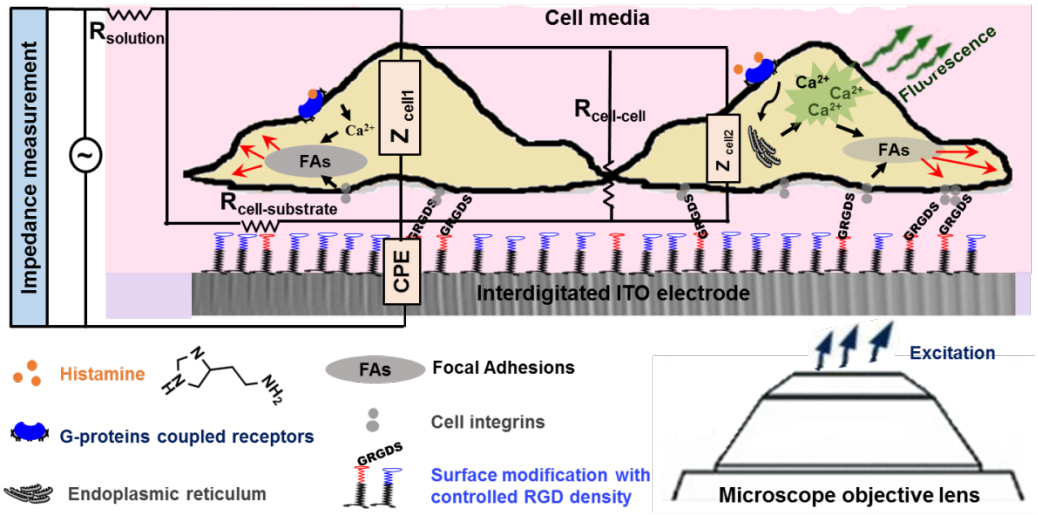

Schematic 5-1. The designed simultaneous setup for collecting more comprehensive information on cells response to soluble cues in the presence of tuned adhesive ligands on an interdigitated indium tin oxide (ITO) surface. Histamine was used as a model soluble cue ligand which activates G-protein coupled histamine receptors, and, consequently, Ca^{2+} ions are mobilized from the endoplasmic reticulum (ER), and the cytoskeleton arrangement undergoes alteration through focal adhesions remodelling. The presence of Gly-Arg-Gly-Asp-Ser (GRGDS), adhesive ligands to cell integrins, leads to focal adhesion formation and signalling. The experimental impedance measurements are subjected to an equivalent circuit model with Z_{cell} being the impedance of the cell, a constant phase element (CPE) which corresponds to the impedance resulting from the cell-surface area and $R_{solution}$, $R_{cell\text{-}cell}$ and $R_{cell\text{-}surface}$ which are the resistance of solution, cell junctions and cell–substrate contacts, respectively.

5.2 EXPERIMENTAL METHODS

5.2.1 Preparation of RGD controlled surface

Interdigitated ITO electrodes were first modified with carboxyl-terminated PHDA SAM. 1-aminotetra(ethylene oxide) molecules with either hydroxyl or methoxy groups were attached to the surface after activating the carboxyl groups

of PHDA molecules. The hydroxyl-terminated 1-aminotetra(ethylene oxide) (H_2N-EO_6)molecules were attached to GRGDS peptides to provide the cell adhesion properties. The ratio of 1-aminotetra(ethylene oxide) molecules was engineered to provide the surface with defined RGD spacing as has been described in detail in Chapter 2, § 2.3.4, and Chapter 4, § 4.2.1. A surface was modified only with H_2N-EO_6-OCH_3 molecules with no RGD molecules chemically attached to the surface.

5.2.2 X-ray photoemission spectroscopy (XPS) measurements

XPS analyses were conducted as has been described in Chapter 2, § 2.5.2. The RGD spacing was estimated using the XRD results as explained in Chapter 4, § 4.3.1.

5.2.3 Cell culture

HeLa cells were grown to confluence in DMEM culture media supplemented with 10% fetal bovine serum as discussed in Chapter 2, § 2.4.1. High density of 1.5×10^5 cells/ cm^2 were seeded on each modified interdigitated ITO surface for 3.5 h or until speeded on bare surfaces.

5.2.4 Loading HeLa cells with fura-2 AM

The plated HeLa cells on interdigitated ITO surfaces were washed two times using phenol red-free DMEM before being loaded with fura-2 AM dyes. The loading was performed according to optimized protocol explained in Chapter 2, § 2.5.4. The loading parameters have been optimized in this chapter.

5.2.5 Histamine solution preparation

100 µM histamine agonist was prepared by dissolving the powder in HBSS buffer and was used freshly.

5.2.6 Simultaneous live fluorescence microscopy and real-time impedance measurement

The developed simultaneous fluorescence microscopy and impedance spectroscopy setup was used for running the experiments in this chapter. The principle of the setup is explained in Chapter 4, § 4.3.3.

The setup was developed by coupling a fluorescence microscope (Zeiss Axio Observer X.1 Spinning Disk/TIRF) and a potentiostat (SP 200, BioLogic, Science Instruments). EC-Lab ® V10.33 (BioLogic, Science Instruments) software was used to collect and analyse the impedance data, and Zeiss ZEN software was used to capture the sequence of fluorescence images. Fiji software (National Institutes of Health, USA) was used to analyse the microscopy results. The microscope was equipped with a cage for controlling the conditions of live cell imaging at 37 °C with 5% CO_2. A costume made chamber made by Micrux Technologies (Oviedo, Spain) was used in the setup as has been explained in Chapter 4, § 4.3.3. The chamber with inserted interdigitated ITO electrodes covered with fura-2-loaded cells was placed on the microscope stage to allow a simultaneous live inverted optical microscopy and impedance spectroscopy.

5.3 RESULTS AND DISCUSSIONS

5.3.1 Finding the most sensitive frequency

During simultaneous measurements, the impedance values at 12 frequencies between 40000-400 Hz (10 mV) were recorded over time. The amplitude of current passed through the cells was held in the nanoampere (nA) range, which created a negligible electrical stimulation to cells during measurement. The real-time histamine-induced impedance alterations at the frequencies of 40000 (solid line) and 4000 (dash line) Hz were compared together. These frequencies are among the most studied frequencies in the literature and were first time used by Giaever group [244]. The change of histamine-induced impedance value was maximized at 4000 Hz (Figure 5-1). This is in agreement with studies by other groups on searching the frequency at which the cell layer display the greatest histamine-induced impedance alteration [145, 147, 257]. This optimal frequency has been selected for further characterizations, except the modelling studies which involve the impedance reading at the whole frequency range.

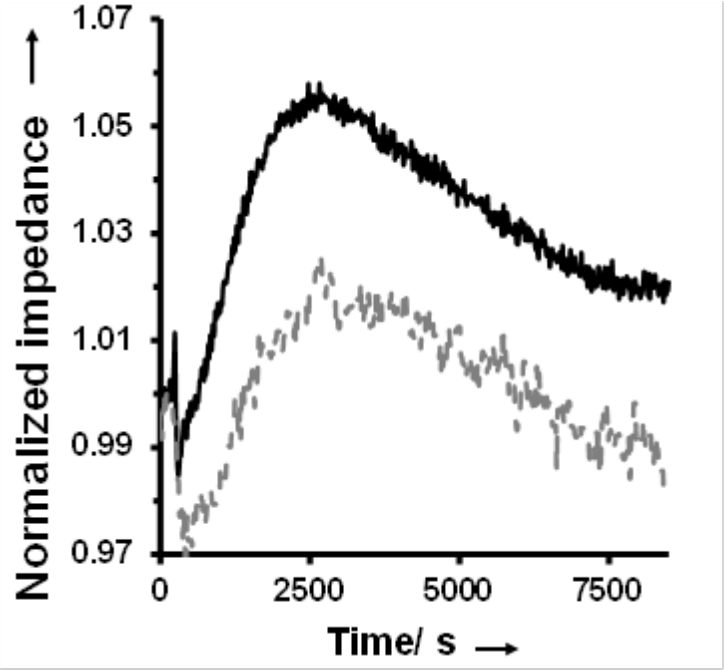

Figure 5-1. The normalized impedance changes were calculated by dividing the value of the histamine-induced impedance of the cell-covered electrode to the impedance value of cells before histamine stimulation at frequencies of 4000 Hz (gray dash line) and 40000 Hz (black line). The impedance measurement at the frequency of 4000 Hz showed the broadest range of relative change.

5.3.2 Optimizing fura-2 loading

The loading was performed using the protocol developed in the Herman group [195]. The temperature and incubation time were optimized for the conditions of the current study. Ca^{2+} indicators can become localized within intracellular compartments, closed parts within the cytosol of a eukaryotic cell, usually, surrounded by a single or double lipid layer membrane. In the case of compartmentalization in the organelles, subcellular fluorescence distribution is not homogeneous, and the fluorescence appeared spotty or filamentous and resembled in shapes the intracellular organelles. Compartmentalization of the

indicator within cells can be reduced if the loading temperature is decreased from 37 °C to room temperature [258]. This is more likely mediated through a reduction in endocytosis, a process that will cause the indicator to accumulate in endosomes and topologically related organelles. When reducing the room temperature, the loading period has to be increased. Therefore, a balance of optimum temperature and loading period should be found for each cell type [259]. Homogenous loaded cells were obtained after 45 min incubation at room temperature, while different incubation times between 15 min to 1 hour were tried in the experiments. Bootman and his co-workers [260] also used 1 h incubation at room temperature as the optimum loading condition of fura 2-Am into HeLa cells.) The stained cells were washed two times using HBSS+ (Calcium and Mg-rich Hank`s salt buffer) and were left for 15 min in fresh HBSS+ (inside the chamber) to de-esterify the cell incorporated dye. The buffer was replaced with 400 µl fresh HBSS+, and the measurement was started immediately.

5.3.3 Simultaneous impedance spectroscopy and Ca^{2+} measurement

The response of fura-2 loaded HeLa cells on interdigitated ITO surfaces to 100 µM histamine was explored using the simultaneous impedance spectroscopy and live cell fluorescence microscopy setup. The simultaneously recorded histamine-induced impedance changes and Ca^{2+} flux are shown in Figure 5-2A and 2B. Histamine rapidly promoted a sharp short-lived intracellular Ca^{2+} flux in all fura-2 loaded cells. The Ca^{2+} peak reached a maximum within 60 s and then decreased to a baseline level in a further 490 s. At the same time, histamine caused a rapid dip in impedance that persisted for a few minutes before restoring. Thereafter the

impedance increased over approximately 35 min before returning to a basal level after a further 80 min. Notably, the observed trend of changes in impedance and calcium ion mobilization are in agreement with those in previous studies employing these two techniques separately on gold [261] and glass coverslip [195], respectively. The onset of the impedance alteration was delayed 30 s after intracellular Ca^{2+} change. One important observation from these simultaneous measurements is that the lifetime of the fluorescence response from the Ca^{2+} mobilization correlated with the time of the dip in the impedance signal before restoring to the initial value (Figure 5-2B).

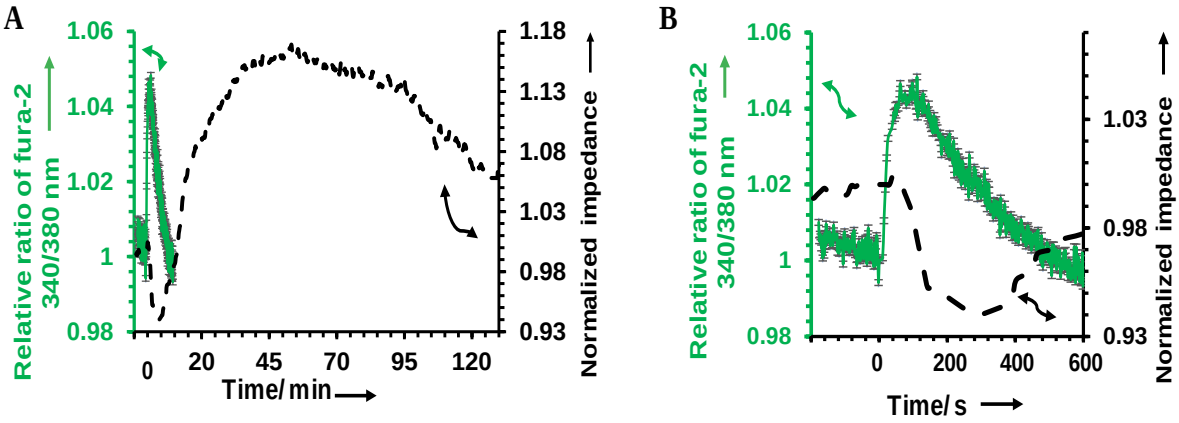

Figure 5-2. (A) The relative histamine-induced change in the fura-2 ratio at 340/380 nm indicates the release of Ca2+ and the simultaneously recorded impedance of HeLa cells plated on interdigitated ITO electrode. The normalized impedance is the impedance of the cell-covered electrode divided by the impedance of the cell-free one (B) An expansion of the impedance and Ca2+ mobilization response for short time intervals from in part A showing the correlation between the fluorescence spike and the decline in the impedance below baseline levels.

An image of an ensemble of fura-2-loaded HeLa cells and time-lapse montages of one of the cells, responding to histamine, as an example, are shown in Figure

5-3. These images show the high fluorescence quality of the surfaces in the setup. Thus, the developed setup allows the monitoring of subcellular and whole-cell responses of ensembles of cells over a wide time scales from milliseconds to hours. Examples of the fura-2 ratio alteration of many individual cells in the ensembles of cells in the field of view over time are shown in Figure 5-4. Results indicated that the cytosolic Ca^{2+} of all fura-2-loaded cells show a rise in response to 100 µM histamine in Hanks' balanced salt solution, which is in agreement with previous reports [262]. The addition of Hanks' balanced salt solution caused no significant changes in either impedance or calcium signals. This result indicated that the obtained responses were purely originated from histamine stimulation.

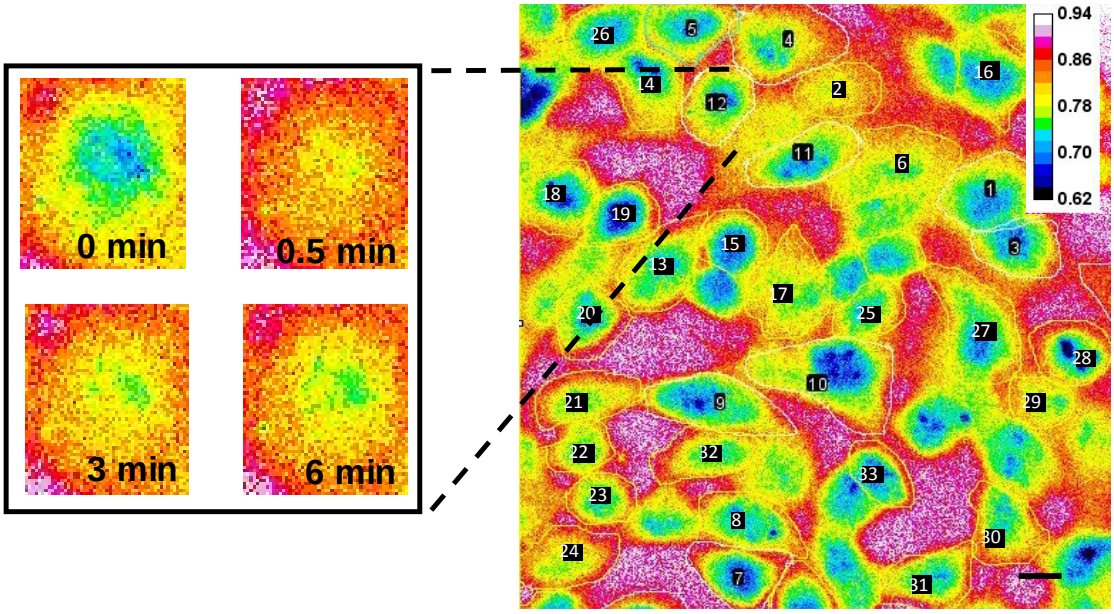

Figure 5-3. A representative of ensemble fura 2-loaded HeLa cells plated on the surface. The ratiometric values of many cells in the field of view was used to calculate the average change in ratiometric value shown in part A. The time-resolved images of one of the cells as an example is shown. Images are pseudocoloured with warmer colours indicating higher ratiometric fluorescence intensity in cells regions. The respective elapsed time after histamine addition is shown.

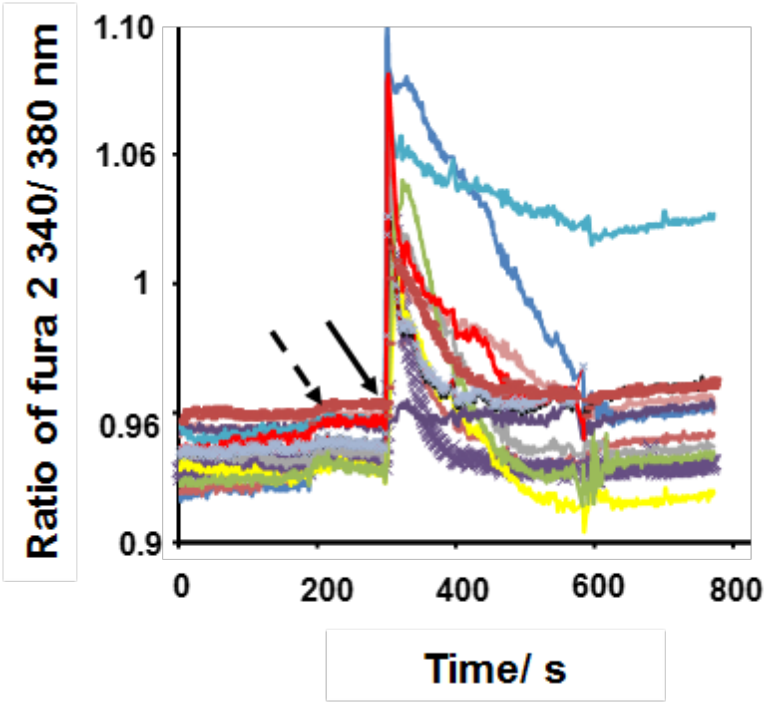

Figure 5-4. Histamine-induced fura-2 ratio change of individual cells on an interdigitated ITO surface. Each curve present the change for one single cell. All fura-2 loaded cells were responsive to 100 µM histamine stimulation. The arrows indicate the time of Hanks' balanced salt solution (dashed arrow) or histamine (solid arrow) addition.

The reported ratiometric values are the average of the ratiometric value of individual cells in the ensembles of cells in the field of view. This value for at one time point was calculated using Fiji software as follow; Opening the movie recorded from ensembles of cells > split channels > extract the frame of the time of interest > draw the rough area around each individual cells, regions of interest (ROI), using “freehand selection” tool > saving these areas using “ROI manager” > Measuring the mean gray value of each ROI of each channel > subtract the background intensity > dividing the aligned emission intensity excited at 340 nm by that at 380 nm pixel by pixel over each manually traced cell region after

subtracting the background fluorescence intensity. The background fluorescence intensity was obtained by calculating the mean gray value of a cell-free area on each frame. The ratiometric value of each individual cell was normalized by diving the fura-2 ratio value with subtracted background data at each time point by the average ratiometric value of that cell during the last 2 minutes before histamine addition again after subtracted background value.

The time-resolution ratiometric images of an individual cell were extracted from the created ratiometric movie as follow; Drawing the ROI around of the cells in the ratiometric movie> Image> Stacks> Tools> Make Substacks. Then, the ratiometric movie of the single cell was created by software. The frames related to the time point of interest were extracted from the movie. The false color images were created using the “Lookup Tables” in the “Image” tab of Fiji software.

5.3.4 Modeling the impedance of the cell layer

Frequency-resolved impedance reading (40000-400 Hz) at different time points before and after adding histamine was subjected to the mathematical model of Giaever and Keese [147]. The detail of this modelling strategy has been explained in chapter 1.Figure 5 illustrates the frequency resolved impedance spectra of interdigitated ITO surface without cells and with cells. The impedance value calculated from the mathematical model were used to obtain the values of α and R_b, before and 25 min after histamine addition. These values for R_b changed from $1.806 \pm 0.10\ \Omega.cm^2$ to $2.13 \pm 0.12\ \Omega.cm^2$ and for α from $1.678 \pm 0.04\ \Omega^{1/2}$.cm to $1.719 \pm 0.05\ \Omega^{1/2}$.cm before and 25 min after histamine addition. In the current

study, any huge change in cell radius was not observable using microscopy and if such a huge change of cell radius was the driver of change in α value, the restoration of the impedance would take a long time (hours) to recover to the basal level. With the average cell radius of 10.2 ± 2.1 μm, calculated by measuring the area of more than 19 cells, and ρ of 54 Ω.cm at 37 °C, the value of h was calculated to change from 199.5 ± 8.7 nm to 190.0 ± 9.2 nm after 25 min of exposure to histamine.

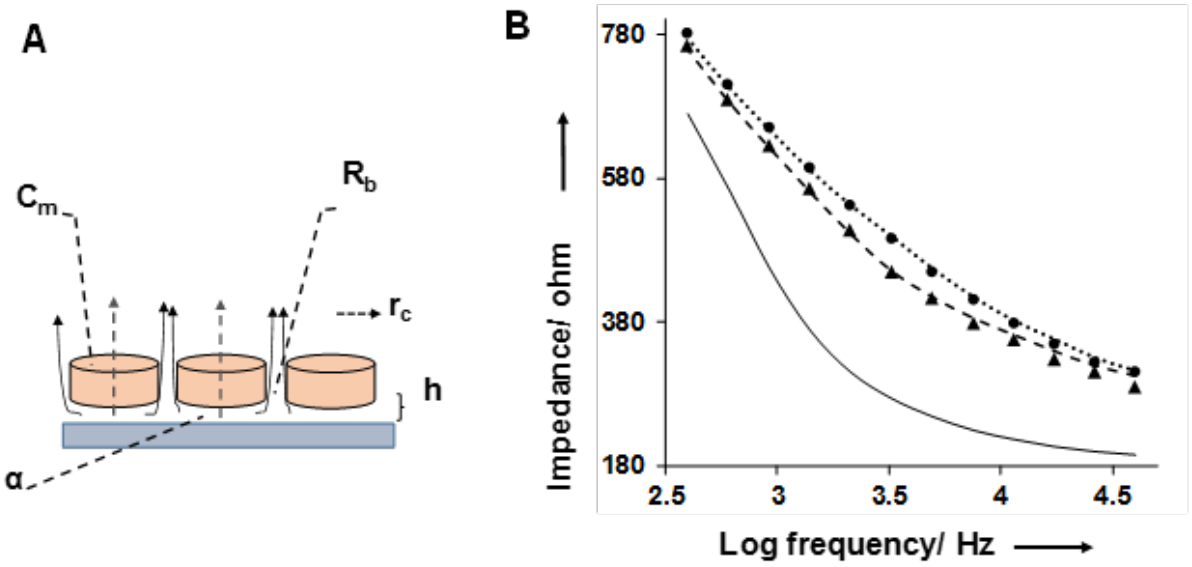

Figure 5-5. (A) A mathematical model developed by the Giaever group was used to fit the frequency resolved impedance data to calculate the values of α, representing the contribution of cell-surface connection, R_b, showing the role of cell-cell strength in define the impedance value, and C_m, the cell capacitance. The model also can be used to extract the morphological information of cells. r_c represents the average cell radius and h is the average distance between the ventral cell membrane and the surface. (B) An example of frequency resolved impedance data of a cell-free interdigitated ITO and the experimental (lines) and fitted (scattered dots) data of the cell-covered electrode before (dashed line and scattered triangles) and 25 min (dotted line and scattered circles) after histamine addition.

Fitting of the model to experimental data enables the determination of the contribution of the cell-cell and cell-substrate interactions to the experimentally

measured impedance (Figure 5-6). The percentage of change in each parameter with respect to its value before the addition of histamine has been expressed as a relative change.The results showed that the immediate decrease in experimental impedance was mainly caused by the decrease in cell-cell resistance ($t < 4$ min). These findings are in agreement with studies on endothelial cells suggesting that histamine targets E-cadherins, and consequently, decreases cell-cell connectivity [34]. Cadherins are Ca^{2+}-dependent transmembrane proteins. In addition, the change in cell-cell resistance is in parallel with the change in overall impedance (~ 40 min). Phase contrast images of cells were recorded before and after histamine addition in an attempt to visualize the change in cell-cell distances using the setup (Figure 5-6B). The arrows on the images show locations where the short-time increase and long-term decrease in cell-cell distances in response to histamine are observable.

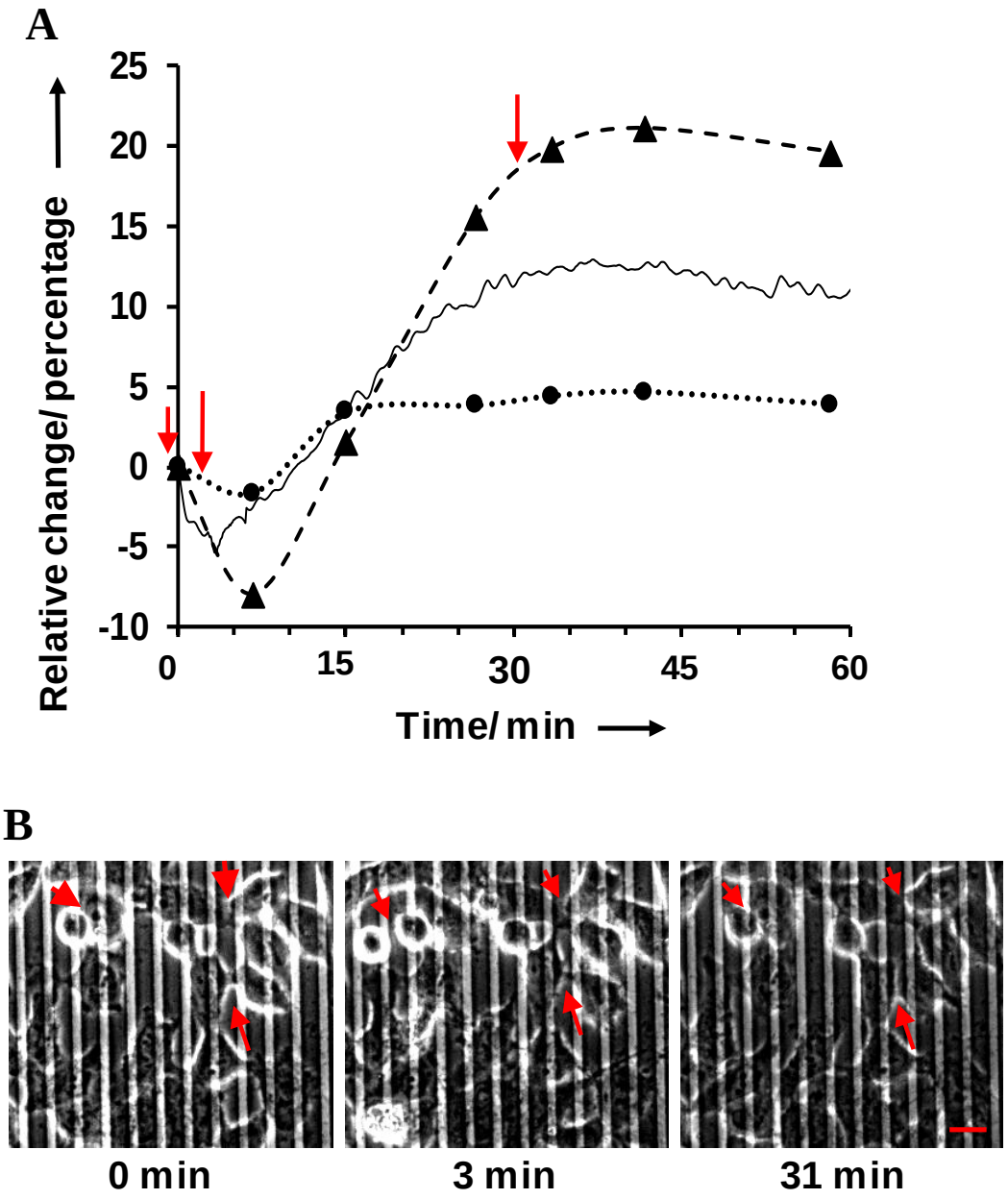

Figure 5-6. (A) The experimental impedance spectroscopy was modeled and deconvoluted to estimate cell-cell (dashed line) and cell-substrate (dotted line) resistance and is shown along with the experimental impedance at 4 kHz (solid line). (B) Representative time-lapse montages of HeLa cells before addition of histamine, 3 min and 30 min after histamine stimulation captured using phase contrast microscopy performed simultaneously with impedance measurement shown in part D[1]. The arrows

[1] The resolution of the phase contrast images have been affected by the thickness of the electrodes.

in part D indicate the times that phase contrast images were taken and on the images point to locations with observable changes in cell-cell contacts. Scale bar is 20 μm.

5.3.5 Surface modification characterization

The ability to screen live cells in a physiologically relevant context is crucial to acquire reliable information for drug discovery and development. Therefore, surface chemists have been motivated to engineer substrates to provide a defined expression of immobilized ligands [15]. Currently, seldom has the effect of surface chemistry been connected with biological functions of cellular targets in response to soluble cues.

Interdigitated ITO surfaces were modified with different average RGD spacing to assess any possible impact of cell adhesive ligand spacing on histamine-induced cellular responses (Schematic 5-2). The modification strategy and characterization of the surface are outlined in detail in chapter 2. In brief, a plasma cleaned interdigitated ITO surface was modified with 16-phosphohexadecanoic acid self-assembled monolayers followed by coupling to different ratios of 1-aminohexa(ethylene oxide) to 1-aminohexa(ethylene oxide) monomethyl ether molecules. The distal hydroxyl on the 1-aminohexa(ethylene oxide) was then activated to which the GRGDS adhesive ligands were attached. The RGD spacing on the surfaces was tuned by adjusting the ratio of the two ethylene oxide-based molecules.

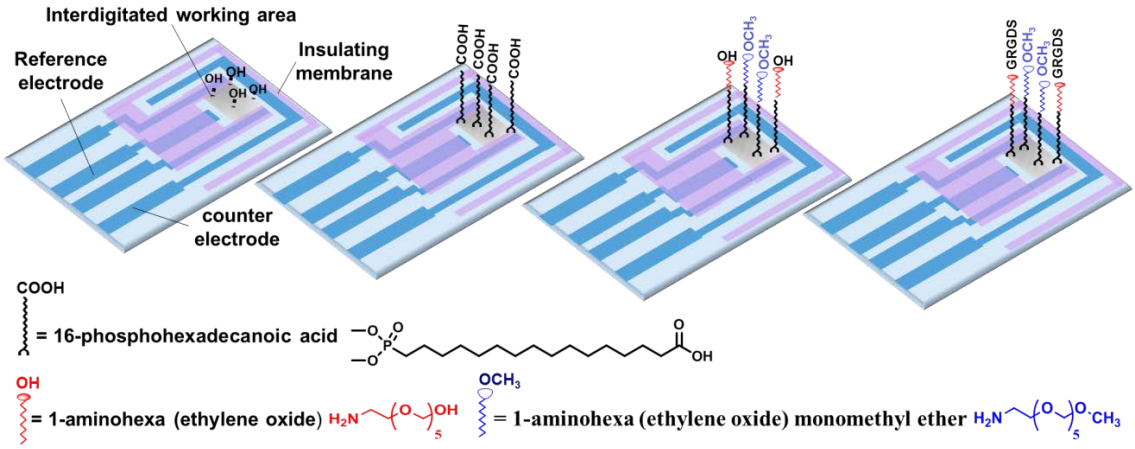

Schematic 5-2**.** Interdigitated ITO area was modified using 16-phosphohexadecanoic acid followed by attaching to various ratios of 1-aminohexa(ethylene oxide) monomethyl ether to 1-aminohexa(ethylene oxide). Further coupling of controlled amount of GRGDS cell adhesive ligands was achieved with the hydroxyl, and not to the methoxy-terminated species.

5.3.6 Simultaneous histamine-induced calcium ion release and impedance change on surfaces with different RGD densities

Simultaneous measurements revealed that histamine stimulation of cells on surfaces with average RGD spacing of 1 or 31 nm led to cytosolic Ca^{2+} release (Figure 5-7A) and impedance changes (Figure 5-7B) over shorter durations of time compared with cells compared with surfaces with 968 or 30957 nm average ligand spatial distribution. The duration of Ca^{2+} was calculated based on the time that Ca^{2+} signal takes to reach a plateau. In addition, the results indicated that the magnitude of the histamine-induced Ca^{2+} flux (Figure 5-7C) and impedance response (Figure 5-7D) were also sensitive to the spatial expression of RGD adhesive ligands. The summarized average variations in the percentage of the fura-2 ratio (Figure 5-7C) were calculated by subtracting the average ratiometric

values at the beginning of the experiment from the maximal ratiometric values after histamine addition [263].

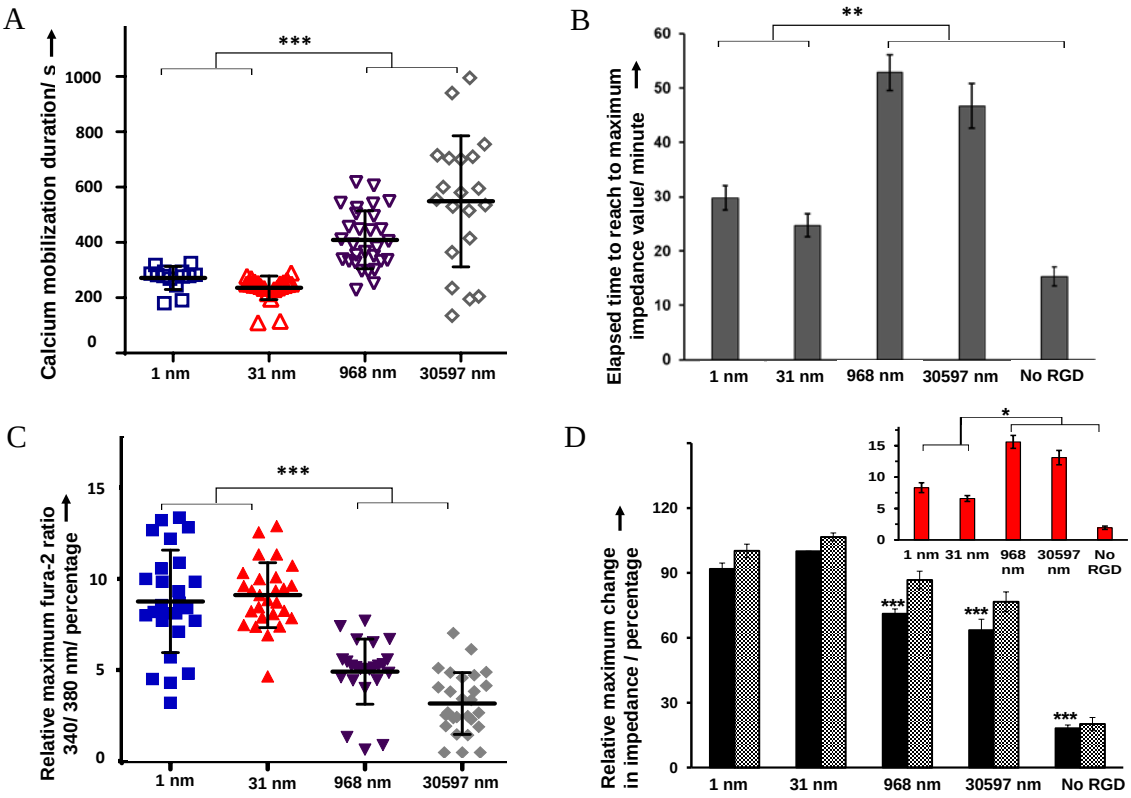

Figure 5-7. Simultaneous histamine-induced impedance and calcium ion release measurements of HeLa cells plated on interdigitated ITO surfaces with different average RGD spacing. (A) The Ca^{2+} duration. (B) The time to maximal impedance response (C) The maximum normalized ratio of fura-2 ratiometric value obtained by dividing the fluorescence intensity measured with excitation at 340 nm to that at 380 nm for cells. The data are integrated over the ratiometric data of individual cells in the ensemble of cells at the time of maximum response divided by the respective ratiometric value of each cell before histamine addition, n ≥19. (D) The value of maximum impedance response of cells before (black bars) and after (grey bars) histamine addition normalized to the impedance values of cell-free electrodes. The inset is the difference between the impedance value before and after histamine addition. For statistics, 1 way ANOVA, comparing all sets of data with data of surface with average 31 nm RGD spacing. *p < 0.05 relative to surfaces with 31 nm average RGD spacing wherever it is not specified.

Histamine promoted a higher Ca^{2+} response in cells plated on the surfaces with RGD spacing of 1 or 31 nm than surfaces with average RGD spacing of 968 or

30,957 nm. Examples of Ca^{2+} response and impedance signals of the cells on surfaces with different RGD densities are shown in Figure 5-8 and Figure 5-9. For cells on surfaces with 1 or 31 nm average ligand spacing, there was a lower relative increase in impedance values upon histamine addition compared with cells on surfaces with average RGD spacing of 968 or 30,597 nm (Figure 5-7D). These smaller impedance increases are attributed to the more robust cell adhesion to these surfaces and to neighboring cells before stimulation than the surfaces with higher ligand coverage. Higher baseline impedance level (Figure 5-7D) of plated cells confirmed greater cell adhesions to the surfaces with 1 nm or 31 nm average ligand spacing compared with the surfaces with 968 or 30,597 nm average ligand spatial distributions. This is physiologically relevant as the RGD spacing smaller than 70 nm mimics the similar periodic spacing of RGD to that found in fibronectin and collagen which provide strong cell adhesion points [80].

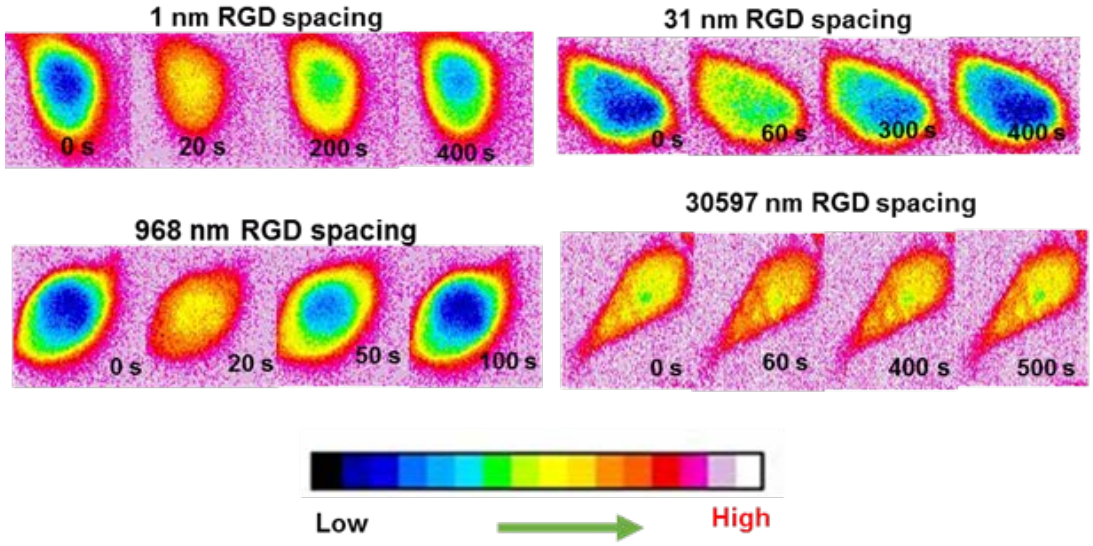

Figure 5-8. Examples of simultaneously recorded time-lapse montages of a fura-2-loaded single HeLa cells on surfaces with different average RGD spacing (The spacing is shown on top of each series of images). The elapsed time written on each image refer to the duration after histamine addition. Pseudocolor calibration bar indicates that warmer colours (e.g., orange, red) attribute with higher concentrations of intracellular calcium cells regions.

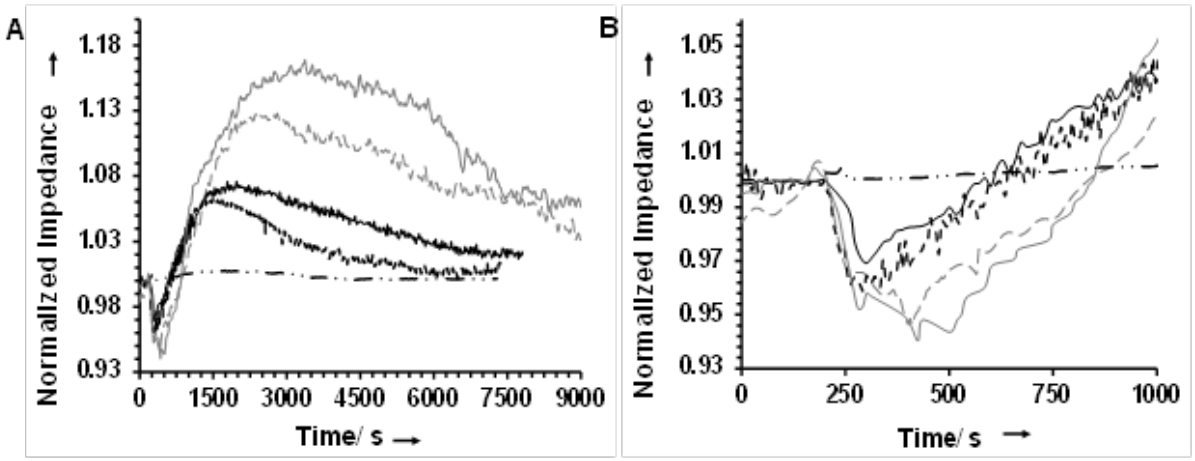

Figure 5-9. (A) Simultaneously recorded real-time normalized histamine-induced impedance on surfaces with various RGD spacing of 1 nm (black solid line), 31 nm (black dashed line), 968 nm (grey solid line) and 30597 nm (grey dashed line) and the surface with no RGD (black dash-dotted line) (B) Magnified time course of normalized impedance as is shown in part A. The impedance of a cell-covered electrode was divided by the respective impedance of the cell-free electrode, to obtain normalized impedance value on each surface.

5.3.7 The behavior of the cells on the surface modified with only 1-aminohexa(ethylene oxide) monomethyl ether molecules

Cells on inert surfaces, surfaces modified with 1-aminohexa(ethylene oxide) monomethyl ether in the absence of 1-aminohexa(ethylene oxide) such that no RGD ligands were attached, did not show any reproducible histamine-induced Ca^{2+} response. Cells on this surface did display a slight change (less than 1%) in impedance signal with no initial immediate decrease upon histamine stimulation. This is because a limited number of cells adhered to this surface and rarely any mature cell-cell contacts formed (Figure 5-10). This result further supports the idea that a decrease in cell-cell adhesion dominantly drives the histamine-induced immediate decrease in impedance value as was concluded from the modeling results. This surface is acting as an inert surface with the minimum ability of cell attachment and adhesion although a high density of cells (1.5×10^5 cells/ cm^2) has been plated on the surface for 3.5 h. The disappearing of the temporary rapid decrease in impedance that was observed for cells on other studied surfaces is in agreement with the idea that reduction in cell-cell adhesion precedes the immediate histamine-induced reduction in impedance value.

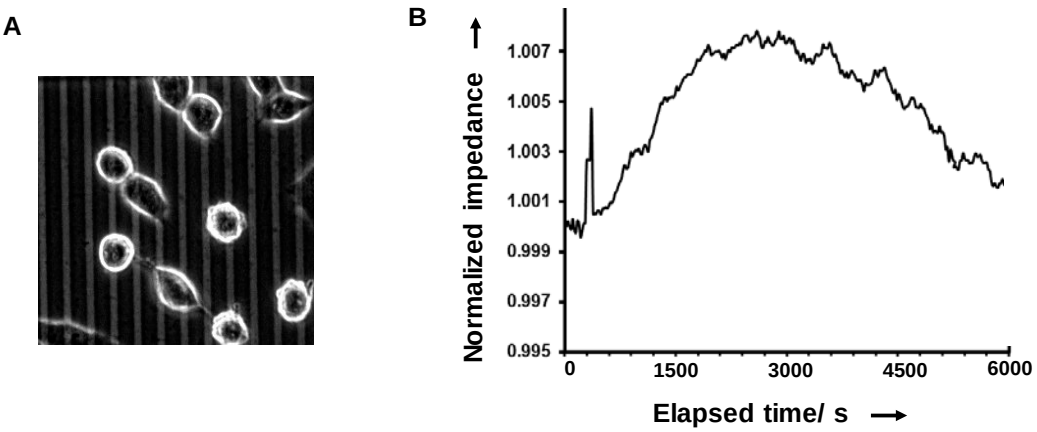

Figure 5-10. (A) A phase contrast image of cells on surface modified with only 1-aminohexa(ethylene oxide) monomethyl ether molecules (No RGD) after 3.5 h of plating and before fura-2 dye loading procedure. (B) Histamine-induced impedance alteration of cells on this surface. This peak displayed a weakly visible change (less than 1%) with no initial immediate decrease. This data further support the idea that reduction in cell-cell adhesion precedes the immediate histamine-induced decrease in impedance value.

The results confirmed the sensitivity of cell responses to the model drug to cell-surface interactions. It is speculated that among the possible factors that may have participated in regulating agonist-induced Ca^{2+} mobilization, the morphological state of cells has played an essential role. It has been demonstrated by the Gooding group that cell morphology is regulated on ITO surfaces with various RGD spacing [238]. It has been shown that the interruption in the cytoskeleton arrangement which is in direct relation to cell morphology contributes to modulating the release of Ca^{2+} through the formation of signalling complexes that alter the efficiency of the relevant signalling transductions [264, 265]. However, this is incredibly complicated as cytoskeleton and Ca^{2+} mobilization cross talk in a bi-directional manner. It is shown that the rearrangement of cellular actin is Ca^{2+} dependent [266] and essential for inducing an impedance change.

Therefore the modulated Ca^{2+} elevation can be a reason behind the regulated duration of impedance change on surfaces with various cell adhesive ligand densities. Recently, The Gooding group has demonstrated [81] that cells on a silicon wafer with average RGD spacing of 44 nm display highly ordered focal adhesions and, consequently, the greatest signal transduction efficiency. Interestingly, herein, the minimum duration of histamine-induced impedance alteration was found to correlate well with the shortest duration of Ca^{2+} elevation on interdigitated ITO surfaces with 31 nm average RGD spacing. The cells on this surface displayed the maximal amplitude of histamine-induced Ca^{2+} release.

5.4 SUMMARY

These findings are biologically significant since they imply that specific adhesive ligand spacing induces synergy between adhesive ligand integrins and mediators of GPCRs activity that critically determine the cell behavior. Thus, controlling the surface chemistry is critical to avoid misleading information on cellular responses during drug testing. Developing the screening tools similar to the simultaneous methodology that was presented here provides the ability of real-time analysis of cellular responses at sub-cellular and whole-cell levels on an interdigitated ITO surface that was designed to mimic the native cellular environment. In summary, a novel approach that combines two powerful techniques for examining the cell responses was developed; live fluorescence microscopy and impedance spectroscopy, simultaneously. This coupling offers a more in-depth view of cellular responses to soluble cues in the presence of

physical attributes of adhesive cues with different time scales. This methodology provides a more comprehensive and reliable evaluation of drug *in vitro*.

CHAPTER 6 REAL-TIME SCREENING OF POTENTIAL ANTIFIBROTIC COMPOUNDS ON LIVE CELLS USING A BIOELECTROCHEMICAL ASSAY

6.1 INTRODUCTION

Scarring happens as the last phase of the normal physiological tissue response to wounding. However, if scarring perpetuates in pathological cases, fibrosis may occur and cause the loss of tissue function and even death. Fibrosis is a major global health burden [267] accompanying with deregulated cell morphology, migration, differentiation and function [268] . The fibrotic condition is histologically characterized by the excessive production of extracellular matrix (ECM) components such as collagen [269]. Different parts of the body such as lung, liver, skin, joints, and tendons can be afflicted by fibrosis disorder. For instance, the fibrotic condition in palms, called Dupuytren`s, is associated with permanent flexion contracture of digits, which is often painless but severe and debilitating to hand function [270]. Apart from pathological effects, millions of patients develop multiple long-term fibrotic sequelae such as depression and sleep disorders that severely hinder their quality of life [271]. Currently, the excision of the palmar aponeurosis, in the form of fasciectomy is the most common therapy for Dupuytren`s contracture. In fact, there is no potent chemical compound available as a cure for the different type of fibrosis [272]. Due to the surgery complications [273, 274] and the high recurrence rate [275], there is an unmet need to develop drug therapies.

The development of efficient therapeutical antifibrosis agents has been hampered partly due to the lack of appropriate methodologies for the *in vitro* evaluation of

these compounds prior to introducing the agents to animal models [276]. Currently, most of the devices in this area monitor the amount of deposited collagen to detect the effect of the potential antifibrotic compounds. One of the biological challenges in this regard is that cells do not lay down enough collagen over a useful time scale *in vitro* for screening with either monolayer cultures or 3D scaffolds. Recently, Raghunath group [272] has introduced efficient strategies to accelerate and enhance collagen deposition *in vitro*. In this method, specific biomolecules are added to the culture medium (crowded media) to speed up the fibrosis progress from several weeks to a few days, similar to what occur in body condition. The detection in these methods involves fixing and staining of collagen fibres and measure the collagen area compared with control samples. The enhanced collagen production process combined with fluorescence microscopy analyses is called “Scar-in-a-Jar” [277]. As the “Scar-in-a-Jar” method requires cell fixation and staining, it is essentially an end-point assay. A desirable extension of this technique would be to develop methods that are amenable of assessing fibrosis on the same cells as it progresses. Thus, evaluating of fibrosis in live cells for long-term, without interrupting cells normal function, is important to provide a more robust assay that can provide information on the dynamics of drug responses as well as their end result [278-280].

Electrochemical impedance bioassays can detect minute changes in cell morphology and cells-cells or cells-substratum connectivity as well as the alteration in media resistance in real-time [173, 281]. Thus, these techniques have

the capability to assess the disease or therapies that interrupt with cell shape and adhesion in long-term in a label-free manner. During fibrosis, quiescent fibroblasts differentiate to fibrotic myofibroblasts associated with alteration of cell morphology and adhesion [268]. Thus, the hypothesis was that bioimpedance measurements may display sensitivity to fibrosis progress. In this regard, the feasibility of screening of potential anti-fibrotic compounds using electrochemical bioimpedance measurements is worthy of assessment to provide a real-time “Scar-in-ajar” inspired biosensor. However, correlating the acquired raw impedance data to subcellular events is challenging. Therefore, a desirable cell-based electrochemical impedance biosensor that provides the possibility of also performing light microscopy would greatly aid in the acquiring of information on intracellular changes that occur during the screening of newly developed antifibrotic molecules.

Herein, the feasibility of using cell-based electrochemical impedance measurements in determining the efficacy of potential antifibrotic chemical agents was assessed by culturing the fibrogenic cells on interdigitated ITO electrodes. The assay was used to examine the effect of an analogue of mannose-6-phosphate (M6P), namely PXS64, on inhibiting the progress of fibrosis of cells collected from the palms of patients with Dupuytren`s disease. During the entire experiment, fibrosis was modelled *in vitro* by culturing fibrotic cells under the experimental condition developed as part of the “Scar-in-a-Jar” methodology. Owing to the non-invasive nature of the employed electrochemical method, and

the transparency of the electrodes, the cell area, the amount of collagen per cell, collagen fibrils alignment, and the level of cytosolic Ca^{2+} was measured using fluorescence microscopy after finding the useful time window of the drug. In addition, the fluorescence-based analyses were used to confirm the validity of the results of the bioelectrochemical impedance assay on the efficacy of the examined antifibrotic chemical compound. The principle of impedance measurement combined with the "Scar-in-a-Jar" is shown in Schematic 6-1.

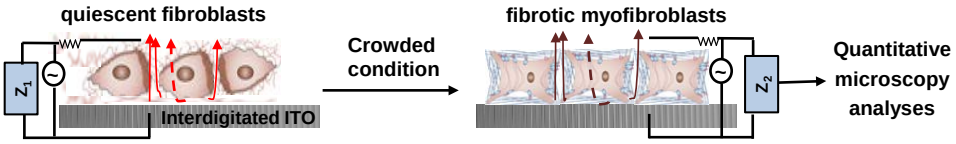

Schematic 6-1.The electrochemical impedance values of the cell layer before (Z_1) and after (Z_2) fibrosis may display different values due to the change in morphology and adhesion of cells. Fibrosis is involved with the transition of fibrogenic cells from quiescent fibroblasts collected from patients to fibrotic myofibroblasts. The fibrosis disease is modelled *in vitro* using the crowded media as part of the "Scar-in-a-Jar" strategy. Impedance measurement aims at determining the efficient time window of the examined chemical compound in a rapid and non-destructive manner prior to performing optical analyses on the same cells to provide quantitative information at on detail intracellular events.

6.2 EXPERIMENTAL SECTION

6.2.1 Preparing media

Three different media were prepared; non-crowed, crowded, and PXS64-containg crowded media. The crowded media contains molecules that stimulate cells to produce enhanced amount of collagen in shorter period of time.The crowded model the scar-like tissue *in vitro* according to "Scar-in-a-Jar" method [277]. This media contains 0.5 % FBS, a mixture of 37.5 mg/mL Ficoll PM70

(Fc 70) with 25 mg/mL Ficoll PM 400 (Fc 400), 100 mM of l-ascorbic acid 2-phosphate and 5 ng/mL-1 TGF-β_1 (5 ng/ml). 2-Phosphate hexahydrate is a stable form of ascorbate with a longer lifetime than ascorbate in culture [282]. The neutral macromolecules in a Ficoll cocktail (Fc) increases collagen deposition 10-fold in 6 days and in a reticular deposition pattern [277]. PXS64-containing crowded condition refers to the crowded media with 10 µM dissolved PXS64. The non-crowded state (control media) represents to DMEM that containing l-ascorbic acid 2-phosphate, penicillin-streptomycin and 0.5% FBS.

6.2.2 Primary cell culture

Human primary Dupuytren`s cells were collected from palms of the patients with Dupuytren`s disease under University of Western Australia ethics approval and with informed consent from all patients in accordance with the NHMRC national statement on ethical conduct in human research. The primary cells were cultured as described in 2.4.3. 50000 Cells/cm^2 were cultured for 24 h on surfaces in normal DMEM-glutamax media with 10% FBS and 1% penicillin/streptomycin and then the media was changed to one of the non-crowded (control), crowded (no drug) or 10 µM PXS64-containing crowded culture

6.2.3 Electrochemical impedance spectroscopy

The cell-covered interdigitated ITO surfaces were probed with a weak non-invasive sinusoidal AC signal within the range of frequency between 40000-400 Hz (10 mV) (12 points/decade) as is described in Chapter 2, § 2.5.1. This current applies only a negligible electrical stimulation to cells during the impedance

measurement and, therefore, do not electrically stimulate them. The electrodes were washed two times with the electrolyte (cell media) before cell seeding. The resulting electric potential was measured 24 h after cell seeding across the cell-covered electrode to acquire the baseline impedance spectra. The experimental impedance spectra of the cell layers on the surfaces under different conditions were recorded daily. The measurements continued until the fibrosis occurred and then the effect of the drug became evident. The impedance value on each surface was normalized by dividing the impedance of cell-covered electrode at each time point by the impedance value of the cell layers obtained 24 h after seeding cells, before applying different experimental conditions. The cell-covered surfaces were then used for further optical analyses after finding the effective time window of PXS64 for Dupuytren`s cells.

6.2.4 Cell area measurement

A measure of Dupuytren`s morphology and cells area was performed after impedance measurements. To this end, cells were fixed and stained with Alexa Fluor® 647 phalloidin. Alexa Fluor® 647-phalloidin stain the cell cytoskeleton through the binding of phalloidin to F-actin. Chapter 2, § 2.4.4 describes the fixing and staining processes. The fluorescence images were recorded using a total internal reflection fluorescence (TIRF) microscope (ELYRA, Zeiss) equipped with a cooled, electron-multiplying charge-coupled device camera (iXon DU-897; Andor) with an exposure time of 30 ms. A 20x air objective lens and 15 mW of 633 nm laser illumination were used for imaging. Raw

fluorescence intensity images were analyzed using image-analysis software platform ImageJ (US National Institutes of Health).

6.2.5 Immunocytochemistry for collagen visualization according to "Scar-in-a-Jar" method

Cells were exposed to one of the non-crowded, crowded (no drug), or 10 µM PXS64-containing crowded conditions for the time window that was indicated using impedance measurements. Then, cells were washed with PBS and were blocked with 3% bovine serum albumin (BSA) in Fluorobrite for 10 min. Then the immunocytochemistry assay was performed using primary and secondary antibody solution according to Chapter 2, § 2.4.6. The nuclei of cells also were stained to count the number of cells on the surface using Hoechst® staining solution as Chpter2, § 2.4.4 explains.

The coverslips were mounted on the slides using Prolong® Gold anti-fade mounting solution (Life technologies, USA). Nail polish was used to fix the coverslips, and the slides were stored in a light-proof box at 4°C until imaging for quantifying the amount of collagen per cell or for coherency analysis.

6.2.6 Coherence analysis

The alignment of collagen fibres deposited by cells cultured in crowded, non-crowded and PXS64-containing crowded media was calculated by analysing the confocal images of stained collagen and nuclei using the orientation J plugin of Fiji software and the orientation J package as has been outlined in detail in

Chapter 2, § 2.4.7. The coherence value from 0 to 1 described the collagen fibres with lowest to highest oriented structure, respectively.

6.2.7 Ca^{2+} flux measurement

The amount of intracellular Ca^{2+} flux in cells was measured after exposing cells to one of the non-crowded, crowded or PXS64-containing crowded culture media for the time window that was determined by impedance results. The measurement was performed after loading cells with fura-2 AM. Fluorescence at 340 nm/380 nm excitation and 510 nm emission were recorded on an inverted Nikon TE2000-U microscope at 1 min intervals with an exposure time of 50 ms using a Hamamatsu Orca ER digital camera at 37 °C. The ratiometric 340 nm/380 nm signals of individual cells were quantified using Metamorph 6.3 to measure signal intensity of manually traced cell regions. A cell-free equivalent region was used to measure the background intensity. The background value was subtracted from the value that was obtained from cell areas. Based on the observed results for cells exposed to different media for the duration that was indicated based on impedance measurement, it was decided to check the intracellular calcium ion concentration of Dupuytren`s cells at different time points. Cells were seeded on the surfaces for 24 h first, then the intracellular Ca^{2+} was measured immediately after changing media (0 h), after 24 h, after 48 h or after 72 h of treating cells in one of the non-crowded, crowded (no drug), or 10 µM PXS64-containing culture media. For acute measurement (0 h), the intracellular calcium ion level of the cells loaded with fura-2 AM was measured 5 min just before and 10 min after

changing the experimental condition. For long term measurements (≥24 h), the media was changed to one of the relevant ones and at specific time points the fura-2 was loaded, and the intracellular Ca^{2+} flux was measured for cells under various experimental conditions. To study whether the calcium flux is mobilized from endoplasmic reticulum stores, thapsigargin was used [283]. For this purpose, 10 nM thapsigargin was added to cells that were exposed to the crowded media for 48 h and the cytosolic calcium ion level was then measured after another 24 h.

6.3 RESULTS AND DISCUSSION

The "Scar-in-a-jar" model uses TGF-β to enhance collagen deposition in an accelerated manner. In this study, such a condition noted as "crowded media". Crowded condition describes the environment that induces a scar-like state. Macromolecules in the crowded media drive reaction partners into closer collaboration resulting in improved protein folding and protein-protein interactions [277]. The absence of crowding molecule (TGF-β) hinders the fibrosis progress [284]. This condition was named "non-crowded", where fibrosis progress is expected to impede compared with the cells exposed to the crowded media. The effect of PXS64 was examined by culturing cells in the crowded environment in the presence of 10 µM PXS64. This concentration was selected according to a recent study conducted by Iyer and co-workers [285, 286] to control the fibrosis of fibroblast cells. It is desirable that the potential antifibrotic

compounds in crowded media keep the state of cells as close as possible to those under the “non-crowded” condition. The experimental conditions have been summarized in Table 6-1.

Table 6-1. Summary of the experimental conditions

Condition	Non-crowded	Crowded	Drug-containing crowded
TGF-β1 (5 ng/ml)	-	+	+
PXS64 (10 µM)	-	-	+

6.3.1 Impedance measurement

Impedance spectroscopy on interdigitated ITO surfaces was employed to assess the status of cells. For this purpose, the media was changed to the crowded, 10 µM PXS64-containg crowded, or non-crowded media after 24 h of seeding cells. The frequency-resolved impedance readings were performed at 12 frequencies spaced evenly on the logarithmic scale ranging from 40000 Hz to 400 Hz were recorded at each time point. The impedance measurement was carried out at different time points until significance differences between the impedance values of cells in drug-containing condition were observed compared with those under the crowded state. The impedance values of the cells before changing the experimental conditions were similar. These data displayed significantly higher value for cells under crowded condition compared with cells in non-crowded or PXS64-containing crowded media after 48 h of exposure. The example of frequency-resolved impedance data shown in Figure 6-1A demonstrates that the impedance changes were at a maximum at 40000 Hz. The electrical current

mainly passes between the ventral surface of the cell membrane and the electrode and cell membrane rather than through cell junctions at high frequencies (f > 10000 HZ) [157]. Therefore, at these frequencies, the impedance is dominated by the resistance through the cell and therefore mainly depends on cell coverage, the cell-electrode gap (cell cleft) and the electrolyte resistance [156, 287].

The normalized impedance values at the frequency of 40000 Hz after immediate (0 h), 24 h, 48 h, and 72 h after changing the normal media to one of the experimental conditions are shown in the Figure 6-1B. The time-resolved impedance values after exposing cells to different conditions were divided by the impedance value of the cell-free electrodes to obtain the normalized data. This normalization removes the contribution of the electrode-electrolyte combination and parasitic elements [288]. Therefore, the change in impedance values was attributed to the alteration in cellular properties induced by applying different experimental conditions. The impedance of the cells under the crowded condition displayed a greater increase over time compared with cells cultured in the non-crowded environment. The magnitude of the impedance of cells under crowded condition after 48 h displayed a significant difference compared with cells in the crowded media containing 10 μM PXS64 and this effect persists in the next 24 h. The impedance of the cell-covered electrodes cultured in 10 μM PXS64-containing crowded culture media displayed similar values to those in the non-crowded one. These results indicated the efficacy of PXS64 in neutralizing the effect of the crowded condition that stimulated fibrosis in 72 h. Next, the validity

of the results on the influence of PXS64 using electrochemical impedance measurement was assessed using fluorescence measurements on the cells after 72 h culturing under the different experimental condition and running electrochemical measurements.

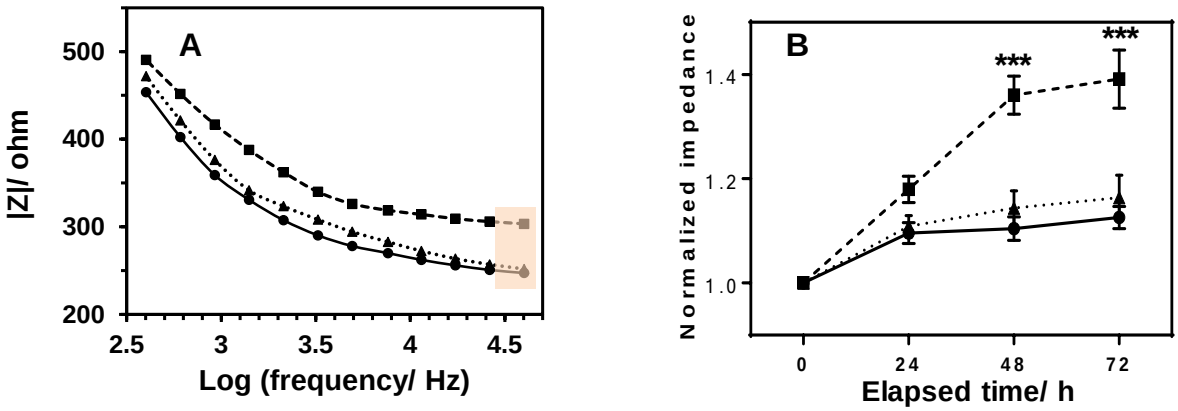

Figure 6-1. Measure the effect of PXS64 on Dupuytren`s cells in non-crowded (solid curve), crowded (dashed curve), or 10 µM PXS64-containing crowded media (dotted curve). (A) The impedance measurement at 12 frequencies in the range of 40000 Hz-400 Hz after 72 h exposing cells to the various media. The frequency of 40000 Hz showed the broadest range of relative change for cells as has been highlighted. The impedance values at this frequency were reported for further comparisons. (B) The effect of PXS64 on Dupuytren`s cells at different time points by tracking the real-time change in impedance of the cell layers at 40000 Hz. The impedance of the cells under the crowded condition showed a significant increase compared with the cells cultured in PXS64-containing crowded media. This indicated the efficacy of the drug in inhibiting the fibrosis progress in the crowded state. The elapsed time shows the time after changing the normal media of cells into one of the experimental conditions. *** is $p < 0.001$ versus non-crowded condition.

6.3.2 Cell area measurement

Evaluation of the cell area and shape was performed by staining the cytoskeleton to obtain the quantitive information on the effect of PXS64 as an antifibrotic chemical on cellular behaviour. The fluorescence microscopy was also used to

correlate the conclusions made with the electrochemical impedance measurement with cell morphology changes. It has been demonstrated that cell morphology and spreading are downstream events that undergo regulation in fibrosis. Therefore, cells on the electrodes treated under different experimental conditions were fixed and stained with Alexa Fluor® 647 phalloidin (Figure 6-2). The results showed that cells under crowded condition displayed dendritic morphology, whereas, cells in non-crowded media mainly exhibited the stellate shape. Furthermore, the results illustrated that the presence of 10 µM PXS64 recovered the cell morphology back to stellate. The average area occupied per cell were calculated based on obtained fluorescence images (Figure 6-2D). Cells under crowded media displayed a significantly higher average area per cell than cells exposed to PXS64-containing crowded media. Moreover, the results showed that cells under the crowded condition in the presence of 10 µM PXS64, exhibited similar morphology and spreading behaviour to cells cultured under non-crowded condition.

These results demonstrated that cells under crowded condition became well-spread, indicating they were well-adhered with prominent focal adhesions. This morphological study showed that the crowded condition accelerated the fibrosis in Dupuytren`s cells *in vitro* compared with same cells under non-crowded condition. The cell area and shape of cells in PXS64-containing crowded media remained similar to cells treated under the non-crowded state. In agreement with impedance results, the fluorescence results indicated the capability of PXS64 to

inhibit the effect of crowded condition in developing fibrosis. This change in cell morphology occurs by inducing the polymerization of the actin cytoskeleton from globular to filamentous [289, 290]. Actin polymerization is necessary for impedance alteration [57]. The increased cell coverage limits the bare area of electrode surface exposed to the electrolyte and thus the current leakage [156]. These data in addition to providing the quantitative measure of average area per cell indicated that the observed increase in impedance value over time of cells under crowded media could be related to changes in cell spreading and shape.

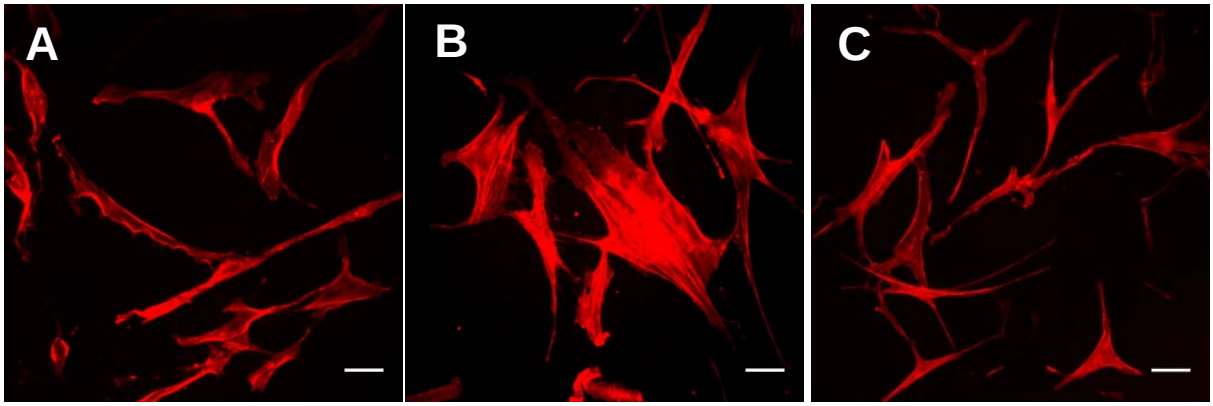

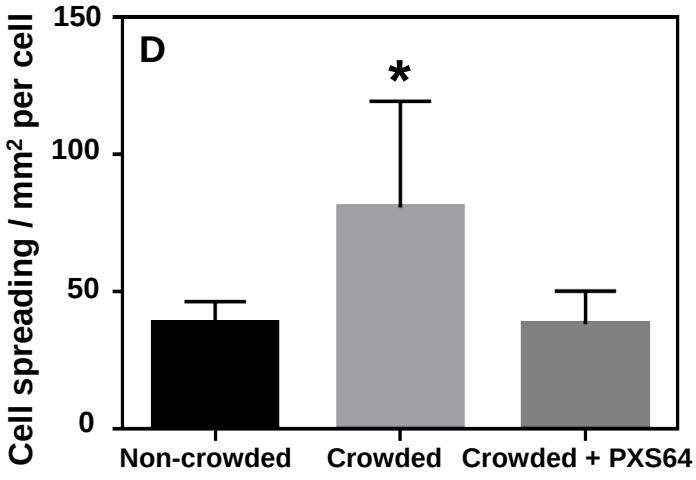

Figure 6-2. A measure of Dupuytren`s cells morphology and area post Alexa Fluor® 647 phalloidin staining. Epifluorescent images of cells in (A) non-crowded, (B) crowded (no drug) or (C)10 µM PXS64-containing crowded media for 72 h. Considerable alterations in cell morphology under crowded condition were observed compared with cells in PXS64-containing media. (D) The values of average area per cell calculated based on analyzing the epifluorescent images. These results indicated higher cell area for cells under the crowded condition and the efficacy of PXS64 to keep the cell spreading property similar to that of cells in the non-crowded state. * is $p < 0.05$ versus non-crowded condition ($n > 35$). The scale bars are 50 µm.

6.3.3 Collagen I deposition analysis

An excessive amount of collagen is a salient feature of fibrosis [291]. Several studies have reported the increase in type I collagen fibres in ECM of Dupuytren's cells [292]. Here, fluorescence microscopy was utilized to quantify the amount of collagen per cell after 72 h of exposure to different media. Moreover, such data provide one more evidence on the applicability of impedance measurement in antifibrotic screenings. The average amount of collagen that was deposited in ECM by each cell was calculated by following the immunocytochemistry strategy explained in "Scar-in-a-Jar" methodology [276]. Figure 6-3A-C show fluorescence microscopy images of the deposited collagen 1 (green) and nuclei (blue) from cells in one of the crowded, non-crowded or PXS64-containing crowded media. The area of deposited collagen I per cell was calculated by analysing the recorded fluorescence microscopy images (Figure 6-3D). The average collagen produced by cells under crowded media was 3.4-fold and 2.1-fold higher than that by cells cultured in PXS64-containing crowded media, respectively. The statistical analysis showed no significant difference between the amounts of deposited collagen from cells in PXS64-containing crowded media compared with cells under non-crowded condition. It is shown

that the excessive deposition of collagen increase the matrix stiffness and induces focal adhesions formation and stability through an increase in tension at these sites [293]. Thus, the extra deposited collagen by the cells that were cultured in crowded media contributed in raising the impedance value for cells under crowded state by improving the cell-surface adhesion.

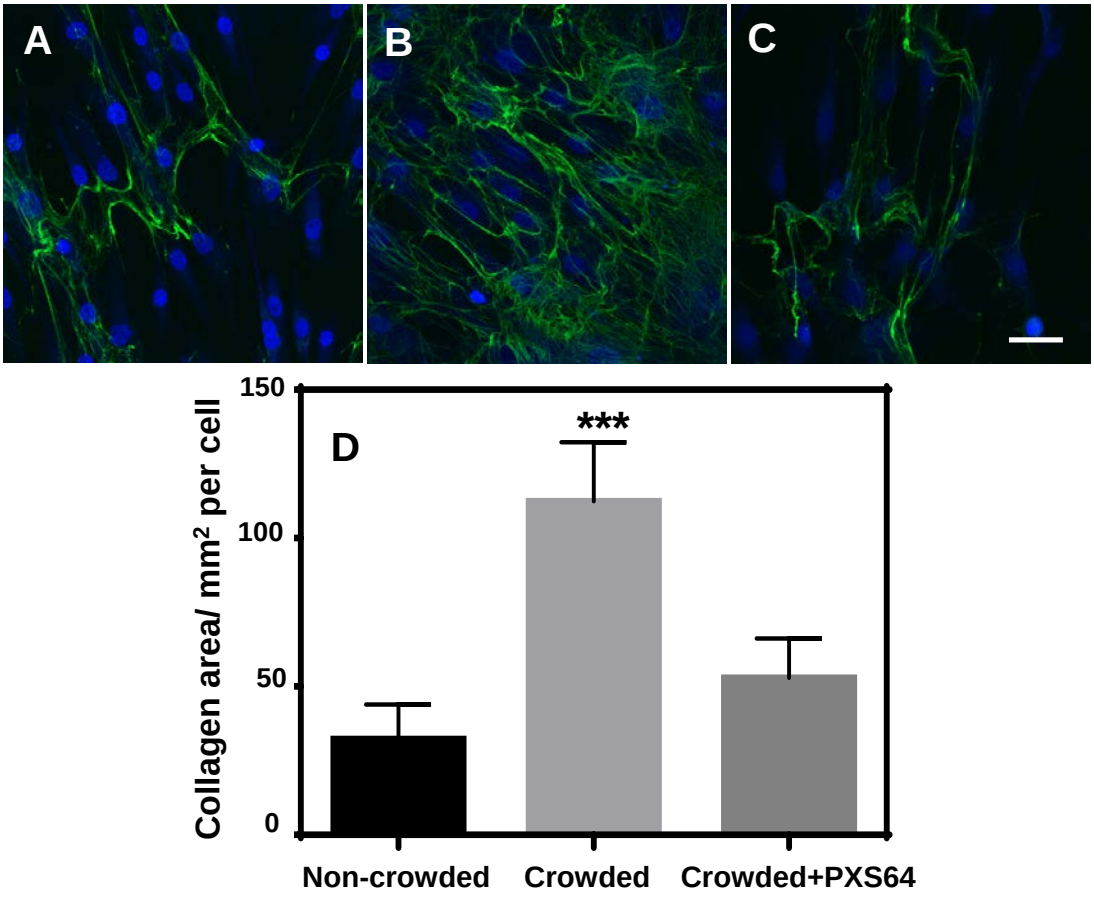

Figure 6-3. Collagen deposition analysis from the *in vitro* "Scar-in-a-Jar" study. Fluorescence microscopy images of deposited collagen I (green) and nuclei (blue) of cells exposed to (A) non-crowded, (B) crowded or (C) 10 μM PXS64-containing crowded media for 72 h. (D) Quantification of the area of stained deposited collagen I fibers per cell determined from the recorded microscopy images as are shown above. Cells under crowded condition deposited significantly greater amount of collagen compared with cells in the non-crowded state. The presence of 10 μM PXS64 significantly reduced the quantity of collagen fibers laying down in ECM under crowded

condition. Data displayed as a mean ± standard deviation (n>4). *** is $p < 0.001$ versus non-crowded condition. The scale bar is 100 µm.

6.3.4 Study the architecture of collagen fibrils

It has been demonstrated that the functionality of connective tissues directly depends on the alignment of collagen fibrils molecules [294]. During scar and fibrosis development, collagen fibrils undergo many synthesis, breakdown and cross-linking processes that strengthen and stabilize the formed tissue [295]. In this regard, it has been shown [293, 295] that abnormal alignment of the collagen is one of the characteristics of the formation of scar and fibrosis tissues. Therefore, an effective antifibrotic chemical not only restores the amount of collagen produced by cells but also keep the collagen alignment similar to their organization in the native cell environment. The coherency analysis of cells after 72 h culturing in one of the non-crowded, crowded or PXS64-containing crowded media is shown in Figure 6-4. A coherence of 0 means the most random orientation, and a coherence of 1 means the least random alignment. A highly oriented structure was observed for the collagen fibers produced by cells under the crowded condition compared with cells treated in non-crowded or PXS64-containing crowded media. In addition, there was no major difference between the architecture of collagen fibers deposited under non-crowded state or 10 µM PXS64-containg crowded media. These results indicated that PXS64 was effective in keeping the alignment of the collagen fibers in the crowded environment similar to those produced by cells under non-crowded condition. The alignment of collagen fibers can profoundly influence fibroblast cells to

orient themselves on rigid collagen fibers in the manner to generate maximal traction forces that stabilize integrin adhesions to promote focal adhesion maturation in the direction of collagen fiber orientation [293, 296]. Overall, the cell area and collagen deposition and alignment assays together confirmed the validity of impedance data on the effect of PXS64 on Dupuytren`s cells.

These results together demonstrated the higher cell coverage and stronger cell-surface adhesion for cells under the crowded condition that induce a scar-like condition than cells exposed to this condition in the presence of PXS64. It can be concluded that the higher impedance value for cells in crowded media compared with the other mentioned conditions were due to the higher cell coverage and well-adhered cells to the electrode surfaces.

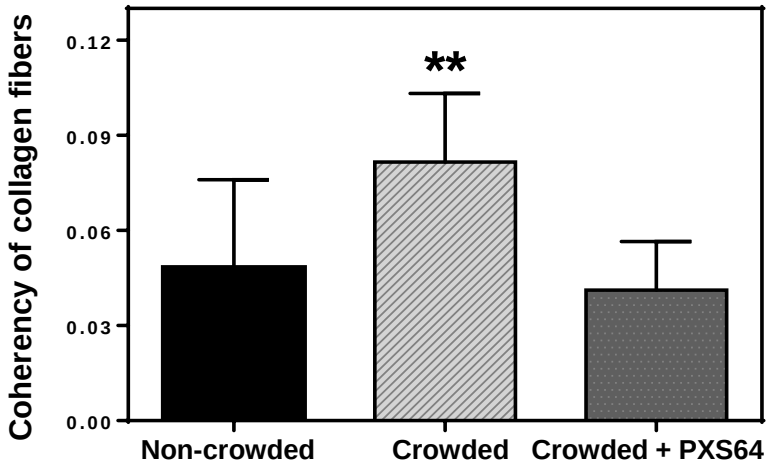

Figure 6-4. The coherency of collagen fibers deposited by cells exposed to non-crowded, crowded or PXS64-containing crowded media. The results suggest a significant coherence in the orientation of collagen fibers produced by cells under crowded condition versus the random alignment of collagen fibers deposited from cells treated in non-crowded or PXS64-containing crowded media. The collagen fibers exhibited similarity in their alignment when they were stimulated with 10 µM PXS64-containing crowded media. ** is $p < 0.01$ versus crowded media.

6.3.5 Ca^{2+} flux measurement

Herein, the efficacy of PXS64, in controlling fibrosis in Dupuytren`s cells was demonstrated both using a rapid and label-free electrochemical method and multiple microscopy assays. However, the mechanism through which PXS64 control the fibrosis progress in Dupuyren`s cells remain an open question. There is evidence demonstrating that several aspects of Ca^{2+} signalling behave abnormally in fibrotic cells [297, 298]. Ca^{2+} is engaged in extensive cellular responses and relaying intracellular messages [299]. Thus, to examine whether PXS64 control fibrosis progress through calcium signalling pathways, the cytosolic Ca^{2+} of Dupuytren`s cells was determined before and immediately (0h), 24 h, 48 h, and 72 h after changing the media to crowded, non-crowded or 10 µM PXS64-containing crowded media (Figure 6-5). The cytosolic calcium level for the cells in crowded media was considerably higher than that for cells in PXS64-containing crowded media after 48 h and 72 h. These are consistent with time points that were recognized using impedance measurement as the time that cell shape and adhesion of cells in crowded and PXS64-containg crowded media become significant.

Two possible sources of the increase in cytosolic Ca^{2+} are the release of calcium ions from internal stores and/or influx of Ca^{2+} from the extracellular space through the channels on the plasma membrane [300]. Thapsigargin was used to assess whether the origin of Ca^{2+} concentration is through the release of calcium from the endoplasmic reticulum. Thapsigargin elevates cytosolic Ca^{2+}

concentration by blocking the ability of the cell to pump calcium into the sarcoplasmic and endoplasmic reticula that cause the depletion of these stores [283]. The attenuation of cytosolic Ca^{2+} in the presence of thapsigargin indicated that the release of calcium ions from endoplasmic reticulum stores played a major role in increasing the cytosolic Ca^{2+} under the crowded condition that stimulates cells to go through fibrosis. Previously, the high activity of myosin light chain kinases (MLCK) in Dupuytren`s cells has been shown [300]. The activation of MLCK is intracellular $Ca^{2+}$ dependant. Thus, these results suggested the increased $Ca^{2+}$ level in Dupuytren`s cells. However, due to the inconsistency that was found in the expression of MLCK trough Dupuytren`s tissue, more studies, particularly on cells from different part of Dupuytren`s tissue, should be performed before concluding on intracellular calcium state in Dupuytren`s cells.

The intracellular Ca^{2+} for cells cultured in PXS64-containing crowded media was attenuated compared with those in crowded media. However, more studies are needed before envisaging biochemical therapeutic strategies based on the intervention of intracellular calcium.

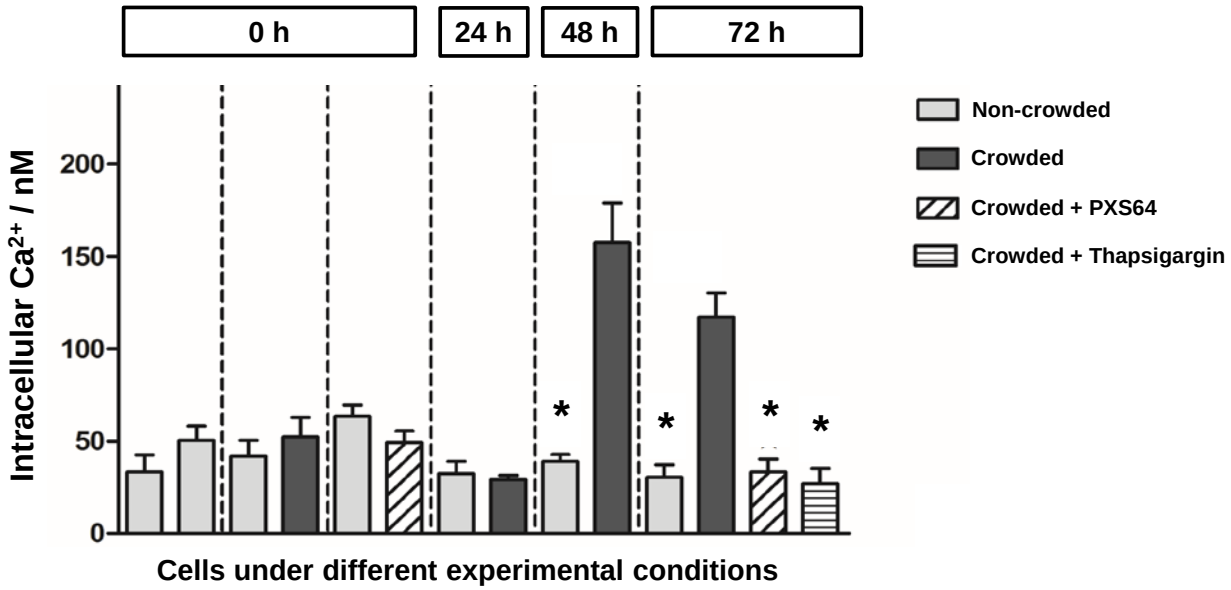

Figure 6-5. The intracellular Ca^{2+} of cells cultured in non-crowded, crowded, or 10 µM PXS64-containing crowded media immediately (0 h) and after 24 h, 48 h, and 72 h of changing the media. The increase in cytosolic Ca^{2+} after 72 h was significantly attenuated in the presence of either 10 µM PXS64 or 10nM Thapsigargin. The results indicated the capability of PXS64 in controlling the fibrosis progress and showed that the source of mobilized calcium was mainly from endoplasmic reticulum stores. * is $p < 0.05$ versus crowded condition.

6.4 SUMMARY

In summary, it was shown that the developed electrochemical bioimpedance assay have the capability of the screening the long-term effects of antifibrotic chemicals. This assay can be used as a label-free and non-distractive method to detect the appropriate doses and useful time windows of potential antifibrotic chemical compounds. The real-time impedance measurements were combined with the crowded strategy suggested in the "Scar-in-a-Jar" method to model the fibrotic disease *in vitro*. This combination facilitates the determination of the useful screening drug time window before performing laborious quantitative

measurement processes. The change in impedance magnitude was used as the measure to determine the effect of PXS64 on primary human cells collected from the palms of patients with Dupuytren`s disease. The fluorescence assays not only provided quantitative information on subcellular influences of the examined chemical but also confirmed the validity of the impedance method for monitoring potential therapeutical agents. The emergence of cell-based electrochemical impedance approaches for screening potential antifibrotic compounds opens new avenues to probe the dynamics of fibrosis in live cells in a real-time manner.

CHAPTER 7 CONCLUSIONS AND FUTURE WORK

7.1 SUMMARY

This thesis has presented results obtained during development of a cell-based assay that was used to study the various aspects of cells responses in the presence of physical and soluble cues. The opportunity of obtaining more comprehensive insight into cellular responses was provided by combining impedance spectroscopy and optical microscopy techniques. Optical microscopy techniques, fluorescence in particular, were employed to detect short-lived subcellular events. Impedance spectroscopy monitored alterations in cell adhesion and morphology in a label-free and real-time manner over an extended period of time. The transparency and conductivity of interdigitated ITO electrodes supplied a substrate compatible with both techniques. A stable and robust surface modification strategy provided a well-controlled environment for cell adhesion. The application of the developed dual impedance/microscopy setup was extended to screen a potential anti-fibrosis compound.

In the earlier parts of the research (**Chapter 3**), gold electrodes, as the most common surface for bioelectrical measurements, were modified with low impedance and antifouling coatings. The ability of the developed coatings in limiting nonspecific proteins adsorption was confirmed using fluorescence microscopy and electrochemical impedance spectroscopy. These features were prerequisites of the substrate for developing a cell-based biosensor. Using gold for optical microscopy of cells was challenging due to quench of the fluorescence and lack of transparency.

Chapter 4 discusses the modification of indium−tin oxide (ITO) electrodes as transparent and conductive interfaces with controlled density of RGD adhesive ligands. A setup for running simultaneous live optical microscopy and impedance spectroscopy was designed. The simultaneous microscopy and electrochemistry results were employed to coordinate the impedance data with the amount of cell coverage on the surface. The developed system showed the dependency of cell adhesion kinetic to the expression of different RGD spacing.

Chapter 5 illustrates the application of the developed dual readout system using live fluorescence and impedance spectroscopy to investigate how surface chemistry influences the cell responses to soluble cues. G-protein coupled cell receptors were used as the pathway interrupted with soluble cues inducing changes in cell shape and adhesion as well as intracellular signalling (e.g., calcium signalling). This part of the study revealed the importance of controlling the cellular adhesive environment on cell response to chemical cues.

Chapter 6 demonstrates the developed cell chip efficacy to acquire biological information on the effect of potential anti-fibrotic compounds on primary human cells. The impedance spectroscopy on interdigitated ITO surfaces was used to detect the useful time window of the potential therapeutic agent. The microscopy analyses performed afterwards provided quantitative subcellular information on the effects of the examined agent per individual cell. The results of this chapter confirmed the capability of the developed device for drug-screening applications. In summary, this study revealed the power of the developed dual approaches using live optical and impedance measurements in screening the cell behaviour

and aiding in answering biological questions. The results demonstrated the role of expression of physical cues in regulating cell adhesion and attachment and modulating the cell responses to soluble cues.

7.2 FUTURE WORKS

7.2.1 Finding the mechanisms behind cell response to GPCRs agonists

Achieving a deeper understanding of the mechanisms behind the drug functions to aid in developing more efficient therapies. Most of the current drugs in the market targets GPCRs on the cell membrane to trigger cell responses [301]. It was found in this study that the timescale of calcium signalling mobilization correlated the best with duration of the decrease in cell-cell adhesion in response to histamine as a GPCRs agonist (Chapter 5). It was shown in this project and in the literature [265, 302, 303] that calcium release and cytoskeleton arrangement crosstalk in a bi-directional manner. However, the exact pathway that connects the organization of cell adhesive ligands to the modulation of outside-in signalling of cells is an open question. The developed setup using simultaneous microscopy and impedance spectroscopy can be used to answer the biological questions on the mediators of these events. Different actin disturbing agents can be used to find out that which part of the cytoskeleton structure is mediating the change in cell morphology and adhesion in response to histamine or other stimulators of GPCRs. For instance, cells can be incubated with blebbistatin [304] before addition of histamine to find out if myosin light chain kinase (MLCK) is mediating the change in the cytoskeleton. Subsequently, other actin disturbing agents such as latrunculin A [305] that sequester the free actin can be

used to examine the role of free actin in response to histamine. The Rho-kinase (ROCK) inhibitors [306, 307] are other potential candidates which can be utilized to achieve a better understanding of the mechanism of behind the effects of GPCRs stimulators on cells.

7.2.2 Personalized medicine

It is shown that not only different drugs have unique effects on cell behaviour, but also the responses of individuals can be unique due to genetic variations and body factors that contribute to human illness. Having accurate diagnostic tests aid in the success of personalized medicine to recognize the patients that can benefit from targeted medicine [308]. A future work can be based on investigating the effect of therapies on the same kind of cell lines from different patients. Personalized medicine is a key to ensuring that patients will receive the best suited possible therapy [309].

7.2.3 Screening newly developed therapeutic compounds

The pharmaceutical industry frequently use a series of in vitro toxicity testing and functional biochemical high throughput screening assays to assess the potential molecule libraries and build new classes of lead compounds [59]. In these tests, the affinity and binding efficacy of the testing agent to the target of interest is performed. These assays are mainly based on enzyme inhibition and ligand-receptor binding tests [179]. Recently using live cells as sensing elements for drug screening applications has been considered as a more physiologically relevant assay than the biochemical tests [85, 310]. In addition, the purification

and preparing of targets in biochemical assays in some cases is challenging [179]. The 2-D cell assays can be used to evaluate the potency, selectivity, identifying the mode of action of drugs, the effect of cocktailing several drugs or studying the drug resistance analyses. However, it is challenging to extract comprehensive information on cell responses to a potential therapeutic agent. The developed simultaneous fluorescence/impedance spectroscopy setup can be used as a platform for screening the effect of potential therapeutic molecules. The system can be employed to find the efficient dose of drugs and the duration that they should be exposed to cells. Most of commercially available therapeutic compounds target GPCRs as the pathway to influence the cellular behavior. The activation of GPCRS, activate different intracellular events detectable using fluorescence microscopy such as change in secondary messengers Ca^{2+} and cAMP. In addition, it cause alteration in cell adhesion and morphology that can be detected using impedance spectroscopy. In this study, the effect of a new prodrug, PXS64 on primary human cells was examined (Chapter 6). To extend the application of the system as a platform for drug testing, one of the important requirements is that the influences of many different drugs on various cells have to be examined.

7.2.4 Increasing the optical resolution of microscopy images on interdigitated ITO electrodes

In the present project, the quality of phase contrast images (Chapter 5) was compromised by the thickness of the slides (Figure 7-1). The current design is superior as a big counter, and a reference electrode have been printed on the surfaces. Moreover, the area of the electrochemically active part of the electrode

is defined due to coating the electrode with an insulating membrane. However, the current resolution of phase contrast images can be enhanced by improving the design and fabrication methods of interdigitated ITO electrodes, e.g. decreasing the total thickness of the underlying quartz substrate. The quality of the optical images on plain ITO has been shown to be high. Various lithography [311] and non-lithography [312] methods can be employed to fabricate interdigitated ITO electrodes with the capability of capturing high quality transmitted light microscopy images.

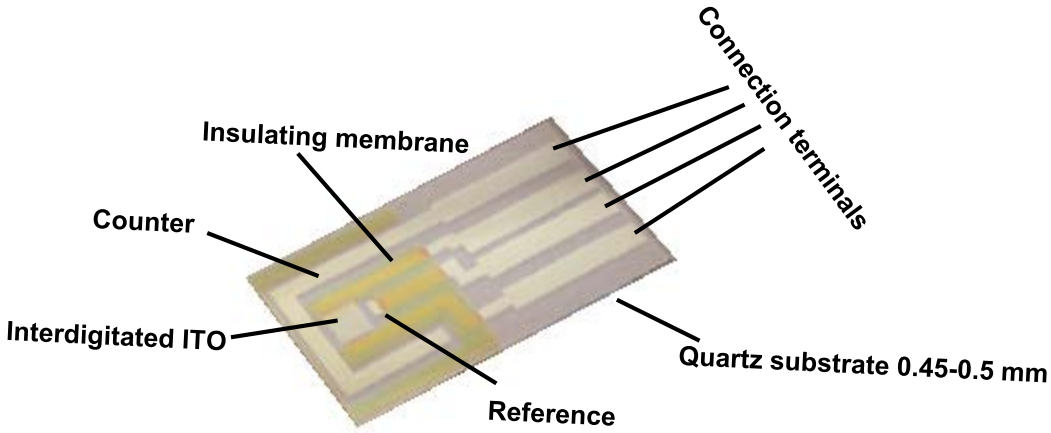

Figure 7-1. Commercial interdigitated ITO electrodes. The thickness of the quartz substrates can be decreased by fabricating more thin electrodes.

REFERENCES

1. Bolon, B., *Genetically engineered animals in drug discovery and development: a maturing resource for toxicologic research.* Basic & clinical pharmacology & toxicology, 2004. **95**(4): p. 154-161.
2. Maggi, A. and P. Ciana, *Reporter mice and drug discovery and development.* Nature Reviews Drug Discovery, 2005. **4**(3): p. 249-255.
3. Frank, R. and R. Hargreaves, *Clinical biomarkers in drug discovery and development.* Nature Reviews Drug Discovery, 2003. **2**(7): p. 566-580.
4. Lilienblum, W., et al., *Alternative methods to safety studies in experimental animals: role in the risk assessment of chemicals under the new European Chemicals Legislation (REACH).* Archives of toxicology, 2008. **82**(4): p. 211-236.
5. Russell, W.M.S., R.L. Burch, and C.W. Hume, *The principles of humane experimental technique.* 1959.
6. Rose, M. and E. Grant. *Australia's ethical framework for animals used in research and teaching*. in *Proceedings of AAWS International Animal Welfare Conference*. 2008.
7. Leist, M., et al., *Novel technologies and an overall strategy to allow hazard assessment and risk prediction of chemicals, cosmetics, and drugs with animal-free methods.* Altex, 2012. **29**(4): p. 373-388.
8. Hendriksen, C.F., *Replacement, reduction and refinement alternatives to animal use in vaccine potency measurement.* Expert review of vaccines, 2009. **8**(3): p. 313-322.
9. Reagan-Shaw, S., M. Nihal, and N. Ahmad, *Dose translation from animal to human studies revisited.* The FASEB journal, 2008. **22**(3): p. 659-661.
10. Van der Worp, H.B., et al., *Can animal models of disease reliably inform human studies?* PLoS med, 2010. **7**(3): p. e1000245.
11. Hartung, T., *Food for thought look back in anger–What clinical studies tell us about preclinical work.* Altex, 2013. **30**(3): p. 275.
12. Food and D. Administration, *Innovation or stagnation: challenge and opportunity on the critical path to new medical products.* Food and Drug Administration, critical path report, 2004.

13. Turner, A., I. Karube, and G.S. Wilson, *Biosensors: fundamentals and applications.* 1987.
14. Turner, A.P., *Biosensors: sense and sensibility.* Chemical Society Reviews, 2013. **42**(8): p. 3184-3196.
15. Pancrazio, J., et al., *Development and application of cell-based biosensors.* Annals of biomedical engineering, 1999. **27**(6): p. 697-711.
16. Lukashev, M.E. and Z. Werb, *ECM signalling: orchestrating cell behaviour and misbehaviour.* Trends in cell biology, 1998. **8**(11): p. 437-441.
17. Ruoslahti, E., *RGD and other recognition sequences for integrins.* Annual review of cell and developmental biology, 1996. **12**(1): p. 697-715.
18. Clark, E.A. and J.S. Brugge, *Integrins and signal transduction pathways: the road taken.* Science, 1995. **268**(5208): p. 233.
19. Hynes, R.O., *Integrins: versatility, modulation, and signaling in cell adhesion.* Cell, 1992. **69**(1): p. 11-25.
20. Gooding, J.J., et al., *Molecularly Engineered Surfaces for Cell Biology: From Static to Dynamic Surfaces.* Langmuir, 2013.
21. Geiger, B., J.P. Spatz, and A.D. Bershadsky, *Environmental sensing through focal adhesions.* Nature reviews Molecular cell biology, 2009. **10**(1): p. 21-33.
22. Kholodenko, B.N., *Cell-signalling dynamics in time and space.* Nature reviews Molecular cell biology, 2006. **7**(3): p. 165-176.
23. Rørth, P., *Communication by touch: role of cellular extensions in complex animals.* Cell, 2003. **112**(5): p. 595-598.
24. Vogel, V. and M. Sheetz, *Local force and geometry sensing regulate cell functions.* Nature reviews Molecular cell biology, 2006. **7**(4): p. 265-275.
25. Connelly, J.T., et al., *Actin and serum response factor transduce physical cues from the microenvironment to regulate epidermal stem cell fate decisions.* nature cell biology, 2010. **12**(7): p. 711-718.
26. Guilak, F., et al., *Control of stem cell fate by physical interactions with the extracellular matrix.* Cell stem cell, 2009. **5**(1): p. 17-26.
27. Frith, J.E., R.J. Mills, and J.J. Cooper-White, *Lateral spacing of adhesion peptides influences human mesenchymal stem cell behaviour.* Journal of Cell Science, 2012. **125**(2): p. 317-327.

28. Dike, L.E., et al., *Geometric control of switching between growth, apoptosis, and differentiation during angiogenesis using micropatterned substrates.* In Vitro Cellular & Developmental Biology - Animal, 1999. **35**(8): p. 441-448.
29. Chen, C.S., et al., *Geometric control of cell life and death.* Science, 1997. **276**(5317): p. 1425-1428.
30. Hoffman-Kim, D., J.A. Mitchel, and R.V. Bellamkonda, *Topography, cell response, and nerve regeneration.* Annual review of biomedical engineering, 2010. **12**: p. 203.
31. Le Saux, G., et al., *The relative importance of topography and RGD ligand density for endothelial cell adhesion.* PLoS One, 2011. **6**(7): p. e21869.
32. Hynes, R.O., *The extracellular matrix: not just pretty fibrils.* Science, 2009. **326**(5957): p. 1216-1219.
33. Boudreau, N.J. and P.L. Jones, *Extracellular matrix and integrin signalling: the shape of things to come.* Biochemical Journal, 1999. **339**(3): p. 481-488.
34. Alexander, J.S. and J.W. Elrod, *Extracellular matrix, junctional integrity and matrix metalloproteinase interactions in endothelial permeability regulation.* Journal of Anatomy, 2002. **200**(6): p. 561-574.
35. Humphrey, J.D., E.R. Dufresne, and M.A. Schwartz, *Mechanotransduction and extracellular matrix homeostasis.* Nature reviews Molecular cell biology, 2014. **15**(12): p. 802-812.
36. El-Ali, J., P.K. Sorger, and K.F. Jensen, *Cells on chips.* Nature, 2006. **442**(7101): p. 403-411.
37. Nagavarapu, U., *Cell-based assays: technologies and global markets.* BCC Research, 2011: p. 188.
38. Rawson, D.M., A.J. Willmer, and A.P. Turner, *Whole-cell biosensors for environmental monitoring.* Biosensors, 1989. **4**(5): p. 299-311.
39. Otero-Gonzalez, L., et al., *Application and validation of an impedance-based real time cell analyzer to measure the toxicity of nanoparticles impacting human bronchial epithelial cells.* Environ Sci Technol, 2012. **46**(18): p. 10271-8.

40. Bukoreshtliev, N.V., K. Haase, and A.E. Pelling, *Mechanical cues in cellular signalling and communication.* Cell and tissue research, 2013. **352**(1): p. 77-94.
41. Haase, K., Z. Al-Rekabi, and A.E. Pelling, *Mechanical cues direct focal adhesion dynamics.* Progress in molecular biology and translational science, 2014. **126**: p. 103-34.
42. Davies, P.F. and S.C. Tripathi, *Mechanical stress mechanisms and the cell. An endothelial paradigm.* Circulation research, 1993. **72**(2): p. 239-245.
43. Brighton, C.T., et al., *In Vitro Bone-Cell Response to a Capacitively Coupled Electrical Field The Role of Field Strength, Pulse Pattern, and Duty Cycle.* Clinical orthopaedics and related research, 1992. **285**: p. 255-262.
44. Joshi, R.P., Q. Hu, and K.H. Schoenbach, *Modeling studies of cell response to ultrashort, high-intensity electric fields-implications for intracellular manipulation.* IEEE transactions on plasma science, 2004. **32**(4): p. 1677-1686.
45. Larsen, G.L., et al., *Airway response to electrical field stimulation in sensitized inbred mice. Passive transfer of increased responsiveness with peribronchial lymph nodes.* Journal of Clinical Investigation, 1992. **89**(3): p. 747.
46. Krassowska, W. and J.C. Neu, *Response of a single cell to an external electric field.* Biophysical journal, 1994. **66**(6): p. 1768.
47. Robinson, K.R., *The responses of cells to electrical fields: a review.* The Journal of cell biology, 1985. **101**(6): p. 2023-2027.
48. Yen-Patton, G., et al., *Endothelial cell response to pulsed electromagnetic fields: stimulation of growth rate and angiogenesis in vitro.* Journal of cellular physiology, 1988. **134**(1): p. 37-46.
49. Naarala, J., A. Höytö, and A. Markkanen, *Cellular effects of electromagnetic fields.* Alternatives to laboratory animals: ATLA, 2004. **32**(4): p. 355-360.
50. Frey, C.B., *Intellectual property rights and the financing of technological innovation: public policy and the efficiency of capital markets*. 2013: Edward Elgar Publishing.

51. Varshney, M. and Y. Li, *Interdigitated array microelectrodes based impedance biosensors for detection of bacterial cells.* Biosensors and Bioelectronics, 2009. **24**(10): p. 2951-2960.
52. Thibodeau, S.A., R. Fang, and J.K. Joung, *High-throughput beta-galactosidase assay for bacterial cell-based reporter systems.* Biotechniques, 2004. **36**(3): p. 410-417.
53. Yang, L., *Electrical impedance spectroscopy for detection of bacterial cells in suspensions using interdigitated microelectrodes.* Talanta, 2008. **74**(5): p. 1621-1629.
54. Watson, A.L. and N.H. Chiu, *Fluorometric cell-based assay for β-galactosidase activity in probiotic gram-positive bacterial cells—Lactobacillus helveticus.* Journal of Microbiological Methods, 2016.
55. Stolwijk, J., et al., *Impedance analysis of GPCR-mediated changes in endothelial barrier function: overview and fundamental considerations for stable and reproducible measurements.* Pflügers Archiv - European Journal of Physiology, 2014: p. 1-26.
56. Mrksich, M., *What can surface chemistry do for cell biology?* Current opinion in chemical biology, 2002. **6**(6): p. 794-797.
57. Atienza, J.M., et al., *Dynamic monitoring of cell adhesion and spreading on microelectronic sensor arrays.* Journal of biomolecular screening, 2005. **10**(8): p. 795-805.
58. Jessup, J., T. Goodwin, and G. Spaulding, *Prospects for use of microgravity-based bioreactors to study three-dimensional host—tumor interactions in human neoplasia.* Journal of cellular biochemistry, 1993. **51**(3): p. 290-300.
59. Kunz-Schughart, L.A., et al., *The use of 3-D cultures for high-throughput screening: the multicellular spheroid model.* Journal of biomolecular screening, 2004. **9**(4): p. 273-285.
60. Browning, M.B., et al., *Endothelial cell response to chemical, biological, and physical cues in bioactive hydrogels.* Tissue Engineering Part A, 2014. **20**(23-24): p. 3130-3141.
61. Cheng, K., Y. Lai, and W.S. Kisaalita, *Three-dimensional polymer scaffolds for high throughput cell-based assay systems.* Biomaterials, 2008. **29**(18): p. 2802-2812.

62. Powers, M.J., et al., *A microfabricated array bioreactor for perfused 3D liver culture.* Biotechnology and Bioengineering, 2002. **78**(3): p. 257-269.
63. Edmondson, R., et al., *Three-Dimensional Cell Culture Systems and Their Applications in Drug Discovery and Cell-Based Biosensors.* Assay and Drug Development Technologies, 2014. **12**(4): p. 207-218.
64. Xu, T., et al., *Viability and electrophysiology of neural cell structures generated by the inkjet printing method.* Biomaterials, 2006. **27**(19): p. 3580-3588.
65. Shi, B.-X., et al., *Release monitoring of single cells on a microfluidic device coupled with fluorescence microscopy and electrochemistry.* Biomicrofluidics, 2010. **4**(4): p. -.
66. Kim, M.S., J.H. Yeon, and J.-K. Park, *A microfluidic platform for 3-dimensional cell culture and cell-based assays.* Biomedical microdevices, 2007. **9**(1): p. 25-34.
67. Bissell, M., *Biology's new dimension.* Nature, 2003. **424**: p. 870-872.
68. Cahill, P.S., et al., *Microelectrodes for the measurement of catecholamines in biological systems.* Analytical chemistry, 1996. **68**(18): p. 3180-3186.
69. Juliano, R., *Signal transduction by cell adhesion receptors and the cytoskeleton: functions of integrins, cadherins, selectins, and immunoglobulin-superfamily members.* Annual review of pharmacology and toxicology, 2002. **42**(1): p. 283-323.
70. Adams, J.C. and F.M. Watt, *Regulation of development and differentiation by the extracellular matrix.* Development, 1993. **117**(4): p. 1183-1198.
71. Mrksich, M., *Tailored substrates for studies of attached cell culture.* Cellular and Molecular Life Sciences CMLS, 1998. **54**(7): p. 653-662.
72. Keselowsky, B.G., D.M. Collard, and A.J. García, *Integrin binding specificity regulates biomaterial surface chemistry effects on cell differentiation.* Proceedings of the National Academy of Sciences, 2005. **102**(17): p. 5953-5957.
73. Hersel, U., C. Dahmen, and H. Kessler, *RGD modified polymers: biomaterials for stimulated cell adhesion and beyond.* Biomaterials, 2003. **24**(24): p. 4385-4415.

74. Prime, K.L. and G.M. Whitesides, *Adsorption of proteins onto surfaces containing end-attached oligo (ethylene oxide): a model system using self-assembled monolayers.* Journal of the American Chemical Society, 1993. **115**(23): p. 10714-10721.
75. Gui, A.L., et al., *Zwitterionic Phenyl Layers: Finally, Stable, Anti-Biofouling Coatings that Do Not Passivate Electrodes.* ACS Applied Materials & Interfaces, 2013. **5**(11): p. 4827-4835.
76. Jiang, C., et al., *Zwitterionic Phenyl Phosphorylcholine on Indium Tin Oxide: a Low-Impedance Protein-Resistant Platform for Biosensing.* Electroanalysis, 2015. **27**(4): p. 884-889.
77. Kato, M. and M. Mrksich, *Using model substrates to study the dependence of focal adhesion formation on the affinity of integrin-ligand complexes.* Biochemistry, 2004. **43**(10): p. 2699-2707.
78. Xiao, Y. and G.A. Truskey, *Effect of receptor-ligand affinity on the strength of endothelial cell adhesion.* Biophysical journal, 1996. **71**(5): p. 2869.
79. Arnold, M., et al., *Activation of integrin function by nanopatterned adhesive interfaces.* ChemPhysChem, 2004. **5**(3): p. 383-388.
80. Cavalcanti-Adam, E.A., et al., *Cell spreading and focal adhesion dynamics are regulated by spacing of integrin ligands.* Biophysical journal, 2007. **92**(8): p. 2964-2974.
81. Le Saux, G., et al., *Spacing of integrin ligands influences signal transduction in endothelial cells.* Biophysical journal, 2011. **101**(4): p. 764-773.
82. Huang, J., et al., *Impact of order and disorder in RGD nanopatterns on cell adhesion.* Nano Letters, 2009. **9**(3): p. 1111-1116.
83. Bluemmel, J., et al., *Protein repellent properties of covalently attached PEG coatings on nanostructured SiO 2-based interfaces.* Biomaterials, 2007. **28**(32): p. 4739-4747.
84. Houseman, B.T. and M. Mrksich, *The microenvironment of immobilized Arg-Gly-Asp peptides is an important determinant of cell adhesion.* Biomaterials, 2001. **22**(9): p. 943-955.
85. Wang, P., et al., *Cell-based biosensors and its application in biomedicine.* Sensors and Actuators B: Chemical, 2005. **108**(1): p. 576-584.

86. Riss, T., R. Moravec, and A. Niles, *Selecting cell-based assays for drug discovery screening.* Cell Notes, 2005. **13**: p. 16-21.
87. Shacham-Diamand, Y., et al., *Optical and electrical interfacing technologies for living cell bio-chips.* Current pharmaceutical biotechnology, 2010. **11**(4): p. 376-383.
88. Ru, J., et al., *Ratiometric Iridium (III) Complex-Based Phosphorescent Chemodosimeter for Hg2+ Applicable in Time-Resolved Luminescence Assay and Live Cell Imaging.* Analytical chemistry, 2015. **87**(6): p. 3255-3262.
89. Trepte, P., et al., *DULIP: a dual luminescence-based co-immunoprecipitation assay for interactome mapping in mammalian cells.* Journal of molecular biology, 2015. **427**(21): p. 3375-3388.
90. Nakashima, M., et al., *Cell-based assay of nongenomic actions of progestins revealed inhibitory G protein coupling to membrane progestin receptor α (mPRα).* Steroids, 2015. **100**: p. 21-26.
91. Kain, S.R., *Green fluorescent protein (GFP): applications in cell-based assays for drug discovery.* Drug discovery today, 1999. **4**(7): p. 304-312.
92. Barak, L.S., et al., *A β-arrestin/green fluorescent protein biosensor for detecting G protein-coupled receptor activation.* Journal of Biological Chemistry, 1997. **272**(44): p. 27497-27500.
93. Damayanti, N.P., L.L. Parker, and J.M. Irudayaraj, *Fluorescence lifetime imaging of biosensor peptide phosphorylation in single live cells.* Angewandte Chemie, 2013. **125**(14): p. 4023-4026.
94. Lorenzen, A. and S.W. Kennedy, *A fluorescence-based protein assay for use with a microplate reader.* Analytical biochemistry, 1993. **214**(1): p. 346-348.
95. Kicka, S., et al., *Establishment and validation of whole-cell based fluorescence assays to identify anti-mycobacterial compounds using the Acanthamoeba castellanii-Mycobacterium marinum host-pathogen system.* PloS one, 2014. **9**(1): p. e87834.
96. Mattheakis, L.C., et al., *Optical coding of mammalian cells using semiconductor quantum dots.* Analytical Biochemistry, 2004. **327**(2): p. 200-208.

97. Chinen, A.B., et al., *Nanoparticle Probes for the Detection of Cancer Biomarkers, Cells, and Tissues by Fluorescence.* Chemical Reviews, 2015. **115**(19): p. 10530-10574.
98. Mosmann, T., *Rapid colorimetric assay for cellular growth and survival: application to proliferation and cytotoxicity assays.* Journal of immunological methods, 1983. **65**(1-2): p. 55-63.
99. Fang, Y., *Label-free cell-based assays with optical biosensors in drug discovery.* Assay and drug development technologies, 2006. **4**(5): p. 583-595.
100. Homola, J., *Present and future of surface plasmon resonance biosensors.* Analytical and bioanalytical chemistry, 2003. **377**(3): p. 528-539.
101. Hide, M., et al., *Real-time analysis of ligand-induced cell surface and intracellular reactions of living mast cells using a surface plasmon resonance-based biosensor.* Analytical biochemistry, 2002. **302**(1): p. 28-37.
102. Quinn, J.G., et al., *Development and application of surface plasmon resonance-based biosensors for the detection of cell–ligand interactions.* Analytical biochemistry, 2000. **281**(2): p. 135-143.
103. Klein, A.B., et al., *Demonstration of the dynamic mass redistribution label-free technology as a useful cell-based pharmacological assay for endogenously expressed GABA A receptors.* MedChemComm, 2016. **7**(3): p. 426-432.
104. Schröder, R., et al., *Deconvolution of complex G protein-coupled receptor signaling in live cells using dynamic mass redistribution measurements.* Nature biotechnology, 2010. **28**(9): p. 943-949.
105. Kebig, A., et al., *An optical dynamic mass redistribution assay reveals biased signaling of dualsteric GPCR activators.* Journal of Receptors and Signal Transduction, 2009. **29**(3-4): p. 140-145.
106. Shamah, S.M. and B.T. Cunningham, *Label-free cell-based assays using photonic crystal optical biosensors.* Analyst, 2011. **136**(6): p. 1090-1102.
107. Kilian, K.A., et al., *Si–C linked oligo (ethylene glycol) layers in silicon-based photonic crystals: optimization for implantable optical materials.* Biomaterials, 2007. **28**(20): p. 3055-3062.

108. Owen, D.M., et al., *PALM imaging and cluster analysis of protein heterogeneity at the cell surface.* Journal of biophotonics, 2010. **3**(7): p. 446-454.
109. Hess, S.T., T.P. Girirajan, and M.D. Mason, *Ultra-high resolution imaging by fluorescence photoactivation localization microscopy.* Biophysical journal, 2006. **91**(11): p. 4258-4272.
110. Williamson, D.J., et al., *Pre-existing clusters of the adaptor Lat do not participate in early T cell signaling events.* Nature immunology, 2011. **12**(7): p. 655-662.
111. Heilemann, M., et al., *Subdiffraction-resolution fluorescence imaging with conventional fluorescent probes.* Angewandte Chemie International Edition, 2008. **47**(33): p. 6172-6176.
112. Cheng, L., C. Wang, and Z. Liu, *Upconversion nanoparticles and their composite nanostructures for biomedical imaging and cancer therapy.* Nanoscale, 2013. **5**(1): p. 23-37.
113. Johnson, I., *Review: Fluorescent probes for living cells.* The Histochemical Journal, 1998. **30**(3): p. 123-140.
114. Wokosin, D.L., C.M. Loughrey, and G.L. Smith, *Characterization of a Range of Fura Dyes with Two-Photon Excitation.* Biophysical Journal, 2004. **86**(3): p. 1726-1738.
115. Robinson, J.A., et al., *Ratiometric and nonratiometric Ca2+ indicators for the assessment of intracellular free Ca2+ in a breast cancer cell line using a fluorescence microplate reader.* Journal of Biochemical and Biophysical Methods, 2004. **58**(3): p. 227-237.
116. Nishigaki, T., et al., *Stroboscopic illumination using light-emitting diodes reduces phototoxicity in fluorescence cell imaging.* Biotechniques, 2006. **41**(2): p. 191.
117. Hoebe, R., et al., *Controlled light-exposure microscopy reduces photobleaching and phototoxicity in fluorescence live-cell imaging.* Nature biotechnology, 2007. **25**(2): p. 249-253.
118. Shimomura, O., F.H. Johnson, and Y. Saiga, *Extraction, purification and properties of aequorin, a bioluminescent protein from the luminous hydromedusan, Aequorea.* Journal of cellular and comparative physiology, 1962. **59**(3): p. 223-239.

119. Prasher, D.C., et al., *Primary structure of the Aequorea victoria green-fluorescent protein.* Gene, 1992. **111**(2): p. 229-233.
120. Chalfie, M., *Green fluorescent protein as a marker for gene expression.* Trends in Genetics, 1994. **10**(5): p. 151.
121. Inouye, S. and F.I. Tsuji, *Aequorea green fluorescent protein.* FEBS letters, 1994. **341**(2-3): p. 277-280.
122. Tsien, R.Y., *The green fluorescent protein.* Annual review of biochemistry, 1998. **67**(1): p. 509-544.
123. Zimmer, M., *Green fluorescent protein (GFP): applications, structure, and related photophysical behavior.* Chemical reviews, 2002. **102**(3): p. 759-782.
124. Heilemann, M., et al., *Super-resolution imaging with small organic fluorophores.* Angewandte Chemie International Edition, 2009. **48**(37): p. 6903-6908.
125. Lichtman, J.W. and J.-A. Conchello, *Fluorescence microscopy.* Nature methods, 2005. **2**(12): p. 910-919.
126. Ding, L., et al., *Trends in cell-based electrochemical biosensors.* Current medicinal chemistry, 2008. **15**(30): p. 3160-3170.
127. Cahill, P.S. and R.M. Wightman, *Simultaneous amperometric measurement of ascorbate and catecholamine secretion from individual bovine adrenal medullary cells.* Analytical chemistry, 1995. **67**(15): p. 2599-2605.
128. Wightman, R.M., et al., *Time course of release of catecholamines from individual vesicles during exocytosis at adrenal medullary cells.* Biophysical Journal, 1995. **68**(1): p. 383-390.
129. Leszczyszyn, D.J., et al., *Secretion of catecholamines from individual adrenal medullary chromaffin cells.* Journal of neurochemistry, 1991. **56**(6): p. 1855-1863.
130. Chow, R.H., L. von Rüden, and E. Neher, *Delay in vesicle fusion revealed by electrochemical monitoring of single secretory events in adrenal chromaffin cells.* 1992.
131. Dugast, C., M.-F. Suaud-Chagny, and F. Gonon, *Continuousin vivo monitoring of evoked dopamine release in the rat nucleus accumbens by amperometry.* Neuroscience, 1994. **62**(3): p. 647-654.

132. Kawagoe, K.T. and R.M. Wightman, *Characterization of amperometry for in vivo measurement of dopamine dynamics in the rat brain.* Talanta, 1994. **41**(6): p. 865-874.
133. Amatore, C., et al., *Electrochemical monitoring of single cell secretion: vesicular exocytosis and oxidative stress.* Chemical reviews, 2008. **108**(7): p. 2585-2621.
134. Zamaleeva, A.I., et al., *A whole-cell amperometric herbicide biosensor based on magnetically functionalised microalgae and screen-printed electrodes.* Analytical Methods, 2011. **3**(3): p. 509-513.
135. Jacobs, C.B., M.J. Peairs, and B.J. Venton, *Review: Carbon nanotube based electrochemical sensors for biomolecules.* Analytica Chimica Acta, 2010. **662**(2): p. 105-127.
136. Lindau, M. and G. Alvarez de Toledo, *The fusion pore.* Biochimica et Biophysica Acta (BBA) - Molecular Cell Research, 2003. **1641**(2–3): p. 167-173.
137. Amatore, C., et al., *Coupling of Electrochemistry and Fluorescence Microscopy at Indium Tin Oxide Microelectrodes for the Analysis of Single Exocytotic Events.* Angewandte Chemie International Edition, 2006. **45**(24): p. 4000-4003.
138. Burgoyne, R.D. and A. Morgan, *Secretory granule exocytosis.* Physiological reviews, 2003. **83**(2): p. 581-632.
139. Wightman, R., et al., *Temporally resolved catecholamine spikes correspond to single vesicle release from individual chromaffin cells.* Proceedings of the National Academy of Sciences, 1991. **88**(23): p. 10754-10758.
140. Hochstetler, S.E., et al., *Real-time amperometric measurements of zeptomole quantities of dopamine released from neurons.* Analytical chemistry, 2000. **72**(3): p. 489-496.
141. Bunea, A.-I., et al. *SU-8-Derived Carbon Nanopillars Enhance Stem Cell Differentiation into Dopaminergic Neurons*. in *Meeting Abstracts*. 2016. The Electrochemical Society.
142. Kang, M., et al., *Electro-triggering and electrochemical monitoring of dopamine exocytosis from a single cell by using ultrathin electrodes based on Au nanowires.* Nanoscale, 2016. **8**(1): p. 214-218.

143. Yang, C., et al., *Laser Treated Carbon Nanotube Yarn Microelectrodes for Rapid and Sensitive Detection of Dopamine in Vivo.* ACS Sensors, 2016. **1**(5): p. 508-515.
144. Li, Y.T., et al., *Real-time Monitoring of Discrete Synaptic Release Events and Excitatory Potentials within Self-reconstructed Neuromuscular Junctions.* Angewandte Chemie International Edition, 2015. **54**(32): p. 9313-9318.
145. Giaever, I. and C. Keese, *Monitoring fibroblast behavior in tissue culture with an applied electric field.* Proceedings of the National Academy of Sciences, 1984. **81**(12): p. 3761-3764.
146. Das, L., S. Das, and J. Chatterjee, *Electrical Bioimpedance Analysis: A New Method in Cervical Cancer Screening.* Journal of medical engineering, 2015. **2015**.
147. Giaever, I. and C.R. Keese, *Micromotion of mammalian cells measured electrically.* Proceedings of the National Academy of Sciences, 1991. **88**(17): p. 7896-7900.
148. Ehret, R., et al., *On-line control of cellular adhesion with impedance measurements using interdigitated electrode structures.* Medical and Biological Engineering and Computing, 1998. **36**(3): p. 365-370.
149. Hillebrandt, H., et al., *Electrical and optical characterization of thrombin-induced permeability of cultured endothelial cell monolayers on semiconductor electrode arrays.* Applied Physics A, 2001. **73**(5): p. 539-546.
150. Gross, G.W., et al., *Stimulation of monolayer networks in culture through thin-film indium-tin oxide recording electrodes.* Journal of Neuroscience Methods, 1993. **50**(2): p. 131-143.
151. Aoki, T., et al., *Culture of mammalian cells on polypyrrole-coated ITO as a biocompatible electrode.* Synthetic Metals, 1995. **71**(1): p. 2229-2230.
152. Ehret, R., et al., *Monitoring of cellular behaviour by impedance measurements on interdigitated electrode structures.* Biosensors and Bioelectronics, 1997. **12**(1): p. 29-41.
153. Solly, K., et al., *Application of real-time cell electronic sensing (RT-CES) technology to cell-based assays.* Assay and drug development technologies, 2004. **2**(4): p. 363-372.

154. Ke, N., et al., *The xCELLigence system for real-time and label-free monitoring of cell viability*, in *Mammalian Cell Viability*. 2011, Springer. p. 33-43.
155. Benson, K., S. Cramer, and H.-J. Galla, *Impedance-based cell monitoring: barrier properties and beyond.* Fluids and barriers of the CNS, 2013. **10**(5).
156. Asphahani, F., et al., *Influence of cell adhesion and spreading on impedance characteristics of cell-based sensors.* Biosensors and Bioelectronics, 2008. **23**(8): p. 1307-1313.
157. Thein, M., et al., *Response characteristics of single-cell impedance sensors employed with surface-modified microelectrodes.* Biosensors and Bioelectronics, 2010. **25**(8): p. 1963-1969.
158. Asphahani, F., et al., *Single-cell bioelectrical impedance platform for monitoring cellular response to drug treatment.* Physical biology, 2011. **8**(1): p. 015006.
159. *Micromotion of mammalian cells measured electrically.* Proceedings of the National Academy of Sciences, 1993. **90**(4): p. 1634.
160. Wegener, J., et al., *Use of electrochemical impedance measurements to monitor β-adrenergic stimulation of bovine aortic endothelial cells.* Pflügers Archiv, 1999. **437**(6): p. 925-934.
161. Park, H.E., et al., *Real-time monitoring of neural differentiation of human mesenchymal stem cells by electric cell-substrate impedance sensing.* BioMed Research International, 2011. **2011**.
162. Luong, J.H. and M. Habibi-Rezaei, *Insect cell-based impedance biosensors: a novel technique to monitor the toxicity of environmental pollutants.* Environmental Chemistry Letters, 2003. **1**(1): p. 2-7.
163. Luong, J.H., et al., *Monitoring motility, spreading, and mortality of adherent insect cells using an impedance sensor.* Analytical chemistry, 2001. **73**(8): p. 1844-1848.
164. Stolwijk, J.A., et al., *Impedance analysis of adherent cells after in situ electroporation: non-invasive monitoring during intracellular manipulations.* Biosens Bioelectron, 2011. **26**(12): p. 4720-7.
165. Giaever, I. and C.R. Keese, *A morphological biosensor for mammalian cells.* Nature, 1993. **366**(6455): p. 591-592.

166. Wegener, J., A. Hakvoort, and H.-J. Galla, *Barrier function of porcine choroid plexus epithelial cells is modulated by cAMP-dependent pathways in vitro.* Brain research, 2000. **853**(1): p. 115-124.
167. Lo, C.-M. and J. Ferrier, *Impedance analysis of fibroblastic cell layers measured by electric cell-substrate impedance sensing.* Physical Review E, 1998. **57**(6): p. 6982.
168. Graham, A.H.D., et al., *Neuronal cell biocompatibility and adhesion to modified CMOS electrodes.* Biomedical Microdevices, 2009. **11**(5): p. 1091-1101.
169. Thoumine, O., A. Ott, and D. Louvard, *Critical centrifugal forces induce adhesion rupture or structural reorganization in cultured cells.* Cell motility and the cytoskeleton, 1996. **33**(4): p. 276-287.
170. Dammer, U., et al., *Binding strength between cell adhesion proteoglycans measured by atomic force microscopy.* Science, 1995. **267**(5201): p. 1173.
171. Marcotte, L. and M. Tabrizian, *Sensing surfaces: challenges in studying the cell adhesion process and the cell adhesion forces on biomaterials.* IRBM, 2008. **29**(2): p. 77-88.
172. Hartmann, C., et al., *The impact of glia-derived extracellular matrices on the barrier function of cerebral endothelial cells: An in vitro study.* Experimental Cell Research, 2007. **313**(7): p. 1318-1325.
173. Wegener, J., C.R. Keese, and I. Giaever, *Electric cell–substrate impedance sensing (ECIS) as a noninvasive means to monitor the kinetics of cell spreading to artificial surfaces.* Experimental cell research, 2000. **259**(1): p. 158-166.
174. Bouafsoun, A., et al., *Evaluation of endothelial cell adhesion onto different protein/gold electrodes by EIS.* Macromolecular bioscience, 2007. **7**(5): p. 599-610.
175. Chang, B.-W., et al., *Impedimetric monitoring of cell attachment on interdigitated microelectrodes.* Sensors and Actuators B: Chemical, 2005. **105**(2): p. 159-163.
176. Arndt, S., et al., *Bioelectrical impedance assay to monitor changes in cell shape during apoptosis.* Biosensors and Bioelectronics, 2004. **19**(6): p. 583-594.

177. Bagnaninchi, P.O. and N. Drummond, *Real-time label-free monitoring of adipose-derived stem cell differentiation with electric cell-substrate impedance sensing.* Proceedings of the National Academy of Sciences, 2011. **108**(16): p. 6462-6467.
178. Zhu, J., et al., *Dynamic and label-free monitoring of natural killer cell cytotoxic activity using electronic cell sensor arrays.* Journal of immunological methods, 2006. **309**(1): p. 25-33.
179. Zang, R., et al., *Cell-based assays in high-throughput screening for drug discovery.* International Journal of Biotechnology for Wellness Industries, 2012. **1**(1): p. 31.
180. Ceriotti, L., et al., *Real-time assessment of cytotoxicity by impedance measurement on a 96-well plate.* Sensors and Actuators B: Chemical, 2007. **123**(2): p. 769-778.
181. Yeon, J.H. and J.-K. Park, *Cytotoxicity test based on electrochemical impedance measurement of HepG2 cultured in microfabricated cell chip.* Analytical Biochemistry, 2005. **341**(2): p. 308-315.
182. Xiao, C., et al., *Assessment of Cytotoxicity Using Electric Cell−Substrate Impedance Sensing: Concentration and Time Response Function Approach.* Analytical Chemistry, 2002. **74**(22): p. 5748-5753.
183. Xiao, C. and J.H. Luong, *On-line monitoring of cell growth and cytotoxicity using electric cell-substrate impedance sensing (ECIS).* Biotechnology progress, 2003. **19**(3): p. 1000-1005.
184. Peters, M.F. and C.W. Scott, *Evaluating cellular impedance assays for detection of GPCR pleiotropic signaling and functional selectivity.* Journal of biomolecular screening, 2009. **14**(3): p. 246-255.
185. Ramasamy, S., D. Bennet, and S. Kim, *Drug and bioactive molecule screening based on a bioelectrical impedance cell culture platform.* International Journal of Nanomedicine, 2014. **9**: p. 5789-5809.
186. Hertzberg, R.P. and A.J. Pope, *High-throughput screening: new technology for the 21st century.* Current opinion in chemical biology, 2000. **4**(4): p. 445-451.
187. George, S.R., B.F. O'Dowd, and S.P. Lee, *G-protein-coupled receptor oligomerization and its potential for drug discovery.* Nature Reviews Drug Discovery, 2002. **1**(10): p. 808-820.

188. Chambers, C., et al., *Measuring intracellular calcium fluxes in high throughput mode.* Combinatorial chemistry & high throughput screening, 2003. **6**(4): p. 355-362.
189. Kedrin, D., et al., *Cell motility and cytoskeletal regulation in invasion and metastasis.* Journal of mammary gland biology and neoplasia, 2007. **12**(2-3): p. 143-152.
190. Yu, N., et al., *Real-time monitoring of morphological changes in living cells by electronic cell sensor arrays: an approach to study G protein-coupled receptors.* Analytical chemistry, 2006. **78**(1): p. 35-43.
191. Denelavas, A., et al., *Real-time cellular impedance measurements detect Ca 2+ channel-dependent oscillations of morphology in human H295R adrenoma cells.* Biochimica et Biophysica Acta (BBA)-Molecular Cell Research, 2011. **1813**(5): p. 754-762.
192. Zustiak, S.P., *The role of matrix compliance on cell responses to drugs and toxins: towards predictive drug screening platforms.* Macromolecular bioscience, 2015. **15**(5): p. 589-599.
193. Peters, M.F., et al., *Comparing label-free biosensors for pharmacological screening with cell-based functional assays.* Assay and drug development technologies, 2010. **8**(2): p. 219-227.
194. Zhu, H., et al., *Assembly of Dithiocarbamate-Anchored Monolayers on Gold Surfaces in Aqueous Solutions.* Langmuir, 2008. **24**(16): p. 8660-8666.
195. Roe, M., J. Lemasters, and B. Herman, *Assessment of Fura-2 for measurements of cytosolic free calcium.* Cell calcium, 1990. **11**(2): p. 63-73.
196. Schindelin, J., et al., *Fiji: an open-source platform for biological-image analysis.* Nature methods, 2012. **9**(7): p. 676-682.
197. Kador, K.E., et al., *Tissue engineering the retinal ganglion cell nerve fiber layer.* Biomaterials, 2013. **34**(17): p. 4242-4250.
198. Qian, X.P., et al., *Arrays of self-assembled monolayers for studying inhibition of bacterial adhesion.* Analytical Chemistry, 2002. **74**(8): p. 1805-1810.
199. Barbara Rolfe, J.M., Bing Zhang, Sani Jahnke, Sarah-Jane Le, Yu-Qian Chau, Qiping Huang, Hao Wang, Gordon Campbell and Julie Campbell *The Fibrotic Response to Implanted Biomaterials: Implications for*

Tissue Engineering, in *Regenerative Medicine and Tissue Engineering - Cells and Biomaterials*, D. Eberli, Editor. 2011, InTech. p. 551-568.

200. Knop, K., et al., *Poly(ethylene glycol) in Drug Delivery: Pros and Cons as Well as Potential Alternatives.* Angewandte Chemie International Edition, 2010. **49**(36): p. 6288-6308.
201. Ostuni, E., et al., *A Survey of Structure−Property Relationships of Surfaces that Resist the Adsorption of Protein.* Langmuir, 2001. **17**(18): p. 5605-5620.
202. Krishnan, S., C.J. Weinman, and C.K. Ober, *Advances in polymers for anti-biofouling surfaces.* Journal of Materials Chemistry, 2008. **18**(29): p. 3405-3413.
203. Yue, Z., et al., *PEGylation of platinum bio-electrodes.* Electrochem. Commun., 2013. **27**(0): p. 54-58.
204. Blaszykowski, C., S. Sheikh, and M. Thompson, *Biocompatibility and antifouling: is there really a link?* Trends Biotechnol., 2014. **32**(2): p. 61-62.
205. Ainslie, K.M., et al., *Attenuation of protein adsorption on static and oscillating magnetostrictive nanowires.* Nano Letters, 2005. **5**(9): p. 1852-1856.
206. Heuberger, M., T. Drobek, and J. Vörös, *About the Role of Water in Surface-Grafted Poly(ethylene glycol) Layers.* Langmuir, 2004. **20**(22): p. 9445-9448.
207. Shen, M., et al., *PEO-like plasma polymerized tetraglyme surface interactions with leukocytes and proteins: in vitro and in vivo studies.* Journal of Biomaterials Science, Polymer Edition, 2002. **13**(4): p. 367-390.
208. Holmlin, R.E., et al., *Zwitterionic SAMs that Resist Nonspecific Adsorption of Protein from Aqueous Buffer.* Langmuir, 2001. **17**(9): p. 2841-2850.
209. Hayward, J.A. and D. Chapman, *Biomembrane surfaces as models for polymer design: the potential for haemocompatibility.* Biomaterials, 1984. **5**(3): p. 135-142.
210. Chen, S., et al., *Surface hydration: Principles and applications toward low-fouling/nonfouling biomaterials.* Polymer, 2010. **51**(23): p. 5283-5293.

211. Tegoulia, V.A., et al., *Surface Properties, Fibrinogen Adsorption, and Cellular Interactions of a Novel Phosphorylcholine-Containing Self-Assembled Monolayer on Gold.* Langmuir, 2001. **17**(14): p. 4396-4404.
212. Zheng, J., et al., *Molecular simulation studies of the structure of phosphorylcholine self-assembled monolayers.* The Journal of Chemical Physics, 2006. **125**(17): p. -.
213. He, Y., et al., *Molecular Simulation Studies of Protein Interactions with Zwitterionic Phosphorylcholine Self-Assembled Monolayers in the Presence of Water.* Langmuir, 2008. **24**(18): p. 10358-10364.
214. Chen, S., et al., *Strong Resistance of Phosphorylcholine Self-Assembled Monolayers to Protein Adsorption: Insights into Nonfouling Properties of Zwitterionic Materials.* Journal of the American Chemical Society, 2005. **127**(41): p. 14473-14478.
215. Banerjee, I., R.C. Pangule, and R.S. Kane, *Antifouling Coatings: Recent Developments in the Design of Surfaces That Prevent Fouling by Proteins, Bacteria, and Marine Organisms.* Advanced Materials, 2011. **23**(6): p. 690-718.
216. Shao, Q., et al., *Different effects of zwitterion and ethylene glycol on proteins.* The Journal of Chemical Physics, 2012. **136**(22): p. 225101-6.
217. Luk, Y.-Y., M. Kato, and M. Mrksich, *Self-Assembled Monolayers of Alkanethiolates Presenting Mannitol Groups Are Inert to Protein Adsorption and Cell Attachment.* Langmuir, 2000. **16**(24): p. 9604-9608.
218. Mearns, F.J., et al., *DNA Biosensor Concepts Based on a Change in the DNA Persistence Length upon Hybridization.* Electroanalysis, 2006. **18**(19-20): p. 1971-1981.
219. Liu, G., T. Böcking, and J.J. Gooding, *Diazonium salts: Stable monolayers on gold electrodes for sensing applications.* Journal of Electroanalytical Chemistry, 2007. **600**(2): p. 335-344.
220. Gooding, J.J., *Advances in interfacial design sensors: Aryl diazonium salts for electrochemical biosensors and for modifying carbon and metal electrodes.* Electroanalysis, 2008. **20**(6): p. 573-582.
221. Fairman, C., et al., *Protein Resistance of Surfaces Modified with Oligo(Ethylene Glycol) Aryl Diazonium Derivatives.* ChemPhysChem, 2013. **14**(10): p. 2183-2189.

222. Downard, A.J., S.L. Jackson, and E.S.Q. Tan, *Fluorescence Microscopy Study of Protein Adsorption at Modified Glassy Carbon Surfaces.* Australian Journal of Chemistry, 2005. **58**(4): p. 275-279.
223. Mahouche-Chergui, S., et al., *Aryl diazonium salts: a new class of coupling agents for bonding polymers, biomacromolecules and nanoparticles to surfaces.* Chemical Society Reviews, 2011. **40**(7): p. 4143-4166.
224. Gui, A.L., et al., *A Comparative Study of Electrochemical Reduction of 4-Nitrophenyl Covalently Grafted on Gold and Carbon.* Electroanalysis, 2010. **22**(16): p. 1824-1830.
225. Gui, A.L., et al., *A Comparative Study of Modifying Gold and Carbon Electrode with 4-Sulfophenyl Diazonium Salt.* Electroanalysis, 2010. **22**(12): p. 1283-1289.
226. Liu, G.Z., et al., *A Comparative Study of the Modification of Gold and Glassy Carbon Surfaces with Mixed Layers of In Situ Generated Aryl Diazonium Compounds.* Electroanalysis, 2010. **22**(9): p. 918-926.
227. Liu, G., et al., *The modification of glassy carbon and gold electrodes with aryl diazonium salt: The impact of the electrode materials on the rate of heterogeneous electron transfer.* Chemical Physics, 2005. **319**(1–3): p. 136-146.
228. Downard, A.J., *Electrochemically assisted covalent modification of carbon electrodes.* Electroanalysis, 2000. **12**(14): p. 1085-1096.
229. Pinson, J. and F. Podvorica, *Attachment of organic layers to conductive or semiconductive surfaces by reduction of diazonium salts.* Chem Soc Rev, 2005. **34**(5): p. 429-39.
230. Biniak, S., et al., *The characterization of activated carbons with oxygen and nitrogen surface groups.* Carbon, 1997. **35**(12): p. 1799-1810.
231. Doppelt, P., et al., *Surface Modification of Conducting Substrates. Existence of Azo Bonds in the Structure of Organic Layers Obtained from Diazonium Salts.* Chemistry of Materials, 2007. **19**(18): p. 4570-4575.
232. Baranton, S. and D. Bélanger, *Electrochemical Derivatization of Carbon Surface by Reduction of in Situ Generated Diazonium Cations.* The Journal of Physical Chemistry B, 2005. **109**(51): p. 24401-24410.

233. von Wrochem, F., et al., *Efficient electronic coupling and improved stability with dithiocarbamate-based molecular junctions.* Nat Nano, 2010. **5**(8): p. 618-624.
234. Morf, P., et al., *Dithiocarbamates: Functional and Versatile Linkers for the Formation of Self-Assembled Monolayers.* Langmuir, 2005. **22**(2): p. 658-663.
235. Fadley, C., ed. *Electron spectroscopy: Theory, techniques and applications*. ed. A.D. Baker and C.R. Brundle. Vol. 2. 1978, Academic Press: New York.
236. Baer, Y., et al., *Determination of the electron escape depth in gold by means of ESCA.* Solid State Commun., 1970. **8**(18): p. 1479-1481.
237. Bain, C.D. and G.M. Whitesides, *Attenuation lengths of photoelectrons in hydrocarbon films.* The Journal of Physical Chemistry, 1989. **93**(4): p. 1670-1673.
238. Chockalingam, M., et al., *Biointerfaces on Indium–Tin Oxide Prepared from Organophosphonic Acid Self-Assembled Monolayers.* Langmuir, 2014. **30**(28): p. 8509-8515.
239. Chen, W., et al., *Photonic crystal enhanced microscopy for imaging of live cell adhesion.* Analyst, 2013. **138**(20): p. 5886-5894.
240. Webb, D.J., C.M. Brown, and A.F. Horwitz, *Illuminating adhesion complexes in migrating cells: moving toward a bright future.* Current opinion in cell biology, 2003. **15**(5): p. 614-620.
241. Zamir, E. and B. Geiger, *Molecular complexity and dynamics of cell-matrix adhesions.* Journal of cell science, 2001. **114**(20): p. 3583-3590.
242. Biniak, S., et al., *The characterization of activated carbons with oxygen and nitrogen surface groups.* Carbon, 1997. **35**(12): p. 1799-1810.
243. Pawsey, S., K. Yach, and L. Reven, *Self-assembly of carboxyalkylphosphonic acids on metal oxide powders.* Langmuir, 2002. **18**(13): p. 5205-5212.
244. Wegener, J., C.R. Keese, and I. Giaever, *Electric cell-substrate impedance sensing (ECIS) as a noninvasive means to monitor the kinetics of cell spreading to artificial surfaces.* Exp Cell Res, 2000. **259**(1): p. 158-66.
245. Keselowsky, B.G., D.M. Collard, and A.J. García, *Surface chemistry modulates fibronectin conformation and directs integrin binding and*

specificity to control cell adhesion. Journal of Biomedical Materials Research Part A, 2003. **66**(2): p. 247-259.

246. Keselowsky, B.G., D.M. Collard, and A.J. García, *Surface chemistry modulates focal adhesion composition and signaling through changes in integrin binding.* Biomaterials, 2004. **25**(28): p. 5947-5954.
247. Mrksich, M., *A surface chemistry approach to studying cell adhesion.* Chemical Society Reviews, 2000. **29**(4): p. 267-273.
248. DeMali, K.A. and K. Burridge, *Coupling membrane protrusion and cell adhesion.* Journal of cell science, 2003. **116**(12): p. 2389-2397.
249. Poole, K., et al., *Molecular-scale topographic cues induce the orientation and directional movement of fibroblasts on two-dimensional collagen surfaces.* Journal of molecular biology, 2005. **349**(2): p. 380-386.
250. Venkatakrishnan, A., et al., *Molecular signatures of G-protein-coupled receptors.* Nature, 2013. **494**(7436): p. 185-194.
251. Zambrowicz, B.P. and A.T. Sands, *Knockouts model the 100 best-selling drugs—will they model the next 100?* Nature Reviews Drug Discovery, 2003. **2**(1): p. 38-51.
252. Fang, Y., A.G. Frutos, and R. Verklereen, *Label-free cell-based assays for GPCR screening.* Combinatorial Chemistry & High Throughput Screening, 2008. **11**(5): p. 357-369.
253. Cooper, M.A., *Optical biosensors in drug discovery.* Nature Reviews Drug Discovery, 2002. **1**(7): p. 515-528.
254. Xi, B., et al., *The application of cell-based label-free technology in drug discovery.* Biotechnology journal, 2008. **3**(4): p. 484-495.
255. Meunier, A., et al., *Coupling Amperometry and Total Internal Reflection Fluorescence Microscopy at ITO Surfaces for Monitoring Exocytosis of Single Vesicles.* Angewandte Chemie, 2011. **123**(22): p. 5187-5190.
256. Hoffmann, C., et al., *A FlAsH-based FRET approach to determine G protein–coupled receptor activation in living cells.* Nature methods, 2005. **2**(3): p. 171-176.
257. Moy, A.B., et al., *Histamine alters endothelial barrier function at cell-cell and cell-matrix sites.* American Journal of Physiology-Lung Cellular and Molecular Physiology, 2000. **278**(5): p. L888-L898.

258. Roe, M.W., J.J. Lemasters, and B. Herman, *Assessment of Fura-2 for measurements of cytosolic free calcium.* Cell Calcium, 1990. **11**(2–3): p. 63-73.
259. Simpson, A.W., *Fluorescent Measurement of [Ca2+]c*, in *Calcium Signaling Protocols*, D.G. Lambert, Editor. 1999, Humana Press: Totowa, New Jersey. p. 3-30.
260. Aguilar-Maldonado, B., et al., *Histamine potentiates IP3-mediated Ca2+ release via thapsigargin-sensitive Ca2+ pumps.* Cellular Signalling, 2003. **15**(7): p. 689-697.
261. May, K.M.L., et al., *Development of a Whole-Cell-Based Biosensor for Detecting Histamine as a Model Toxin.* Analytical Chemistry, 2004. **76**(14): p. 4156-4161.
262. Aguilar-Maldonado, B., et al., *Histamine potentiates IP 3-mediated Ca 2+ release via thapsigargin-sensitive Ca 2+ pumps.* Cellular signalling, 2003. **15**(7): p. 689-697.
263. Liu, B., et al., *Accumulation of dynamic catch bonds between TCR and agonist peptide-MHC triggers T cell signaling.* Cell, 2014. **157**(2): p. 357-368.
264. Wang, Y., M.P. Mattson, and K. Furukawa, *Endoplasmic reticulum calcium release is modulated by actin polymerization.* Journal of neurochemistry, 2002. **82**(4): p. 945-952.
265. Ribeiro, C.M.P., J. Reece, and J.W. Putney, *Role of the cytoskeleton in calcium signaling in NIH 3T3 cells An intact cytoskeleton is required for agonist-induced [Ca2+] i signaling, but not for capacitative calcium entry.* Journal of Biological Chemistry, 1997. **272**(42): p. 26555-26561.
266. Janmey, P.A., *Phosphoinositides and calcium as regulators of cellular actin assembly and disassembly.* Annual Review of Physiology, 1994. **56**(1): p. 169-191.
267. Bhattacharyya, S., et al., *Tenascin-C drives persistence of organ fibrosis.* Nat Commun, 2016. **7**.
268. Rege, T.A. and J.S. Hagood, *Thy-1 as a regulator of cell-cell and cell-matrix interactions in axon regeneration, apoptosis, adhesion, migration, cancer, and fibrosis.* The FASEB journal, 2006. **20**(8): p. 1045-1054.

269. Raghu, G., et al., *Collagen synthesis by normal and fibrotic human lung fibroblasts and the effect of transforming growth factor-β.* American Review of Respiratory Disease, 1989. **140**(1): p. 95-100.
270. Verjee, L.S., et al., *Unraveling the signaling pathways promoting fibrosis in Dupuytren's disease reveals TNF as a therapeutic target.* Proceedings of the National Academy of Sciences, 2013. **110**(10): p. E928-E937.
271. Wilburn, J., et al., *The impact of Dupuytren disease on patient activity and quality of life.* The Journal of hand surgery, 2013. **38**(6): p. 1209-1214.
272. Chen, C.Z. and M. Raghunath, *Focus on collagen: in vitro systems to study fibrogenesis and antifibrosis _ state of the art.* Fibrogenesis & Tissue Repair, 2009. **2**(1): p. 1-10.
273. Sennwald, G.R., *Fasciectomy for treatment of Dupuytren's disease and early complications.* The Journal of hand surgery, 1990. **15**(5): p. 755-761.
274. Bayat, A. and D. McGrouther, *Management of Dupuytren's disease–clear advice for an elusive condition.* Annals of the Royal College of Surgeons of England, 2006. **88**(1): p. 3.
275. Karkampouna, S., et al., *Novel ex vivo culture method for the study of Dupuytren's disease: effects of TGFβ type 1 receptor modulation by antisense oligonucleotides.* Molecular Therapy—Nucleic Acids, 2014. **3**(1): p. e142.
276. Chen, C.Z., et al., *The Scar-in-a-Jar: studying potential antifibrotic compounds from the epigenetic to extracellular level in a single well.* Br J Pharmacol, 2009. **158**.
277. Chen, C., et al., *The Scar-in-a-Jar: studying potential antifibrotic compounds from the epigenetic to extracellular level in a single well.* British journal of pharmacology, 2009. **158**(5): p. 1196-1209.
278. Jordana, M., et al., *Heterogeneous proliferative characteristics of human adult lung fibroblast lines and clonally derived fibroblasts from control and fibrotic tissue.* Am Rev Respir Dis, 1988. **137**(3): p. 579-584.
279. Fries, K.M., et al., *Evidence of Fibroblast Heterogeneity and the Role of Fibroblast Subpopulations in Fibrosis.* Clinical Immunology and Immunopathology, 1994. **72**(3): p. 283-292.

280. Koumas, L., et al., *Thy-1 Expression in Human Fibroblast Subsets Defines Myofibroblastic or Lipofibroblastic Phenotypes.* The American Journal of Pathology, 2003. **163**(4): p. 1291-1300.
281. Huang, X., et al. *Impedance based biosensor array for monitoring mammalian cell behavior*. in *Sensors, 2003. Proceedings of IEEE*. 2003.
282. Hata, R. and H. Senoo, *L-ascorbic acid 2-phosphate stimulates collagen accumulation, cell proliferation, and formation of a three-dimensional tissuelike substance by skin fibroblasts.* J Cellular Physiology, 1989. **138**.
283. Treiman, M., C. Caspersen, and S.B. Christensen, *A tool coming of age: thapsigargin as an inhibitor of sarco-endoplasmic reticulum Ca 2+-ATPases.* Trends in pharmacological sciences, 1998. **19**(4): p. 131-135.
284. Lareu, R.R., et al., *In vitro enhancement of collagen matrix formation and crosslinking for applications in tissue engineering: a preliminary study.* Tissue engineering, 2007. **13**(2): p. 385-391.
285. Agarwal, V., et al., *Enhancing the efficacy of cation-independent mannose 6-phosphate receptor inhibitors by intracellular delivery.* Chemical Communications, 2015.
286. Li, B., et al., *Regulation of collagen expression using nanoparticle mediated inhibition of TGF-β activation.* New Journal of Chemistry, 2016.
287. Venkatanarayanan, A., T.E. Keyes, and R.J. Forster, *Label-free impedance detection of cancer cells.* Analytical chemistry, 2013. **85**(4): p. 2216-2222.
288. Asphahani, F. and M. Zhang, *Cellular impedance biosensors for drug screening and toxin detection.* Analyst, 2007. **132**(9): p. 835-841.
289. Moustakas, A. and C. Stournaras, *Regulation of actin organisation by TGF-beta in H-ras-transformed fibroblasts.* Journal of Cell Science, 1999. **112**(8): p. 1169-1179.
290. Tamariz, E. and F. Grinnell, *Modulation of fibroblast morphology and adhesion during collagen matrix remodeling.* Molecular biology of the cell, 2002. **13**(11): p. 3915-3929.
291. Pohlers, D., et al., *TGF-β and fibrosis in different organs—molecular pathway imprints.* Biochimica et Biophysica Acta (BBA)-Molecular Basis of Disease, 2009. **1792**(8): p. 746-756.

292. Thurston, A.J., *Dupuytren's disease.* JOURNAL OF BONE AND JOINT SURGERY-BRITISH VOLUME-, 2003. **85**(4): p. 469-477.
293. Lopez, J., J. Mouw, and V. Weaver, *Biomechanical regulation of cell orientation and fate.* Oncogene, 2008. **27**(55): p. 6981-6993.
294. Bi, X., et al., *A novel method for determination of collagen orientation in cartilage by Fourier transform infrared imaging spectroscopy (FT-IRIS).* Osteoarthritis and Cartilage, 2005. **13**(12): p. 1050-1058.
295. Wilson, S.L., A.J. El Haj, and Y. Yang, *Control of scar tissue formation in the cornea: strategies in clinical and corneal tissue engineering.* Journal of functional biomaterials, 2012. **3**(3): p. 642-687.
296. Lu, P., et al., *Extracellular Matrix Degradation and Remodeling in Development and Disease.* Cold Spring Harbor Perspectives in Biology, 2011. **3**(12): p. a005058.
297. Reinlib, L., et al., *Abnormal secretagogue-induced intracellular free Ca2+ regulation in cystic fibrosis nasal epithelial cells.* Proceedings of the National Academy of Sciences, 1992. **89**(7): p. 2955-2959.
298. Suter, S., et al., *Intracellular calcium handling in cystic fibrosis: normal cytosolic calcium and intracellular calcium stores in neutrophils.* Pediatric research, 1985. **19**(4): p. 346-348.
299. Nguyen, T., W.-C. Chin, and P. Verdugo, *Role of Ca2+/K+ ion exchange in intracellular storage and release of Ca2+*. Nature, 1998. **395**(6705): p. 908-912.
300. Hadeed, J.G., et al., *Calcium-dependent signaling in Dupuytren's disease.* Hand, 2011. **6**(2): p. 159-164.
301. Zhang, R. and X. Xie, *Tools for GPCR drug discovery*. Acta Pharmacologica Sinica, 2012. **33**(3): p. 372-384.
302. Bozem, M., et al., *Hormone-stimulated calcium release is inhibited by cytoskeleton-disrupting toxins in AR4-2J cells.* Cell Calcium, 2000. **28**(2): p. 73-82.
303. Rosado, J.A. and S.O. Sage, *The actin cytoskeleton in store-mediated calcium entry.* The Journal of physiology, 2000. **526**(2): p. 221-229.
304. Takács, B., et al., *Myosin complexed with ADP and blebbistatin reversibly adopts a conformation resembling the start point of the working stroke.* Proceedings of the National Academy of Sciences, 2010. **107**(15): p. 6799-6804.

305. Coué, M., et al., *Inhibition of actin polymerization by latrunculin A.* FEBS letters, 1987. **213**(2): p. 316-318.
306. Meshki, J., et al., *Neurokinin 1 Receptor Mediates Membrane Blebbing in HEK293 Cells through a Rho/Rho-associated Coiled-coil Kinase-dependent Mechanism.* The Journal of Biological Chemistry, 2009. **284**(14): p. 9280-9289.
307. Nobes, C.D. and A. Hall, *Rho, rac, and cdc42 GTPases regulate the assembly of multimolecular focal complexes associated with actin stress fibers, lamellipodia, and filopodia.* Cell, 1995. **81**(1): p. 53-62.
308. Hamburg , M.A. and F.S. Collins *The Path to Personalized Medicine.* New England Journal of Medicine, 2010. **363**(4): p. 301-304.
309. Ginsburg, G.S. and J.J. McCarthy, *Personalized medicine: revolutionizing drug discovery and patient care.* Trends in Biotechnology, 2001. **19**(12): p. 491-496.
310. Ziegler, C., *Cell-based biosensors.* Fresenius' journal of analytical chemistry, 2000. **366**(6-7): p. 552-559.
311. Kane, R.S., et al., *Patterning proteins and cells using soft lithography.* Biomaterials, 1999. **20**(23–24): p. 2363-2376.
312. Wang, S., et al., *High-performance all solid-state micro-supercapacitor based on patterned photoresist-derived porous carbon electrodes and an ionogel electrolyte.* Journal of Materials Chemistry A, 2014. **2**(21): p. 7997-8002.